NTNU
Norwegian University of
Science and Technology

Transmission Electron Microscopy Characterisation of Lead-Free KNN Thin Films

Andreas Toresen

Master of Science in Physics and Mathematics
Submission date: June 2018
Supervisor: Randi Holmestad, IFY
Co-supervisor: Ragnhild Sæterli, IFY

Norwegian University of Science and Technology
Department of Physics

Abstract

Lead-free piezoelectric ceramics have in recent years received an increased interest. Potassium sodium niobate (KNN) has shown promising results, exhibiting properties close to todays dominating piezoelectric material lead zirconate titanate (PZT). It is essential for the KNN thin films to be highly textured in order to obtain comparable electrical properties.

Five differently heat treated $(Na_{0.5}K_{0.5})NbO_3$ thin films were studied in a transmission electron microscope (TEM). The films were synthesised using non-toxic materials and an aqueous solution for chemical solution deposition on (100) oriented strontium titanate (STO) substrates. Focused ion beam (FIB) and precision ion polishing system (PIPS) were used for preparation of cross-section TEM specimens. The specimens were studied using scanning precession electron diffraction (SPED), bright field imaging and high resolution TEM. The sets of SPED data were analysed using automated crystal orientation mapping.

Crystallisation during pyrolysis was found to be in direct correlation with the final crystallographic structure of the films after sintering at 700 °C. The microstructure of the films is dominated by columnar growth in which the crystal structure of the initial layer has been approximately templated through the entire film thickness. The effect of pyrolysis on the microstructure was proven to be consistent with what is given in literature, with lower temperatures producing more epitaxial growth. The crystal texture in the growth direction shows indications of a weak [001] texture attributed to the small amounts of epitaxy in the films. Sintering at 700 °C proved necessary for good bonding between substrate and thin film.

Sammendrag

Det har i de siste årene vært en økt interesse i å finne blyfrie piezoelektriske keramer. Kaliumnatriumniobat (KNN) har vist lovende resultater, med elektriske egenskaper som måler seg med dagens dominerende materiale blyzirkoniumtitanat (PZT). Det er avgjørende for tynnfilmer av KNN å ha høy tekstur for å oppnå disse egenskapene.

Fem forskjellig varmebehandlede $(Na_{0.5}K_{0.5})NbO_3$ tynnfilmer ble studert i et transmisjonselektronmikroskop (TEM). Filmene var syntetisert ved bruk av giftfrie materialer og en vannbasert forløperløsning for kjemisk løsning deponering på (100) orienterte strontiumtitanat (STO) substrater. Fokusert ionestråle (FIB) og presisjon ionepoleringssystem (PIPS) ble brukt i fremstillingen av tverrsnittsprøver for TEM. Prøvene ble studert med skannepresesjonelektrondiffraksjon (SPED), lysefeltsavbildning og høyoppløsnings TEM. Settene med SPED-data ble analysert i en automatisert kartlegging av krystallorienteringer.

Det ble funnet en direkte korrelasjon mellom krystallisasjonen ved pyrolyse og tynnfilmens endelige krystallstruktur etter sintring på 700 °C. Filmenes mikrostruktur er dominert av kolonnevekst der krystallstrukturen til det første laget har omtrentlig blitt repetert gjennom hele filmtykkelsen. Det ble funnet en sammenheng mellom pyrolysetemperatur og mikrostruktur som er i samsvar med det som er gitt i litteraturen, der lavere temperaturer resulterte i mer epitaksiell vekst. Krystallteksturen i vekstretning viste indiksjoner på svak [001]-tekstur, begrunnet med små mengder epitaksi i filmene. Sintring ble påvist nødvendig for god heft mellom substrat og film.

Preface

This thesis is a conclusion of my M.Sc. in Applied Physics at the Department of Physics of the Norwegian University of Science and Technology (NTNU), Trondheim. The study is a result of the collaboration between the Department of Materials Science and Engineering and the Department of Physics at NTNU. The experimental work has been carried out at the Department of Physics with Prof. Randi Holmestad and senior engineer Ragnhild Sæterli from NTNU as supervisors.

I sincerely thank Randi and Ragnhild for valued guidance, patience and enlightening discussions regarding the materials and techniques and for motivational support. I would also like to thank PhD candidate Emil Christiansen for his time spent assisting and guiding me in the processing of collected data. Thanks are due to PhD candidate Adrian Lervik and Adj. Assoc. Prof. Per Erik Vullum for their help with FIB preparation as well as valuable discussions concerning preparation of the material in general. Furthermore, I would also like to thank senior engineer Bjørn Soleim for always giving a helping hand if needed, both in preparation of the samples and in usage of the TEM. Prof. Mari-Ann Einarsrud is thanked for giving valuable insight on the synthesis of the thin films. PhD Candidate Nikolai Helth Gaukås have my gratitude both for providing the films and his help in understanding the structure, properties and synthesis of them. I would also like to thank all the people in the TEM group for interesting talks and discussions as well as motivational interest in my work. Finally, I would like to thank my family and friends for love and support.

Trondheim June 18, 2018

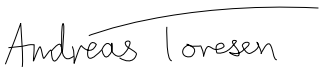

Andreas Toresen

Abbreviations

ACOM	Automated Crystal Orientation Mapping
BF	Bright Field
CCD	Charge-Coupled Device
CSD	Chemical Solution Deposition
DF	Dark Field
DP	Diffraction Pattern
FEG	Field-Emission Gun
FFT	Fast Fourier Transformation
FIB	Focused Ion Beam
HRTEM	High Resolution Transmission Electron Microscope/Microscopy
IPF	Inverse Pole Figure
KN	Potassium Niobate
KNN	Potassium Sodium Niobate
NBD	Nano Beam Diffraction
NN	Sodium Niobate
NTNU	Norwegian University of Science and Technology
ODF	Orientation Distribution Function
PIPS	Precision Ion Polishing System
PZT	Lead Zirconate Titanate
ROI	Region Of Interest
SAD	Selected Area Diffraction
SEM	Scanning Electron Microscope/Microscopy
(S)PED	(Scanning) Precession Electron Diffraction
STO	Strontium Titanate
TEM	Transmission Electron Microscope/Microscopy
VLM	Visible Light Microscope
XRD	X-ray Diffraction

Contents

1 Introduction

The *piezoelectric effect* was first discovered in 1880 by the French brothers Pierre and Jacques Curie [1], and is a phenomenon where a material accumulates electric charge in response to applied mechanical stress. *Ferroelectricity* is a sub-group among piezoelectrics and was discovered later, in 1921 [2], and describes a material that has a spontaneous electric polarisation that can be reversed by the application of an external electric field. Both phenomena have attracted significant scientific interest, especially during World War II, where piezoelectricity was applied in sonars [3]. More recently, science and industry have been merged by applying the functionality offered by ferroelectrics. These materials have a wide range of applications, primarily within microelectromechanical systems, ranging from touch and heat sensors to RAM, gas ignitors and speakers [2, 4, 5]. The dominating materials used in piezoelectric applications today, are lead zirconate titanate (PZT) based ceramics [6]. This is due to their superior piezo- and ferroelectric abilities. However, PZT contains lead – a highly toxic heavy metal which is a hazard both to the environment and human life. In 2003 a directive by the European Union [7] limited the use of lead-containing materials in electrical and electronic equipment, with exceptions being made for materials such as PZT in piezoelectric devices, due to the lack of suitable alternatives. This has led to an increased interest and search for lead-free piezoelectric ceramic substitutes over the last years.

Among the potential lead-free piezoelectric candidates, potassium sodium niobate (KNN) has shown promising results. In 2004 a Japanese research team led by Saito theorised that the material could have properties close to those of PZT [8], and since then the compound received significant attention from the scientific community. Further increases in piezoelectric performance have been made [9], and new application areas within medical diagnostics [10] have been researched. Despite these encouraging results, there still is a major problem in obtaining phase pure thin films with controlled texture. Growth of KNN-based thin films has been investigated by several methods, chemical solution deposition (CSD) being the most common technique due to its efficiency and low cost. However, to date, there are few reports on KNN thin film fabrication obtaining controlled orientation using this technique. In order to further improve the electrical properties, it is essential to have an excellent textured orientation at low temperature with a uniform and controllable microstructure.

The goal of this work is to study the microstructure of chemical solution deposited $K_{0.5}Na_{0.5}NbO_3$ thin films grown on (100) oriented STO substrates. The films have been made at the Department of Material Science and Engineering, NTNU, using non-toxic materials and have been synthesised using an aqueous solution. The research group headed by Mari-Ann Einarsrud

and Tor Grande has for years been internationally leading in synthesis of oxide thin films made by chemical methods. However, as TEM investigation allows the determination of the detailed structure in the films, it is of outmost importance to obtain input from TEM on correlations between structure and synthesis parameters. The texture of the thin films is of particular interest, as this is the dominating factor for their electrical properties. A transmission electron microscope (TEM) has been used in order to study the growth morphology, crystallographic structure and texture of the films. The TEM is favourable as it gives a spatial resolution that enables a detailed study of these features along the film thickness at nanoscale dimensions. Three different pyrolysis temperatures have been used to produce the samples studied. In addition to this, the films have been analysed at different stages of the synthesis. The work is a continuation of the author's project thesis of fall 2017 [11]. A theoretical background covering crystal structure, diffraction, properties of KNN, and an introduction to the TEM is provided in section 2. The experimental procedures of the thin film synthesis, the different preparation techniques used, and details on the TEM are covered in section 3. The results are presented and discussed in section 4 and 5, before a conclusion followed by proposals of further work in sections 6 and 7.

2 Theory

The physics of piezoelectric ceramic thin films is advanced and extensive. This section gives an introduction to the fundamental theory on which the study is based on. First an introduction to crystallography as well as diffraction is presented. This is followed by a brief presentation of the structure and functional properties of KNN. Finally, the basic theory and practical use of the TEM are explained. The content of each section is limited to only subjects of relevance to the study.

2.1 Crystals and Diffraction

Crystals are the most ordered types of solids and are in a state where atoms constitute a highly periodic array and the atomic positions determine the properties of crystalline materials. This section provides an introduction to the definitions needed to understand the behaviour of KNN as well as the results presented in section 4. This section is based on material from [12].

2.1.1 Crystal Lattices

An ideal crystal is constructed by the infinite repetition of identical groups of atoms in a periodic array. This group is called the basis of the crystal. The crystal lattice is a set of mathematical points to which the basis is attached to, and can be described in three dimensions by three translation vectors $\mathbf{a}_1$, $\mathbf{a}_2$ and $\mathbf{a}_3$ (also referred to as $\mathbf{a}$, $\mathbf{b}$ and $\mathbf{c}$, respectively). If all the points in the lattice are equal, and the lattice looks identical when viewed from any point, it is called a Bravais lattice and is defined as

$$\mathbf{r}_j = x_j\mathbf{a}_1 + y_j\mathbf{a}_2 + z_j\mathbf{a}_3, \tag{2.1}$$

where x_j, y_j and z_j are integers, and $0 \leq x_j, y_j, z_j \leq 1$. The following convention is often used for the angles between the lattice vectors: $\mathbf{a}_1 \angle \mathbf{a}_2 = \gamma$, $\mathbf{a}_2 \angle \mathbf{a}_3 = \alpha$ and $\mathbf{a}_1 \angle \mathbf{a}_3 = \beta$. The parallelepiped defined by these vectors is called a unit cell, and this cell has a volume given by

$$V_c = |\mathbf{a}_1 \cdot (\mathbf{a}_2 \times \mathbf{a}_3)|. \tag{2.2}$$

The primitive unit cell contains a total of one lattice point equivalent to one basis in each

corner. For some crystals it is more convenient to choose a unit cell that best displays the symmetry of the crystal, known as the conventional unit cell. Figure 2.2 illustrates a 2D example of this. The cells in Figure 2.1 are some examples of conventional unit cells. There are fourteen different Bravais-lattices for 3D crystals, and these are divided into seven lattice systems. The Bravais-lattices are listed in Table 1.

Table 1: Overview of the different 3D lattice systems and their unit cells. From [13].

System	**Number of lattices**	**Axes and agnles**	**Unit Cells**
Cubic	3	$a_1 = a_2 = a_3$ $\alpha = \beta = \gamma = 90°$	P, I, F
Tetragonal	2	$a_1 = a_2 \neq a_3$ $\alpha = \beta = \gamma = 90°$	P, I
Orthorombic	4	$a_1 \neq a_2 \neq a_3$ $\alpha = \beta = \gamma = 90°$	P, I, F C
Triclinic	1	$a_1 \neq a_2 \neq a_3$ $\alpha \neq \beta \neq \gamma$	P
Trigonal	1	$a_1 = a_2 = a_3$ $\alpha = \beta = \gamma < 120°, \neq 90°$	P
Monoclinic	2	$a_1 \neq a_2 \neq a_3$ $\alpha = \gamma = 90° \neq \beta$	P, C
Hexagonal	1	$a_1 = a_2 \neq a_3$ $\alpha = \beta = 90°$ $\gamma = 120°$	P

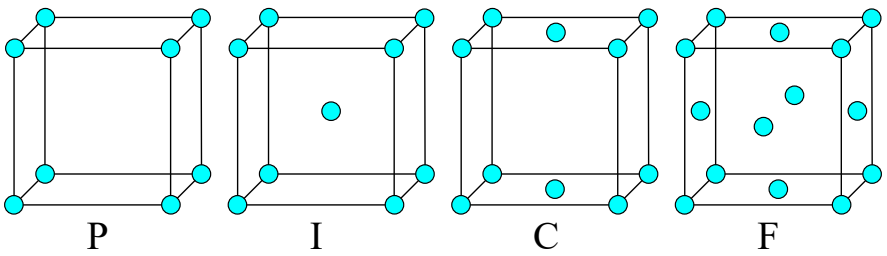

Figure 2.1: Different types of unit cells: P) primitive, I) body-centred, C) side-centred, F) face-centred

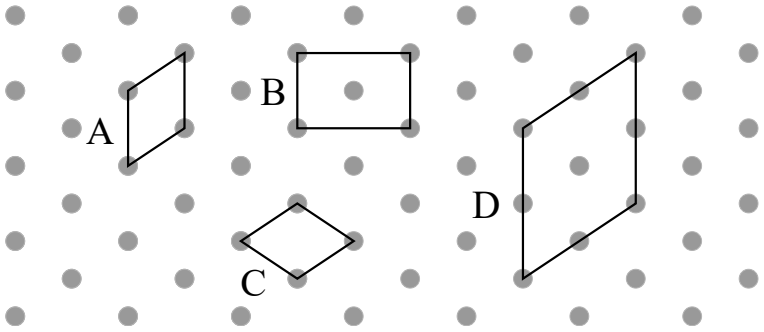

Figure 2.2: Illustration of different cells for a 2D lattice. Unit cells A and C are examples of primitive unit cells. Unit cell D is an extended version of unit cell A, and is not primitive. Unit cell B is the conventional unit cell, showing that the lattice actually is rectangular.

2.1.2 Directions and Planes

The orientation of a crystal plane and the direction in a crystal are determined by three points and are indexed using the Miller indices h, k and l. Lattice planes are denoted (hkl), and represent a plane that intercepts the three points a_1/h, a_2/k and a_3/l, or some multiple thereof. These planes will, when parallel translated throughout the entire crystal, contain all the lattice points in the crystal. Some important planes are illustrated in Figure 2.3. Some planes are equivalent to each other by the symmetry of the lattice, the family of these are denoted with braces, i.e. $\{hkl\}$. Directions are denoted with square brackets and are defined as $[hkl] = h\mathbf{a}_1 + k\mathbf{a}_2 + l\mathbf{a}_3$, where the h, k and l values have been divided by the highest common denominator. Indicies in angle brackets such as $\langle hkl \rangle$ denote a family of directions which are equivalent due to symmetry operations. An example of this is a cubic structure where [100], [010], [001] or the negative of these directions are all equivalent. Negative values are usually represented with a bar as in $\bar{1}$ for -1. For a cubic system with unit-cell dimension a, the spacing d_{hkl} between adjacent (hkl) planes is given by

$$d_{hkl} = \frac{a}{\sqrt{h^2 + k^2 + l^2}}. \tag{2.3}$$

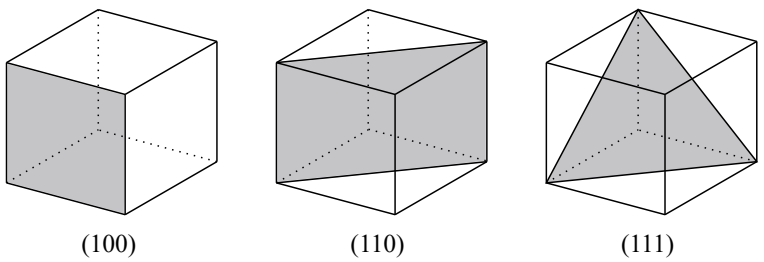

Figure 2.3: Examples of atomic planes in cubic crystal systems.

2.1.3 Reciprocal Lattice

Due to the periodicity of the crystal lattice, one can express the properties of the lattice in a Fourier series. The Fourier transform of the real-space lattice (also called the direct lattice) is known as the reciprocal lattice, and plays a fundamental role in the theory of diffraction. The reciprocal lattice vector $\mathbf{G}$ is defined as

$$\mathbf{G} = u\mathbf{b}_1 + v\mathbf{b}_2 + w\mathbf{b}_3, \tag{2.4}$$

where u, v and w are integers. The axis vectors $\mathbf{b}_1$, $\mathbf{b}_2$ and $\mathbf{b}_3$ of the reciprocal lattice are defined by

$$\mathbf{b}_1 = 2\pi\frac{\mathbf{a}_2 \times \mathbf{a}_3}{V_c} \qquad \mathbf{b}_2 = 2\pi\frac{\mathbf{a}_3 \times \mathbf{a}_1}{V_c} \qquad \mathbf{b}_3 = 2\pi\frac{\mathbf{a}_1 \times \mathbf{a}_2}{V_c}, \tag{2.5}$$

where V_c is the volume of the unit cell in real space, given by equation 2.2. Each point in the reciprocal lattice corresponds to a set of planes in real space. Through simple geometric arguments it can be proved that a reciprocal lattice vector $[uvw] = [hkl]$ is perpendicular to the plane (hkl) and that

$$|\mathbf{G}_{hkl}| = \frac{2\pi}{d_{hkl}}, \tag{2.6}$$

where $\mathbf{G}_{hkl}$ is the reciprocal lattice vector and d_{hkl} is the interplanar distance in real space.

2.1.4 Diffraction

Diffraction is a phenomenon that occurs due to waves interfering after scattering off an obstacle. The analysis of a resulting diffraction pattern (DP) will give information on the structure of the obstacle. Because of the short wavelength of electrons, a material's atom plane spacing will act as slits and scatter an incident parallel electron beam. This will create a DP containing information on the crystal structure of the material, as it essentially shows the reciprocal lattice. The theory behind diffraction can be described using both the Laue condition and Bragg's law, both illustrated in Figure 2.4.

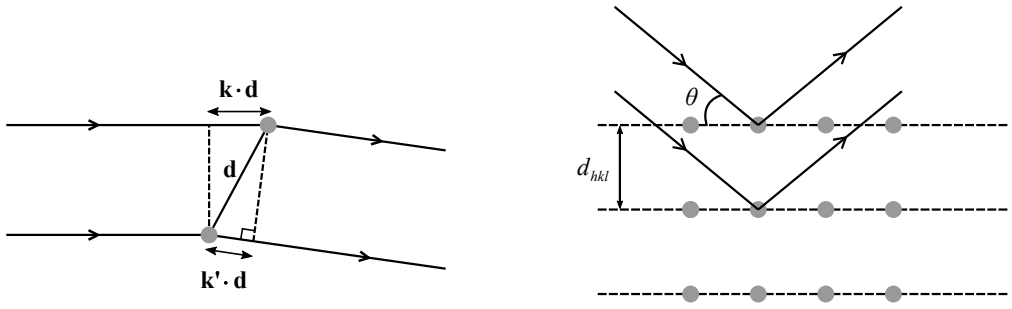

(a) Laue approach (b) Bragg approach

Figure 2.4: The Laue (a) and Bragg (b) approaches to scattering interference.

The Laue condition assumes that the electron waves are scattered elastically. The incident and scattered waves are described by $\mathbf{k}$ and $\mathbf{k}'$, respectively. The scattering vector is defined as $\Delta\mathbf{k} = \mathbf{k}' - \mathbf{k}$. According to the Laue condition, the incoming waves must scatter in phase with each other in order to achieve constructive interference, i.e. the scattering vector equals an integer multiple of the wavelength $\lambda = 2\pi/k$. This can be expressed mathematically as

$$\mathbf{d} \cdot \Delta\mathbf{k} = 2\pi n, \tag{2.7}$$

where d is the distance between the two objects that the incoming wave is scattered on and n is an integer. This is the Laue condition for interference, and only holds true if the scattering vector $\Delta\mathbf{k}$ is a reciprocal vector $\mathbf{G}$. As mentioned, the reciprocal lattice is described as the Fourier transform of the real crystal lattice.

Bragg diffraction is a special case of Laue diffraction where the wave is scattered of the atomic planes in the material, as illustrated in Figure 2.4. Bragg's law formulates the relation between the scattering angle θ with the atomic plane spacing d_{hkl}. The incoming wave that scatter of the second plane will transverse an extra length of $2d\sin\theta$. Constructive interference occurs when the distance is an integer multiple m of the wavelength, yielding Bragg's law

$$2d_{hkl}\sin\theta = m\lambda. \tag{2.8}$$

The lattice planes separated by the interplanar distance d_{hkl} are known as Bragg planes if the plane is "in Bragg", i.e. Bragg's law is satisfied.

The Ewald sphere is a geometrical construct that visualises which (hkl) planes will give diffraction. Figure 2.5 shows it in two dimensions. It is constructed by first drawing the reciprocal lattice, then adding the incident wave vector $\mathbf{k}$ so that it ends at one of the lattice

points. A circle of radius $k = 2\pi/\lambda$ is then drawn about the origin of $\mathbf{k}$. Any point in the reciprocal lattice that intersects with the circle will fulfil the Laue condition, meaning that the set of (hkl) planes associated to that point will be visible in the diffraction pattern.

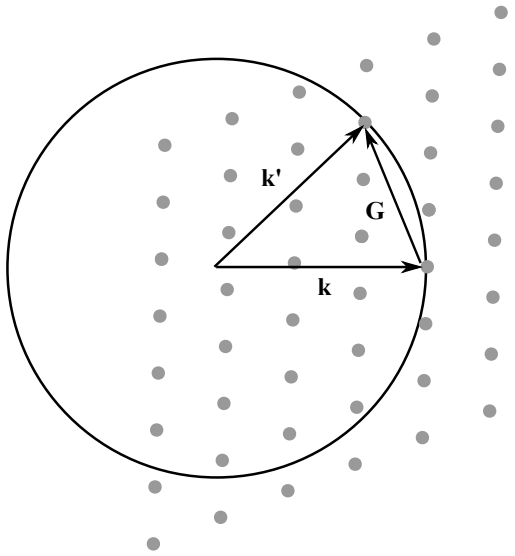

Figure 2.5: The Ewald construction presented in a two dimensional reciprocal lattice.

The three different approaches to diffraction describe how analysis of distances and angles observed in DPs give information on both the structure and orientation of a material. More details on diffraction patterns produced by electrons in the TEM will be presented in section 2.3.3

2.1.5 Defects

A real crystal will contain some dislocations. These structural defects can modify the properties of crystalline materials, especially ferroelectrics. It has been proven that defects can lead to changes in ferroelectric behaviours such as polarisation reversal, phase transition temperatures, ferroelectric fatigue and domain kinetics [14]. This study will not focus on defects in general, however, separation of grains is essential. Grain boundaries are planar defects i.e. two-dimensional imperfections in crystals, and occur where the direction of the crystal lattice abruptly changes. This is most common when two crystals begin to grow separately and then meet. A crystalline material may consist of several grains, each of which have a different crystallographic orientation to its neighbours.

2.2 Material

In order to understand the results produced in TEM, it is necessary to know details about the materials analysed. In this study, the material characterised was potassium sodium niobate, $K_xNa_{1-x}NbO_3$ (KNN) grown on strontium titanate (STO). This section provides information on the structure and properties of the ferroelectric ceramic KNN, and is partly based on material from [15].

2.2.1 Structure of KNN

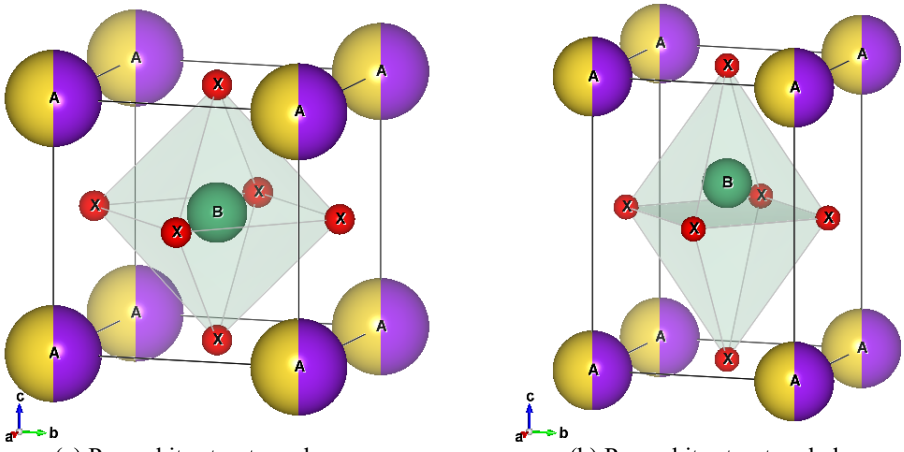

(a) Perovskite structure above the Curie-temperature

(b) Perovskite structure below the Curie-temperature

Figure 2.6: Illustration of different perovskite polymorphs of KNN. (a) illustrates the non-piezoelectric cubic structure ($Pm\bar{3}m$), while (b) illustrates the tetragonal structure ($P4mm$) which is piezoelectric. The marked atoms represent: A) potassium and sodium, B) niobium and X) oxygen. The structures were created using VESTA [16].

Ferroelectrics is a sub-group of piezoelectrics, exhibiting characteristics of piezoelectric materials. What makes ferroelectrics special is that they are capable of maintaining the polarisation even upon removal of the external electric field. Most ferroelectric ceramics have a perovskite structure, KNN being no exception. Figure 2.6 (a) shows the atomic model of the idealised cubic unit cell of KNN. The perovskite structure has the chemical formulae ABX_3, where A and B are metallic cations and X is a non-metallic anion [17]. KNN is a perovskite oxide, meaning that the X-site is occupied by oxygen. The material has a complex perovskite structure, as the A-site is shared by both potassium and sodium. This is because KNN is made from compositions between potassium niobate (KN) and sodium niobate (NN).

Many different potassium to sodium ratios have been tried [9], as it affects the material's phase which again affects ferroelectric properties. However, a 50% KN composition is most common, and this is the ratio used in the materials studied in this thesis. Both KN and NN are perovskites and go through different polymorphs, meaning that the composition also affects the polymorphism of KNN. Figure 2.7 shows the pseudo-binary phase diagram of the KN-NN system [18]. The structure of KNN is dependent on temperature, and as the figure shows, it goes through the phases rhombohedral (R), orthorhombic (O), tetragonal (T) and cubic (C). The structures will affect the ferroelectric properties of the material.

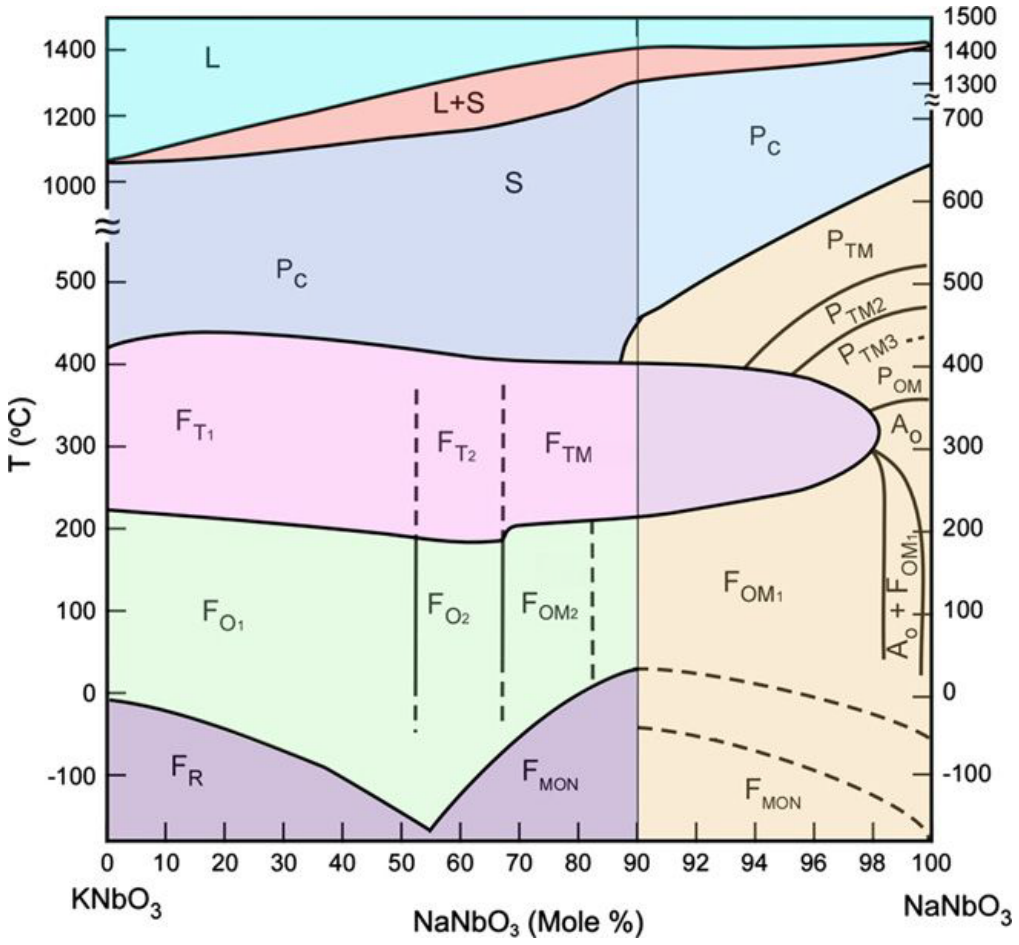

Figure 2.7: Phase diagram of $KNbO_3$–$NaNbO_3$ pseudo-binary solid solutions from Li et al.[18]. The notation used for each phase is X_Y, where X is either type of unit cell or L and S for liquid and solid, respectively, while Y represents the phase as described in the text.

The orthorhombic structure of KNN is important, as this is the one it has at room temperature. The crystals in the KNN thin film analysed in this study should therefore consist of orthorhombic unit cells. The exact parameters of this structure are not known and there are different values given in literature [19, 20, 21]. The most common description of the structure

uses the space group $Amm2$ and describes the lattice vectors $\mathbf{b}_o$ and $\mathbf{c}_o$ being oriented approximately parallel to the $\langle 110 \rangle_c$ axes of the cubic structure. The $\mathbf{a}_o$ axis is approximately equal to the cubic lattice constant and is oriented in the $\langle 100 \rangle_c$ direction. A simplified illustration of the orthorhombic phase is presented in Figure 2.8.

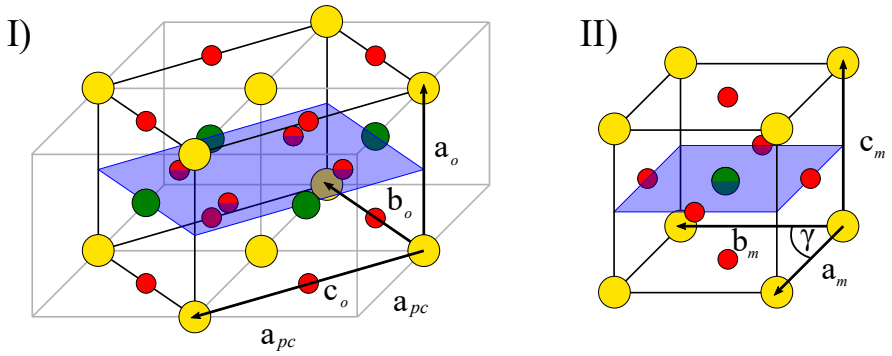

Figure 2.8: Illustration of the orthorhombic (I) and monoclinic (II) structure of KNN adapted from [19]. Yellow atom is potassium and sodium, green is niobium and red is oxygen. The grey cells in (I) represent the pseudo-cubic structure with lattice constant $\mathbf{a}_{pc}$. The lattice parameters with notations o and m illustrate the orthorhombic and monoclinic structures, respectively. The blue planes are mirror planes used to better visualise the structures.

As mentioned in section 2.1.1, different conventional unit cells can be used when describing a crystal, some being more convenient than others. Mgbemere et al. [19] describe the lattice parameters for the orthorhombic phase of KNN at room temperature as $\mathbf{a}_o = 3.9445$Å, $\mathbf{b}_o = 5.64377$Å and $\mathbf{c}_o = 5.67647$Å. In some scenarios a pseudo-cubic structure is favourable, as it is generally easier to work with due to its high symmetry. An additional advantage is that it gives the possibility of applying equation 2.3 when calculating interplanar distances. To be able to define this structure, an approximation of the orthorhombic phase is needed, assuming $\mathbf{b}_o \approx \mathbf{c}_o \approx \sqrt{2}\mathbf{a}_o$. Figure 2.8 (I) illustrates the relation between the two structures. An average of the three vectors defined by the orthorhombic parameters can be used to calculate the value of the pseudo-cubic lattice constant $\mathbf{a}_{pc}$, defining it as

$$\mathbf{a}_{pc} = \frac{1}{3}\left(\frac{1}{\sqrt{2}}(\mathbf{b}_o + \mathbf{c}_o) + \mathbf{a}_o\right). \tag{2.9}$$

Using the values given by Mgbemere et al., this results in $\mathbf{a}_{pc} \approx 3.9831$Å. However, this simplified approximation creates the possibilities of error. Some argue that it is more convenient to describe the KNN at room-temperature with a monoclinic structure, resulting in crystallographic indexing often being inconsistent in literatures. Due to the complexity in the phase, it is possible to define the structure based on the perovskite-type ABO_3 primary

cell, as it possesses monoclinic symmetry. The redefinition is based on the same principles as the pseudo-cubic, however, the difference in $\mathbf{b}_o$ and $\mathbf{c}_o$ is taken into account. The redefinition will therefore result in different values for the three lattice parameters as well as an angle $\gamma \neq 90°$, while $\alpha = \beta = 90°$. The result is a monoclinic structure as illustrated in Figure 2.8 (II). Mgbemere et al. [19] describe the new angle as $\alpha = 90.33°$.

The substrate on which the thin film is grown on is strontium titanate (STO), and from [22] it is described as a cubic perovskite with lattice constant $\mathbf{a}_{\mathrm{STO}} = 3.905$Å. This is close to the calculated value of the pseudo-cubic lattice constant for KNN, $\mathbf{a}_{pc} \approx 3.9831$Å, which is also a perovskite. In other words, the structures of STO and KNN show similarities, which promote the possibility of the deposited KNN thin film to lock into the orientation of the substrate. If the lattices are ordered, it is called epitaxial growth. Epitaxy refers to the KNN thin film overlayer being well-defined in orientation with respect to the STO substrate's crystal structure and is favourable as it results in a high textured thin film.

2.2.2 Functional Properties of KNN

A piezoelectric material produces a charge when it is subjected to an external force. In piezoelectric perovskites, the external force causes a displacement of the ion at the B-site, giving rise to an electrical polarisation in the material. This is known as the direct piezoelectric effect. This is also reversible, meaning that the material can experience a physical change when an external electric field is applied. The piezoelectric coefficient can be used for describing the quality of the material's piezoelectric property, by describing the relationship between polarisation and the applied stress.

Most ferroelectric materials are paraelectric above a certain phase transition temperature, called the Curie temperature (T_C). As seen in Figure 2.7, the Curie temperature for KNN is somewhere around 420 °C. Above this temperature the material becomes cubic, allowing no spontaneous polarisation and is essentially a symmetric, paraelectric material. At lower temperatures the unit cell can be distorted in different directions, giving rise to spontaneous polarisation and become ferroelectric. Between room temperature and T_C, KNN has either an orthorhombic or a tetragonal structure which both are ferroelectric, thus also exhibiting piezoelectric properties. The origin of the spontaneous polarisation can be easily explained from the tetragonal perovskite structure presented in Figure 2.6 (b). When the perovskite structure changes to tetragonal, the B-site atom is no longer equally affected by the surrounding oxygen atoms. Therefore, a spontaneous shift in the equilibrium position of the B-site occurs perpendicular to the plane formed by the four most closely positioned oxygen

atoms. This promotes the possibility of polarisation along one of the six $\langle 100 \rangle_c$ pseudo-cubic directions [23]. The same principle applies to the orthorhombic structure, but the distortion will in this scenario result in a spontaneous polarisation along one of the twelve $\langle 011 \rangle_c$ pseudo-cubic directions [24], as illustrated in Figure 2.9. It is important to mention that definition of the unit cells of the structure is dependent on the orientation of the polarisation. This is because the polarisation is always oriented in either $[001]_o$ or $[00\bar{1}]_o$ direction for the orthorhombic phase.

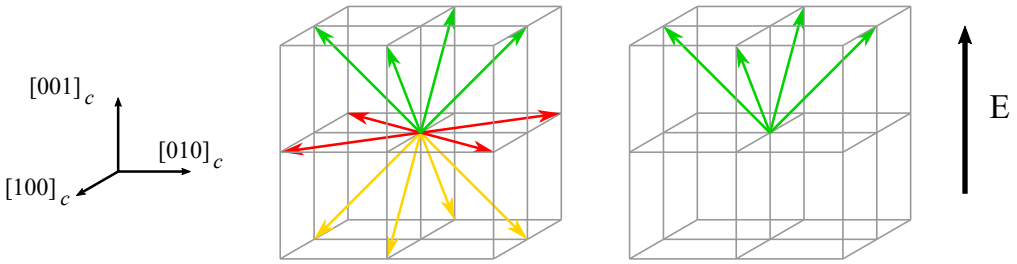

Figure 2.9: Illustration of spontaneous polarisation of the orthorhombic phase of KNN, adapted from [24]. Before poling, the polarisation is along the twelve $\langle 011 \rangle_c$ families. After poling along $[001]_c$, only four polarisation directions are left.

Below the Curie temperature, ferroelectrics are always microscopically polar. However, at a macroscopic scale the individual orientation of the grains will differ, which in turn will cause the possible orientations of polarisation to differ. In addition to this, each unit cell within the individual grains has the possibility of polarisation in one of twelve different directions, as illustrated in Figure 2.9. This promotes the possibility of regions with differently oriented uniform polarisation within the grains, known as ferroelectric domains. These domains are separated by domain walls, in which the polarisation direction changes. The orientation of the polar axes are more or less random, resulting in zero net polarisation within the material [6]. A ferroelectric material has the ability to switch the direction of the spontaneous polarisation within the domains if an electric field of significant strength is applied. This is also known as poling, and it forces the B-site atoms into the currently most energetically favourable positions where they will remain permanently. Figure 2.9 illustrates the possible polarisation directions before and after poling. After poling along $[001]_c$ there are only four of the twelve possible spontaneous polarisations left ($[011]_c$, $[0\bar{1}1]_c$, $[101]_c$, and $[\bar{1}01]_c$). This means that poling will result in a material with much higher net polarisation. However, as the displacement of the B-site atom is dependent on the crystal orientation, the overall polarisation will still be limited by the orientation of the grains. This means that the angle between the grains and the direction of the field from poling decides the overall polarisation of the material. It is therefore favourable that the grains have some preferred orientation

which can be described as textured growth.

Controlled texture will result in more B-site atoms being dislocated in the same direction, creating a high net polarisation, which again results in a better piezoelectric effect. This is the reason for why textured growth is so essential when producing this material, and it is usually made possible through epitaxial growth. In 2004, Saito et al. managed a performance breakthrough in KNN [8]. One of the main reasons for this was strong texture, thereby allowing near perfect alignment of the individual grains.

2.3 Transmission Electron Microscopy

In order to fully understand the properties of a material, one must first analyse the structure of it. Microscopy techniques are essential in characterisation of materials, and many different possibilities exist today. Visible light microscopes (VLMs) are maybe the most familiar equipment, but these do not possess the ability to study structures at the nano scale. In order to see these fine details, powerful microscopes are needed, using electrons instead of light. In 1931, the first transmission electron microscope (TEM) was made by Ernst Ruska and Max Knoll [25]. This section provides information on modern TEMs and is heavily based on the detailed book by Williams and Carter [26].

2.3.1 Construction and Design

In order to understand the results produced in a TEM, a basic understanding of the microscope itself is needed. As the name indicates, the fundamental principle in a TEM is that electrons are transmitted through a specimen. Different interactions may occur when the electrons hit the sample, and the TEM detects the various attributes of these electrons. This is made possible by a system of various components.

Electron lenses are designed to act like the optical glass lenses in a VLM, and are basically used to change the focus, intensity or magnification. The TEM's electromagnetic lenses consist of cylindrical iron cores with holes drilled through, called pole pieces, with copper wires coiled inside. When a current is passed through the coils, it creates an axially symmetric magnetic field inside the pole. The field is weakest at the centre and gets stronger closer to the pole piece, making the magnetic field act as a convex lens, focusing the electric rays. This makes it possible to change the focusing strength of the lens, simply by changing the current in the copper wire.

Apertures are used to select specific areas of the electron beam, and exclude the rest from traversing further down the TEM column. They consist of small metals disks with circular holes that limits the collection angle of a lens. The apertures play a vital role in the setup for different TEM techniques, which will be described further in section 2.3.3.

The electron gun is the electron source of the instrument, and can be one of two main types. The thermionic gun uses either a tungsten (W) or lanthanum hexaboride (LaB_6) filament which is heated to sufficiently high temperature in order to extract the electrons. The field-emission gun (FEG) uses an electric field to extract the electrons from a very fine W needle tip. The brightness (intensity per solid angle) and coherency of the FEG is generally superior to a thermionic gun. However, as the tip of the filament of a FEG is smaller than that of a thermionic gun, it cannot image as large areas.

It is convenient to divide the TEM in three parts which are stacked vertically in a column: the illumination system, the objective lens/stage, and the imaging system. The complete TEM column is illustrated in Figure 2.10. The illumination system consists of the electron gun and condenser lenses which forms the extracted electrons to a beam. The purpose of the illumination system is to transport the electrons from the source and transfer them to the specimen. The objective lens and stage is the "heart" of the TEM. This is where the specimen holder is inserted and where all specimen-beam interactions take place, creating both images and diffraction patterns. The objective lens is therefore the most important lens in the TEM, as its quality determines the quality of all the information gained from the sample. The final part is the imaging system, where several lenses magnify the images produced by the objective lens. The magnifying lenses are often referred to as the intermediate and diffraction lenses and the final lens as the projector lens. The images are finally focused onto a viewing screen or CCD camera.

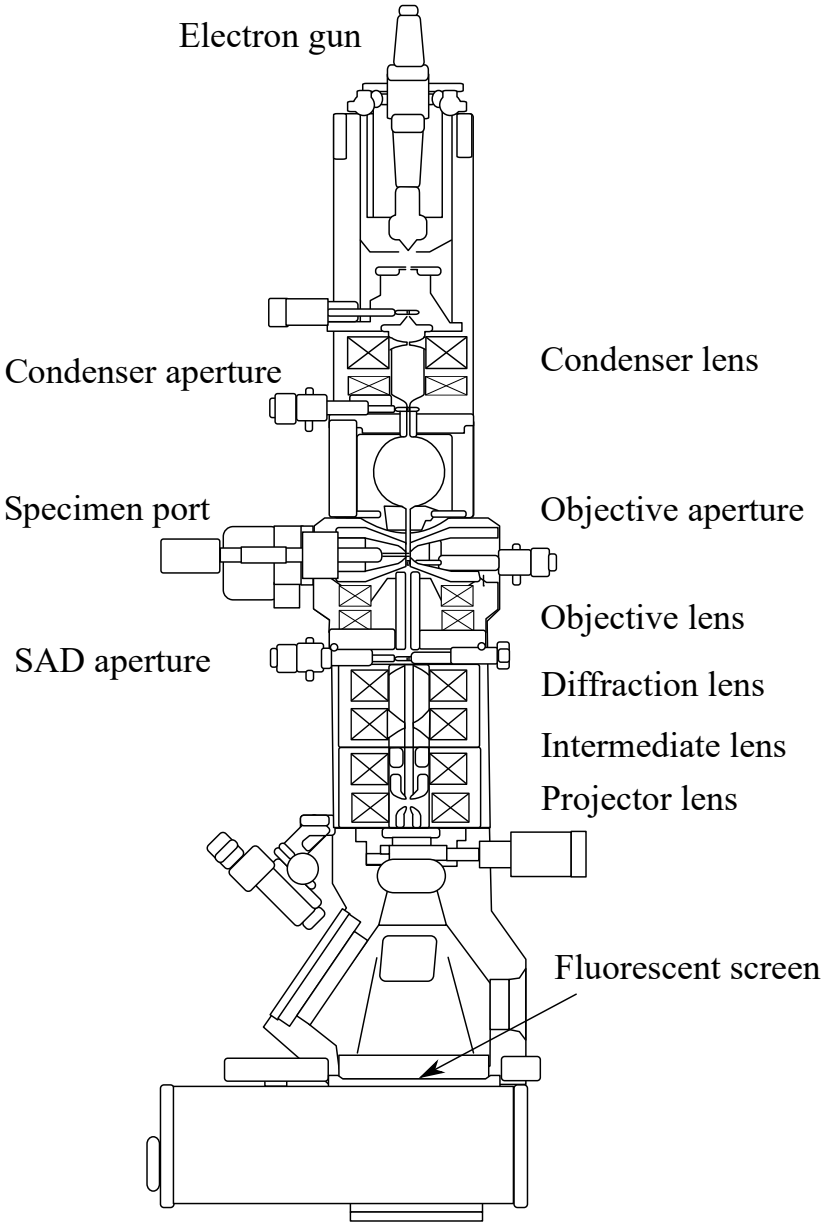

Figure 2.10: Schematic of the TEM column, modified version from [27]

2.3.2 Signals in TEM

When the electronic beam hits the specimen, several interactions occur. The electron is a low-mass, negatively charged particle, meaning it interacts both with the electrons and the positive nucleus of atoms inside the sample. This is one of the reasons why the TEM is such a versatile instrument. The generated signals are summarised in Figure 2.11, and the most important are explained below.

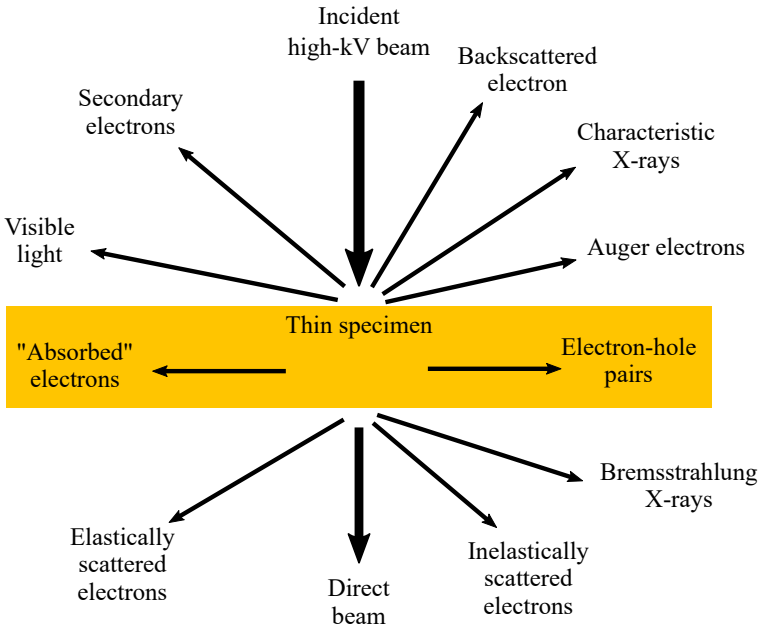

Figure 2.11: Schematic presenting the variety of signals generated when a high-energy electron beam interacts with a thin (10-100 nm) specimen. The direction of the arrows does not accurately describe the direction of the signal, but indicate where the signal is strongest or where it is detected. Figure adapted from [26]

Elastic scattering occurs when the electrons are scattered without losing energy. Elastic scattered electrons interact with the specimen through the Coulomb force, and the interaction can either be with the negatively charged electron cloud or the positively charged nucleus of an atom. The angle of the scattering is dependent on what the electron interacts with, the electron cloud creating relatively low angles and the nucleus creating much larger angles, up to 180°. The elastically scattered electrons are the major source of contrast in TEM imaging as well as creating much of the intensity in the diffraction patterns.

Inelastic scattering occurs when the scattered electrons loose some energy on the way through the specimen. The lost energy may eject a secondary electron from the specimen or produce collective oscillations. This results in a whole range of new signals which can be

used to analyse the composition of the material. Most of the inelastic scattered electron are forward scattered, and are studied with energy electron loss spectroscopy (EELS).

2.3.3 Techniques in TEM

Due to all the available signals, there are a lot of information to be extracted from a specimen in TEM. The instrument is equipped with multiple detectors to record the different signals, and many different techniques can be applied in order to process the data. The TEM is an incredible versatile microscope and this section will explain some of the most common TEM techniques and the physical principles behind them.

Electron Diffraction

Electron diffraction is one of the most useful techniques in the TEM, as the diffraction pattern (DP) contains information about the crystal structure of the specimen and more. DPs can be observed at the back focal plane, and by adjusting the lenses in the TEM this can be projected onto the viewing screen. The most common technique used for producing DPs in TEM is selected area diffraction (SAD), which uses the SAD aperture to restrict the area of a specimen that will contribute to the DP obtained, as shown in Figure 2.13 (b). Each point in the DP corresponds to a (hkl) plane in the direct lattice. As described in section 2.1.4, the Ewald sphere is dependent on the wavelength of the incoming beam. As the wavelength of electrons is small, the Ewald sphere becomes very large, resulting in multiple visible points in the DP produced in the TEM.

As the diffraction patterns are images of the real space crystal planes fulfilling Bragg's law, the patterns are dependent on the crystal structure. The diffraction image is also dependent on the orientation of the crystal. This means that different grains will produce different DPs. It is possible to orient a sample to find one crystal's *zone axis*. This term is used to denote an orientation with high symmetry and is expressed with Miller indices. A zone is defined as a set of planes or faces in a crystal whose intersections are all parallel. The zone axis is the common direction of the interactions, and must pass through the origin of the cell. The symmetry observed in the diffraction image will also be dependent on whether the material analysed is monocrystalline (i.e. a single grain) or polycrystalline. This is well illustrated by comparing a diffraction image of a single crystal and a polycrystal. Figure 2.12 (a) shows a regular diffraction pattern produced from a single STO crystal which can be indexed, while (b) shows a ring pattern of multiple grains of KNN, indicating a polycrystalline area.

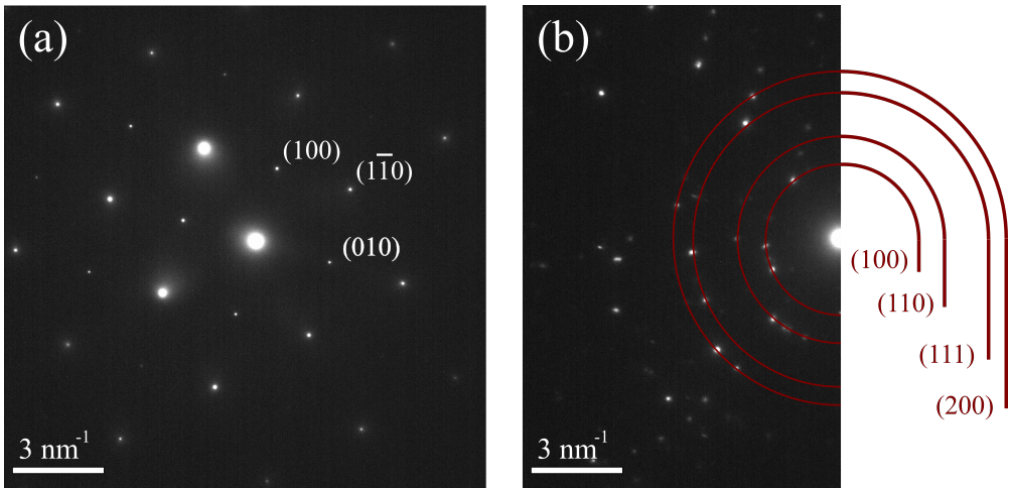

Figure 2.12: Electron diffraction patterns from a single STO crystal (a), and multiple grains of KNN (b) with different orientations resulting in a ring-like pattern. The STO crystal is viewed along its [001] direction.

In order to fully explain the diffraction performed in a TEM, it is usually required to use dynamic diffraction theory. However, it is possible to explain the underlying theory using a kinematic approximation. This is based on the assumptions that the scattering between incident and diffracted beam is both single and coherent. With this approach, the intensity of the spots in the diffraction pattern can be described as proportional to the square modulus of the structure factor, which again can be expressed as

$$F_{hkl} = \sum_j f_j e^{2\pi i(hx_j + ky_j + lz_j)}. \tag{2.10}$$

The equation is a sum of all the atoms j in the unit cell. It shows that the diffraction pattern is influenced by the type of atom, due to its atomic scattering factor f_j, the position of the cell (x, y, z) and the specific atomic planes (hkl) that make up the crystal structure.

Bright and Dark Field Imaging

Bright field (BF) imaging is the most common and familiar operation mode for a TEM. In this mode, the direct beam is used to form an image of unscattered electrons. The selection is done using the objective aperture, as illustrated in Figure 2.13 (a). As a result, areas of the material that scatter strongly will appear dark in the image, while areas that scatter less will be brighter. Consequently, a smaller objective aperture leads to greater image contrast. The contrast in the image can be the result for various effects such as mass-thickness and

diffraction. Mass-thickness contrast will make a region darker if the specimen is thicker or the region contains elements with higher atomic number Z, as both results in more scattering. Diffraction contrast is the main source of contrast in images of crystalline materials, and is dependent on the crystal orientation, as this will affect the scattering of the electron beam. In other words, the BF image contains a lot of information about the specimen. An alternative to filter out all scattered electrons from the image, is to include only a single scattered reflection. This is known as dark field (DF) imaging. Just like BF imaging, selection is done using the objective aperture, but with the centre on a diffracted beam. This way, only a specific set of (hkl) planes will light up in the image, while vacuum will look black. This method is powerful when analysing structure or orientation domains in a specimen, as these domains may diffract electrons to separate reflections in a DP. Forming a DF image can therefore give insight in the shape and size of such domains. Centred dark field operation is a conventional way to do DF imaging, where the incident beam hits the specimen at an angle equal and opposite to the scattering angle. This will make the scattered electrons travel down the optic axis, making it easier to focus the image.

High Resolution

High resolution TEM (HRTEM) creates an image that is the result of complex diffraction and interference in the electron beam, and the technique allows for direct imaging of the atomic structure of the specimen. One of the difficulties with HRTEM is that the image is dependent on the phase difference of the transmitted electrons. Due to the somewhat imperfect lenses in the TEM, the method will image a point in the sample as Gaussian distribution, making it sensitive to overlap of the distributions. A thorough interpretation of HRTEM images is therefore not straightforward. However, it is possible to see lattice fringes in images, and these will give information about the crystal orientation on a very fine scale. It is thereby possible to do Fourier transforms of these images in order to gain information on the reciprocal space of the material, as described in section 2.1.3. In other words, the images produced in HRTEM may not be intuitive to understand, but the symmetry produced will give valuable information on the atomic structure.

Scanning Precession Electron Diffraction

Precession electron diffraction (PED) is a method used for obtaining localised DPs in the TEM. The technique uses a converged electron beam and rocks it to a hollow cone at a fixed

angle to the to the optic axis above the sample [28]. The beam is then de-rocked bellow the sample, the net result being equivalent to precessing the sample about a fixed electron beam parallel to the optic axis. The rocking motion of the beam can be translated to a similar motion of the Ewald sphere. This creates the advantage of recording multiple reflections over a range of angles, including the Bragg condition of each reflection. This will essentially integrate the intensity signal across each reflection intercepted by the Ewald sphere, resulting in a DP composed of many more reflections than for the conventional SAD technique [29].

By scanning the electron beam across the specimen, one can use PED and produce DPs pixel-by-pixel. This forms a four-dimensional SPED data set in which two-dimensional reciprocal information is available at each two-dimensional real space position. The technique is especially convenient when analysing grain structure and texture in a material. The data collected contains a vast amount of information and can be processed in various ways. The setup for PED can be seen in Figure 2.13 (c).

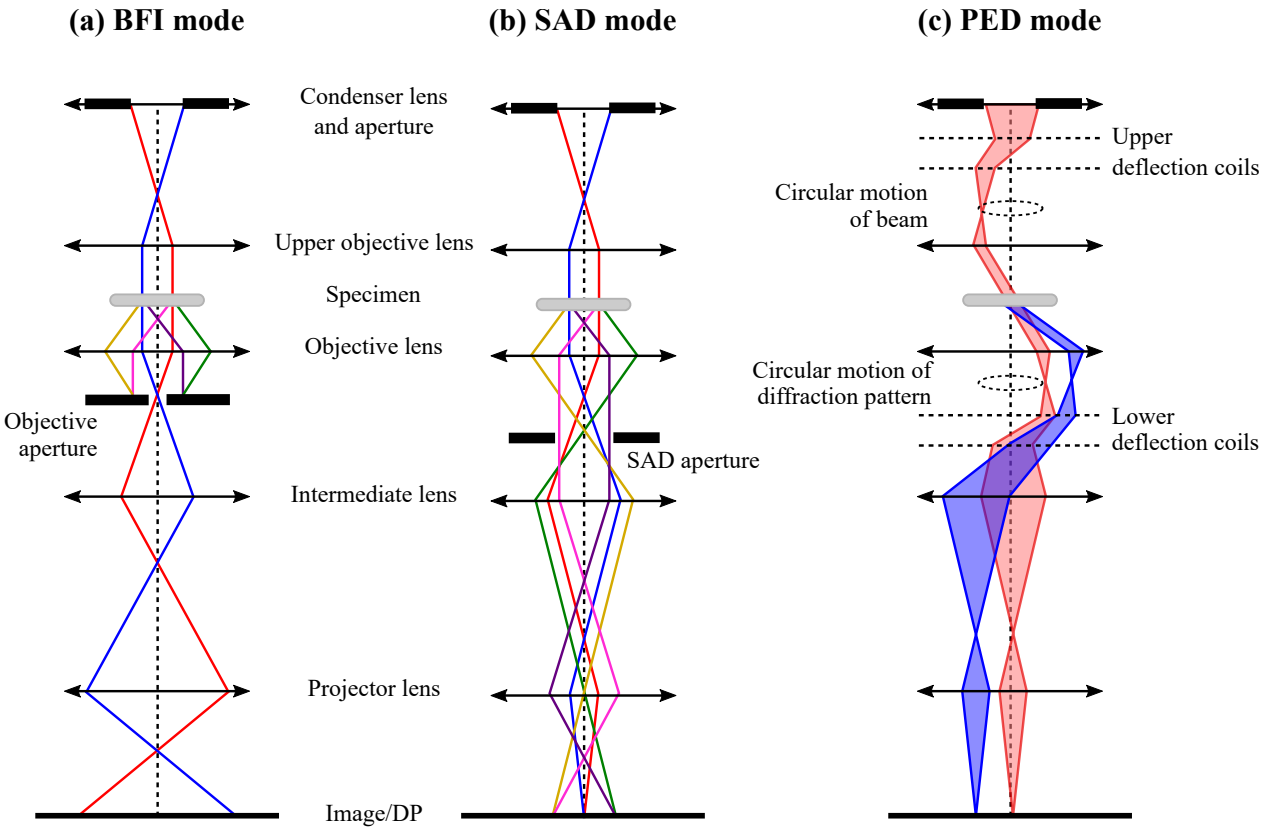

Figure 2.13: Simplified diagrams of ray propagation in the TEM. In bright field imaging (BFI) mode (a) the objective aperture selects the direct beam to form the final image observed on the viewing screed/CCD camera. In selected are diffraction (SAD) mode (b) the SAD aperture is used to select the electrons leaving the specimen at a certain angle to obtain a diffraction pattern. In precession electron diffraction (PED) mode (c) (adapted from [29]), the beam is kept at a fixed angle with respect to the optical axis. The upper and lower deflection coils impose a circular rocking motion of the beam, resulting in PED patterns containing more reflections than for SAD.

2.4 Texture Analysis

Section 2.2.2 explains the importance of controlled orientation in the material analysed. One of the main goals in this study is therefore to define grains in the thin film samples and map the orientations of these. Crystal orientation maps can be obtained by a number of different techniques, one being automated crystal orientation mapping in TEM (ACOM-TEM) by SPED as described in section 2.3.3. This section provides information necessary to understand the analysis of collected data in the study. A further explanation of how to assign crystal orientations to each PED pattern is covered in the experimental section 3.4.

2.4.1 Orientations

Each position in a crystal orientation map describes both the crystallographic structure and orientation of the crystal. The crystallographic orientation refers to how atomic planes in a volume of a crystal are positioned relative to a fixed reference [30]. In order to specify an orientation, it is necessary to define two coordinate systems. The *specimen coordinate system* has sample fixed coordinates that are, in principle, arbitrary. In general, however, they are chosen according to directions associated with the external form or shape of the specimen. The *crystal coordinate system* is specified by the directions in the crystal unit cell. For orthogonal symmetry (cubic, tetragonal, orthorhombic) it is convenient to adopt the axes [100], [010] and [001], as they already form an orthogonal frame. The orientation can then be defined as the position of the crystal coordinate system with respect to the specimen coordinate system.

There are numerous ways of describing a rotation of two coordinate systems with respect to each other and thereby representing the crystal orientation [30, 31]. One frequently used representation is the *pole figure*. By drawing a unit reference sphere centred on the crystal, one can define a pole as the point where a crystallographic plane normal intersects the sphere. A crystal's orientation can then be described by projecting its poles onto the sphere with respect to the specimen coordinates, making a pole figure. Similarly, the orientation of the specimen coordinate system can be projected into the crystal coordinate system, creating what is called the *inverse pole figure* (IPF). The IPF will in other words contain the angular distribution of a chosen specimen direction with respect to the crystal coordinate system. The poles in the three-dimensional unit sphere can be projected onto the equatorial plane, creating a two-dimensional stereographic projection. For cubic crystal symmetry, this projection can be divided by the symmetry planes into spherical triangles sufficient for IPF representation

[32]. The triangle corners are marked by that specific planes' symmetry elements, most commonly being [001], [011] and [$\bar{1}$11] for cubic systems.

2.4.2 Template Matching and Orientation Mapping

In order to determine the orientations of a SPED dataset, information on the crystal structure of the material analysed is needed. Composition, space group, lattice parameters and atom positions are used to simulate diffraction patterns for all possible orientations to create what is known as a *template bank*. These templates are then compared to the experimentally recorded PED patterns in a procedure known as *template matching*, as shown in Figure 2.14.

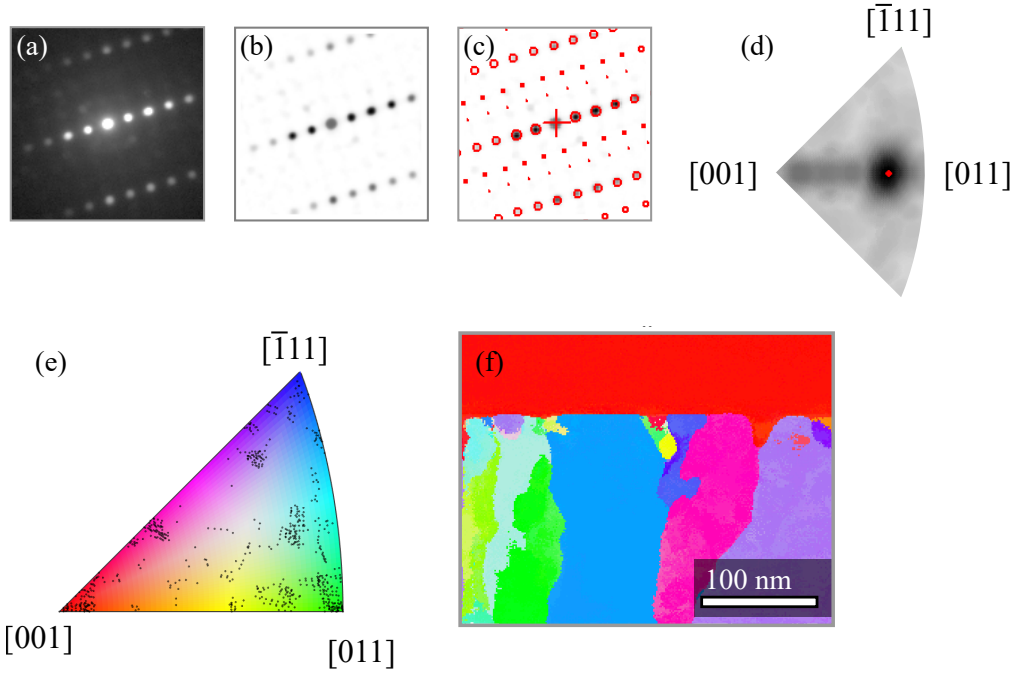

Figure 2.14: Example of template matching. An experimental PED pattern per pixel (a and b) is compared to every simulated template (c). The correlation index density map (d) shows the best match, i.e. most probable orientation. Finished template matching can be presented by an orientation map (f) with corresponding IPF (e).

Multiple templates can be used during the procedure in order to distinguish and index different phases or materials. The quality of the indexation from the template matching is quantified by the image correlation index Q, which is calculated for each PED pattern [33]. The value of Q is dependent on how well the intensity at each position in the PED pattern matches the template, with the best match being selected as the correct orientation. The

image correlation index Q is defined by Rauch et al. [34] as

$$Q(i) = \frac{\sum_{j=1}^{m} P(x_j, y_j) T_i(x_j, y_j)}{\sqrt{\sum_{j=1}^{m} P^2(x_j, y_j)} \sqrt{\sum_{j=1}^{m} T_i^2(x_j, y_j)}}, \tag{2.11}$$

where the diffraction pattern is represented by the intensity function $P(x, y)$ at each position (x, y) and each template i is described by the function $T_i(x_j, y_j)$. The highest Q value is selected as solution with a reliability parameter R, quantified by the ratio of the matching indices for the two best solutions, as

$$R = 100\left(1 - \frac{Q_1}{Q_2}\right). \tag{2.12}$$

It is common to use either Q or R, or both, to filter the orientation maps in order to improve the visibility of structural features.

After the template matching of a SPED dataset is complete, a map with information on phase, orientation, index Q and reliability R for each pixel is created. The orientation is given in the representation of Euler angles, which can be described as three sequential rotations of the crystal coordinate system through three (ϕ_1, Φ, ϕ_2) angles with respect to the specimen coordinate system [30]. It is common to present the maps visually by colouring the pixels according to the IPF of a chosen specimen direction as seen i Figure 2.14 (e) and (f). As the IPF only represents one direction of the three-dimensional orientation, rotations about the chosen axis are not visually present. Consequently, it is necessary to present maps along more than one specimen direction, usually being the three specimen coordinates **x**, **y** and **z**. By applying a subset of all crystal coordinates viewed along the specimen coordinates plotted into the IPF, the texture becomes easier to interpret.

There are multiple ways of presenting information on the material's texture. In some scenarios it may be more reasonable to present the pixel (or PED pattern) count of each orientation in a histogram. It is also possible to use orientation distribution functions (ODFs) in order to describe the probability of finding certain orientations within a given angular distance to a given axis. ODFs are continuous density distribution of orientations, calculated either from discrete data or from a series expansion method [30]. Calculated ODFs are often presented in pole figures with the orientation of crystal plane normals [001], [011] and $[\bar{1}11]$ plotted with respect to the specimen coordinates, essentially giving the same texture information as the equivalent IPFs.

2.4.3 Grain Boundaries

In order to better understand and separate the grains in orientation maps, one can define and mark grain boundaries. These are commonly found by thresholding the misorientations between adjacent data points. In order to avoid including many irrelevant boundary segments, the threshold angle is usually set to be above 1°, while at the same time being below 10° to ensure that all important regions are included. It is important to mention that the threshold-based method of reconstructing grains may not lead to desired results for regions where grains have gradual and subtle boundaries. These regions have no rapid changes in the orientation, resulting in multiple grains potentially being defined as one. The change in orientation may still be observed, by plotting the misorientation of each pixel to the mean orientation of the corresponding grain. Localised regions with high misorientation within a grain indicate missing grain boundaries.

The number of defined grains may vary, depending on if the orientation map has been filtered with respect to Q or R prior to the thresholding. Even a filtered map may contain some pixels with wrongly indexed orientations, resulting in the possibility of small irrelevant grains being defined. It is therefore recommended to filter out small grains before defining the final grain boundaries. As only a two-dimensional view of the grains is presented, the size refers to the area of the grains. Rauch and Véron recommend further removal of unreliable grains, based on the reliability of the pixels within each grain [35].

It is important to mention that there is a possibility of error in the grain boundaries defined through analysis of SPED data. The orientation of the grain boundaries' planes in a polycrystalline material might not be perpendicular to the incoming electron beam, resulting in overlapping grains. Consequently, the recorded PED patterns may contain DPs from multiple crystals, resulting in poor template matching in these regions. All in all, the SPED technique is a powerful tool. The thousands of DPs stored in each dataset contain a wealth of information about the material analysed. Still, one should keep in mind that there are limitations imposed by both the recording method and subsequent data analysis.

3 Experimental

This section starts with a brief presentation of the synthesis of the material analysed. This is followed by a detailed description of the sample preparations before the techniques used in the TEM are presented. Finally the processing of collected data is explained.

3.1 Thin Film Synthesis

The materials studied in this project are KNN thin films grown on (100) oriented strontium titanite (STO) substrates. Five different samples were made, using different heat treatments. The thin films were synthesised at the Department of Material Science and Engineering, NTNU, by PhD candidate Nikolai Helth Gaukås. As the synthesis of thin films is not the focus of this study, details concerning the growth are omitted. However, a brief introduction to the deposition technique used will be explained and is based on the thesis written by Dale [36].

Various deposition techniques described in literature have been used to successfully produce KNN thin films [37, 38]. The thin films used in this project were synthesised using a sol-gel process with chemical solution deposition (CSD). This technique uses a liquid precursor solution and forms thin films during thermal treatment. One of the important aspects when making the precursor is the ratio between KN and NN, which for these samples were made so that the potassium to sodium ratio in the final KNN thin films was 50/50. It is also important to mention that the precursor for these films has been made using non-toxic chemicals in an aqueous solution. There are few reports on KNN thin films being synthesised this way, and it makes the process cost-effective as well as more environmental friendly [39, 40].

After the solution was made, the thin films were synthesised through multiple cycles of deposition followed by pyrolysis, essentially building the thin film samples layer by layer. An illustration of the cycle is given in Figure 3.1. The solution was spin coated onto the substrates at 3500 rpm for 40 seconds. Spin coating is a procedure where a small amount of the solution is applied to the centre of the substrate, which is then rotated in high speed in order to spread the material by the centrifugal force. This deposition made the thin film spread out in a circular shape, resulting in low quality film at the corners of the substrate. It is not guaranteed that the solution levelled out evenly during spin coating, implying a possibility of the thin films being of higher quality close to the centre.

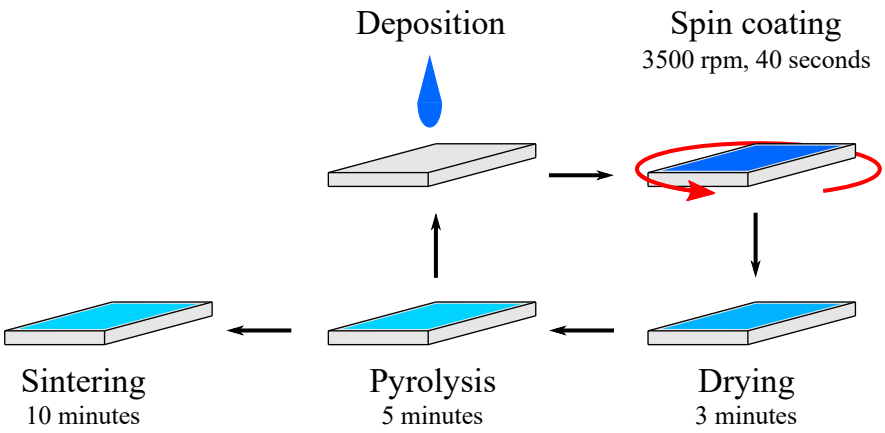

Figure 3.1: An overall illustration of the synthesis route, adapted from [36]. The precursor is deposited on cleaned (100) oriented STO substrates. The solution is the spin-coated and dried on hot plate before being pyrolised. This cycle is repeated until sufficient thickness is achieved, before the film is finally sintered.

Before pyrolysis, the films were dried at 200 °C for three minutes on a hotplate. Pyrolysis is often referred to as the heat treatment where the organic molecules are removed through decomposition to volatile organic molecules such as CO_2. A layer of thin film with a thickness between 10 and 20 nm was formed through pyrolysis at different temperatures for five minutes. Two samples were made using a temperature of 450 °C, two at 500 °C and one at 550 °C. The pyrolysis stage plays a key role in the crystallisation of the material, as the pyrolysis temperature affects the nucleation and growth process [39]. At lower temperatures it is energetically beneficial for the material to nucleate on the substrate, resulting in epitaxial growth and texture in the thin film. This is known as heterogeneous nucleation. If the temperature is raised above a critical point, homogeneous nucleation may occur, which means nucleation appear somewhere within the bulk of the film, i.e. away from a surface. This critical point exists somewhere between 500 and 600 °C [15].

The deposition and pyrolysis were repeated a total of fifteen times until a desired thickness of about 200 nm was achieved for each sample. Finally, crystallisation and densification of the films were obtained by sintering at 700 °C for ten minutes in a tube furnace. In addition to removing potential pores in the material, the final stage makes the multiple layers in the film bond better together. Two of the samples were not sintered, one with pyrolysis temperature of 450 °C and one with 500 °C. These samples were made in order to analyse the change in the films before and after sintering.

3.2 TEM Specimen Preparation

To be able to analyse a material in the TEM, the specimens need to be prepared. There are multiple factors to consider when preparing a sample, as the techniques must not affect what is to be measured, unless the effect is known. Therefore, different sample preparation techniques have been developed to be more suitable for different materials. The main goal of TEM specimen preparation is to make the region of interest (ROI) electron transparent without affecting the structure of the material. Two different preparation techniques were used in this experiment: focused ion beam (FIB) and precision ion polishing system (PIPS). This section starts with the overview of the sample before and after it was cut. Then the different preparation techniques are presented.

3.2.1 Sample Overview

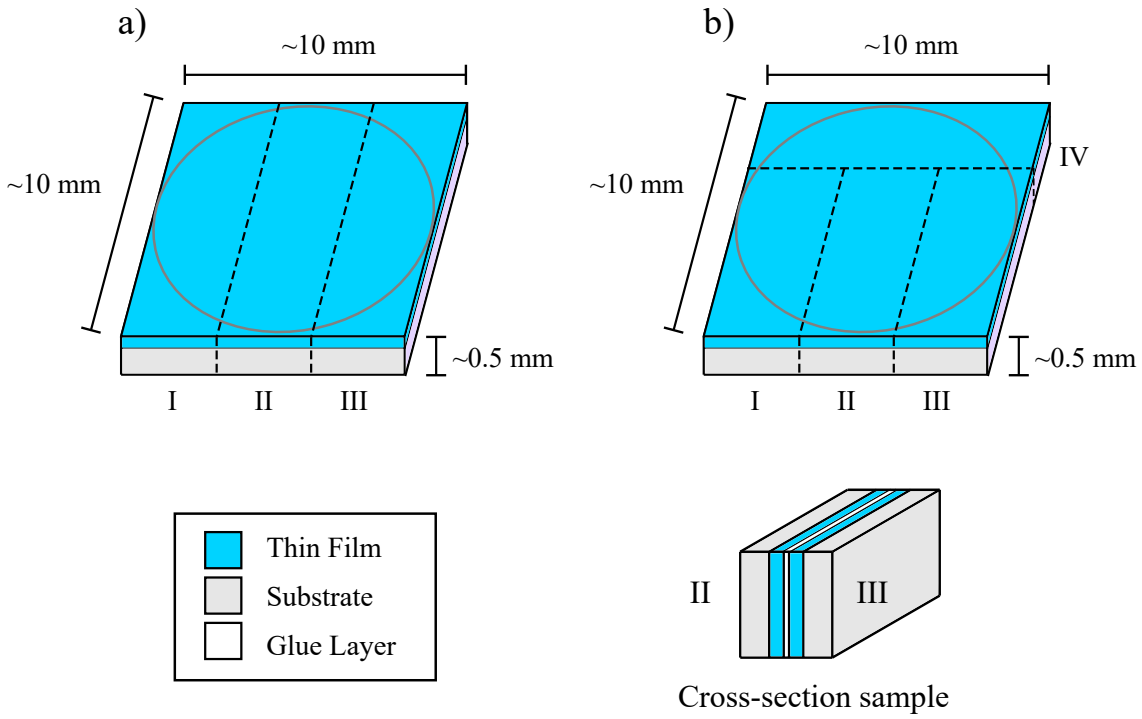

Figure 3.2: Illustration of the thin films analysed in the project. The thickens of the thin film and glue layer is exaggerated. The samples were cut using either pattern a) or b) presented with dotted lines, both resulting in pieces with about 3 mm width. Cross-section samples were made by gluing the middle piece (II) and one side-piece (III).

A total of five KNN thin films were analysed in this study. The different film samples were initially cut into smaller pieces to be used for different preparation techniques. The

illustration presented in Figure 3.2 shows the dimensions of the samples as well as the cutting patterns used. As mentioned, only a circular area of the thin films were of high quality, limiting the amount of usable material. In order to analyse the variations in microstructure along the film thickness, cross-section samples were made. The films synthesised using 450 °C were cut using pattern (a), while the ones synthesised using 500 °C were cut using pattern (b). The latter pattern was used in order to produce FIB-specimens from piece (IV). For all these films, piece (I) was made for potential plane view specimens. The final film synthesised using 550 °C was originally used in the author's project thesis of fall 2017 [11], and was cut using pattern (a). All cutting procedures were done using a *Testbourne Model 650 Low Speed Diamond Wheel Saw* equipped with a 150 µm *Allied High Tech Wafering blade*. The samples were mounted with wax on a glass plate using a hotplate at around 125°C. The glass plate was then mounted to the saw for cutting. The parts marked II and III were glued together using *Araldite Rapid* 2-part epoxy adhesive, in order to make cross-section samples. It was important that the glue layer was as thin as possible, as a thick layer could lead to problems occurring in specimen preparation as well as a high probability of falling apart. This was achieved by putting the sample in a clamp holder, compressing the layers while the glue dried. The cross-section sample is illustrated in Figure 3.2.

The cross-section samples were cut into smaller pieces with dimensions of 1 mm × 1 mm × 3 mm before being used for PIPS preparation. This resulted in 6 pieces for the film synthesised using 500 °C, and 10 for the rest. Table 2 presents an overview of the different specimens studied in the thesis. The specimens have been named after what thin film sample they originate from, indicating pyrolysis temperature and if they have been sintered or not. All specimens have been extracted close to the centre of the film. As the specimens produced by PIPS contained two layers of thin film, an extra notation in the name has been included later in the text to distinguish them. The notation *-II* and *-III* refers to which piece (as presented in Figure 3.2) the thin film originates from.

Table 2: The specimens studied and the methods used for TEM preparation.

Sample name	**Pyrolysis temperature [°C]**	**Sintered**	**Preparation**
P450N	450	No	PIPS
P450S	450	Yes	PIPS
P500N	500	No	PIPS
P500S	500	Yes	FIB
P550Sa	550	Yes	FIB
P550Sb	550	Yes	PIPS

3.2.2 Focused Ion Beam Preparation

A *FEI Helios NanoLab DualBeam FIB* at NTNU NanoLab was used to prepare selected samples, using a standard lift-out technique. As the FIB is an advanced instrument, it requires much training and experience to handle properly. For this reason, the author did not participate in the making of the FIB specimens. Specimen *P550Sa* was prepared by Senior Researcher at SINTEF Materials and Chemistry, Per Erik Vullum during the fall of 2017 while the author observed the process. Specimen *P500S* was prepared by PhD candidate Adrian Lervik in the spring of 2018. The workings of the FIB instrument are not the focus of this project and will not be discussed or presented in detail. However, some important aspects on the technique are outlined and is adapted from [11].

The samples used for this preparation was of the dimensions $1\,\text{mm} \times 3\,\text{mm} \times 10\,\text{mm}$. The reason for using such a large area of the original piece was to acquire a TEM specimen close to the centre of the thin film. This area was suspected to be of higher quality due to the spin coating mentioned in section 3.1. The FEI system's DualBeam technology combines scanning electron microscope (SEM) analysis and FIB milling, making the system capable of producing ultra-thin samples for TEM. Protective layers where deposited onto the samples in order to avoid charging from the electron beam as well as protecting the material's crystalline properties. Before placing the sample in the machine a $\sim 40\,\text{nm}$ layer of Pt/Pd (80/20) was sputter coated on the surface, using a *Cressington Sputter Coater Model 208 HR*. By introducing gases in close proximity to the surface of the sample within the vacuum chamber of the system, a thicker layer ($\sim 2\,\mu\text{m}$) of carbon was deposited on the desired surface by first using the electron beam, and then the gallium ion-beam. The TEM specimen was then cut out of the sample using the high energy ion-beam. First, several ditches were dug straight down through the film and into the substrate around the protected area, leaving one side untouched, as presented in Figure 3.3 (a). The sample was then tilted and cut in order to separate the piece covered by the protective layer, making a "bridge" which would be used as specimen in TEM. A high precision movable needle-like *Omniprobe AutoProbe* was then attached, before cutting the remaining side and lifting out the sample. The sample was then mounted on a *Copper FIB Lift-Out TEM Grid*, before the probe was cut off, as seen in Figure 3.3 (b). Finally, the sample was thinned through a series of milling steps using the ion-beam. To minimise the ion-damage, the last thinning was done using reduced voltages.

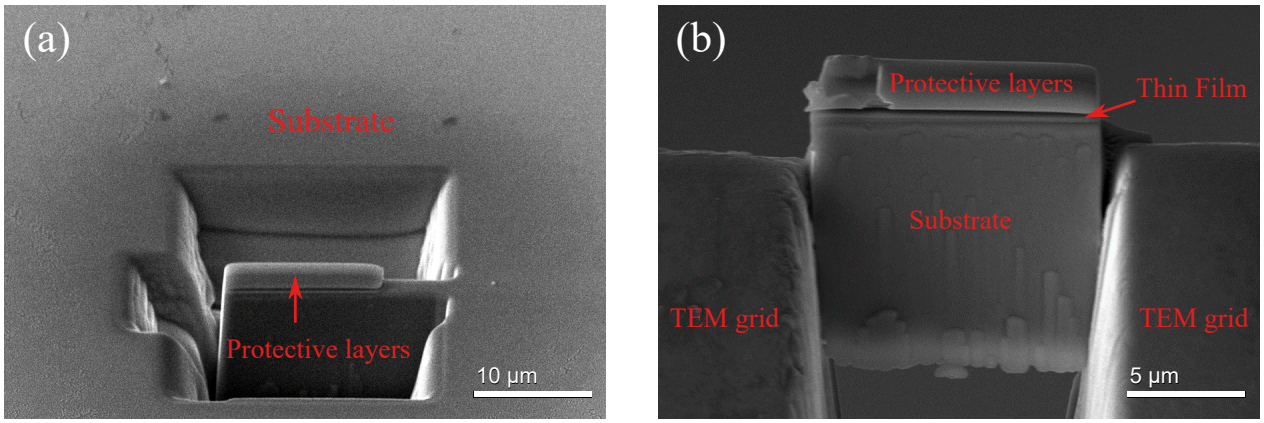

Figure 3.3: SEM images obtained during FIB preparation of specimen *P500S* by PhD candidate Adrian Lervik. (a) shows the excavated ditches around the protected "bridge" area. The sample is cut, moved with an AutoProbe and mounted to the TEM grid presented in (b).

Some observations were made during the preparation in the FIB-system by using the SEM analysing properties of the machine. The initial protective layer of Pt/Pd (80/20) had attached well to the sample, creating an even and dense layer on the surface. Another important observation occurred during thinning of the TEM specimen. If the sample was thinned too much, a spontaneous bending in the STO material could arise.

3.2.3 Precision Ion Polishing

As mentioned in section 3.2.1, pieces of dimensions 1 mm × 1 mm × 3 mm were cut from the cross-section samples to be used for PIPS preparation. In order to maintain structural stability of these specimens, two pieces of silicon were glued to each side. The specimens consisted then of the layers silicon - substrate - thin film - substrate - silicon, with glue between each layer. The first step in this preparation technique is thinning the sample. Each specimen was mounted on a clean dimpling stub with wax, so that the interface-plane with length 3 mm was parallel to the dimpling stub's surface. Using a *Struers RotoPol-21* grinding machine, the samples were polished with Grit P1200/2500/4000 grinding papers until the surface was as smooth and flat as possible. The specimens were then turned around, with the polished side facing down on the dimpling stub. The grinding was then repeated until the thickness of the samples was about $80 - 90\,\mu m$. The thickness was measured using a calibrated *Olympus BX60* VLM.

The next stage of the preparation technique is making a dimple in each sample. The dimple needs to be centred at the ROI, in this case the centre of the specimens. The dimples were

made using a *Fischione Model 2000 Dimpling Grinder*. 3 µm *Allied High Tech Polycrystalline Diamond Compound* mixed with deionised water was used as grinding lubrication and the grinding rate was set to 1.5 µm. The instrument's measurement of grinded depth had a high uncertainty. Precautions were therefore made by removing the sample before the dimpler grinded too deep. The estimated thickness in the bottom of the pits made in this study varied between 20 µm and 35 µm.The preferred thickens was 20 µm, as the material tended to break if the dimple was deeper. Finally, the specimens were removed from the dimpling stubs using acetone. Afterwards it was cleaned in ethanol for about five minutes.

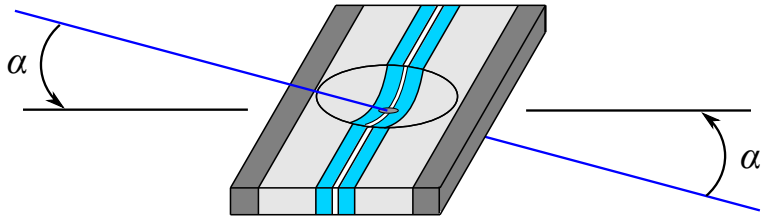

Figure 3.4: Illustration of a specimen subjected to argon beams, sputtering a hole at the centre at a given angle α. The thickness of the layers is exaggerated.

The final stage of preparation is the ion polishing. This was done using a *Gatan Precisison Ion Polising System Model 695* (PIPS). The machine uses argon ions to sputter a hole through the bottom of the dimple, as illustrated in Figure 3.4. The PIPS uses a special set of spring-style sample holders called *DuoPost*, which holds the specimen with two clamps. Each specimen was mounted with the dimple centred and then inserted in the PIPS vacuum chamber before being cooled using liquid nitrogen. Two opposing argon beams angled relative to the sample polished until a hole was observed. As the specimens were relatively thick, an acceleration voltage of 4.5 eV at angle 4.5° was used in the initial sputtering process.

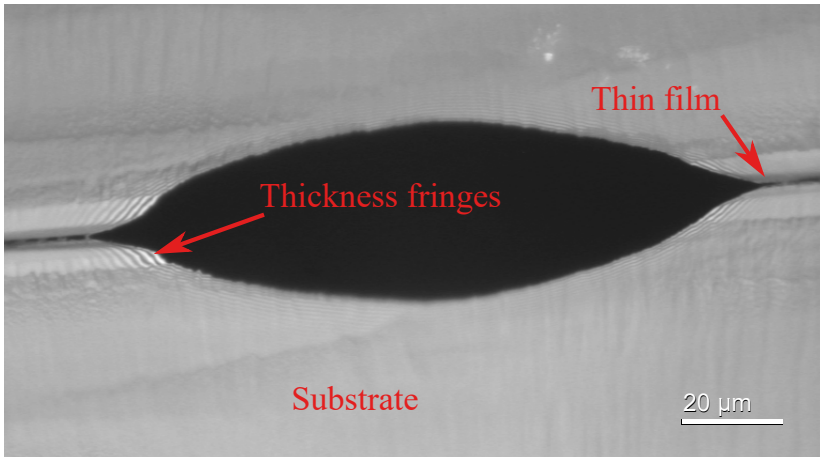

Figure 3.5: Image of a PIPS specimen taken with an Olympus BX60 VLM. Thickness fringes can be observed on both corners of the hole, indicating that the ROIs are electron transparent.

When a hole was observed, the angle was changed to 4° and acceleration voltage reduced to 4 eV. In order to avoid amorphous layers created by the argon ions on the specimens' surface, the voltage was gradually lowered. Different time and voltage intervals were used for the various specimens produced in this study. *P450N* and *P500N* were polished at ten-minute intervals with a reduction of 0.5 eV each time until the acceleration voltage was at 0.5 eV before finishing with two final intervals at 0.25 eV and 0.1 eV. This made the holes relatively big, and proved to be unnecessary after various trials. The rest of the specimens were therefore polished for two minutes at 4 eV, 2 eV and 1 eV and finally for five minutes at 0.5 eV, 0.25 eV and 0.1 eV, respectively. After the polishing was completed, the specimens were inspected in a *Olympus BX60* VLM. The finished specimens contained two regions of interest, located at the corners of the hole where the two layers of thin film meet. Thickness fringes were observed at the ROIs, indicating that the areas were electron transparent, as illustrated in Figure 3.5. Before using it in the TEM, the specimens were mounted on a copper TEM grid with *Araldite Rapid* 2-part epoxy adhesive.

3.3 Characterisation

3.3.1 TEM Operation Modes

The TEMs used in this study were a *JEOL JEM-2100* and a *JEOL JEM-2100F*, and are part of the Norwegian Centre of Transmission Electron Microscopy (NORTEM) infrastructure at TEM Gemini Centre, NTNU, Trondheim. These are equipped with a LaB_6 thermionic electron gun and a tungsten FEG, respectively. Both microscopes were operated using an acceleration voltage of 200 kV. The 2100 microscope is equipped with a *Gatan 2k Orius* CCD camera using *Gatan Digital Micrograph* software [41] for acquiring images. The 2100F is installed with a *Gatan 2k UltraScan* bottom mounted CCD camera, also using the *Gatan Digital Micrograph* software. In addition to this, the 2100F is equipped with a *NanoMegas ASTAR* hardware and software [42] package for performing SPED. An *Allied Stingray 046B ASG* camera is mounted in the binocular stand outside the microscope column to collect the PED patterns from the microscope viewing screen. A *JEOL EM-31640 Specimen Tilting Beryllium holder* with possibilities for tilting both parallel and orthogonal to its axis up to ±30° was used as holder for all specimens studied.

BF images of all specimens were obtained in the 2100 microscope by operating the TEM as explained in section 2.3.3, in order to get an overview of the thin films and study the microstructure. HRTEM images of the thin film and substrate interface were acquired in the

2100F microscope to study the polycrystalline nature of all specimens. The interface-region was of special interest, as potential epitaxial growth could quickly be observed by analysing lattice fringes in the HRTEM images.

3.3.2 Acquisition of SPED data

SPED data was acquired while operating the TEM in what is known as nano beam diffraction (NBD) mode. This is when the condenser lenses create a probe of sub-nanometer diameter nearly parallel to the specimen with a semi-convergence angle $\alpha < 1.5$ mrad [43]. The 2100F microscope was used, as the FEG source creates DPs readily visible on the fluorescent screen in a fraction of one second. As a result, series of patterns may be recorded by the use of the externally mounted camera in a relative short amount of time. In order to ensure acquisition of localised PED patterns, an alignment of the double-rocking movement of the precessing electron probe was performed. This was done entirely in diffraction mode, by using the shadow image in the bright field diffraction disk, and reduce the effects of the rocking and precessing movement on it. Barnard et al. [44] describe that the goal of the alignment is to coincide the probe focal plane and the pivot point plane of the precessing movement with the specimen plane. The procedure can be summarised and described in a few steps as follows:

1. Insert a large condenser aperture and over-focus the electron probe using the condenser lens.
2. Find a region with highly visible features, e.g. the interface between thin film and substrate, and activate precession by introducing both precession angle (ϕ) and frequency (ω).
3. Obtain a static diffraction disc with a sharp edge using the de-rocking adjustment.
4. Minimise the motion of the shadow image by adjusting the pivot point of the precessing movement. Sharp features should be visible and not change when turning precession on/off.
5. Reduce the defocus and repeat steps 3 and 4 until no further improvement is seen.
6. Finally refocus the probe using the condenser lens and insert a small condenser aperture.

The precessing probe was aligned with the values $\phi = 0.8°$ and $\omega = 100$ Hz, for all scans made in the study. The size of the probe spot and the semi-convergence angle were set to

1.0 nm and 1.0 mrad, respectively. The probe was then scanned over the specimen with a step length of 1.28 nm, creating a raster image of the region of interest. The size and shape of the image may vary, however, it is recommended that the shape is set to be square. This is because a rectangular shape may result in complications when processing the data. The orientation of the scan was rotated so that the thin film was oriented as parallel as possible to the coordinate axes of the recorded map. This was because the orientation of the substrate was known and could be used as reference for the specimen coordinates when analysing the produced data. The reciprocal space of the obtained PED patterns were therefore rotated relative to the real space. The camera length was set to 40 cm with an exposure time ranging from 20 to 40 ms, matching the integer number of complete precessions.

SPED datasets were acquired of all thin film samples, except for *450S* due to it being unstable in the TEM. Nine square-shaped regions were scanned in series of specimen *P500N* and *P500S*, and eight of *450S*. One large rectangular scan was performed on *P550Sa*. The total length of film scanned for each specimen is presented in Table 3.

Table 3: Total length of film scanned for each specimen

Specimen	*P450S*	*P500N*	*P500S*	*P550Sa*
Scanned Length [µm]	1.57	1.93	1.73	1.28

3.4 Data Processing

The localised diffraction patterns in a SPED dataset contain large amount of information, and there are many different ways of extracting this information. *NanoMegas ASTAR* software was used in this study to acquire the PED patterns, as well as creating template banks and preform template matching. As described in section 2.4.2, the produced orientation maps consisted of one orientation per pixel with a correlation index Q and its reliability R. This dataset was further analysed in the open source Matlab toolbox *MTEX* [45, 46] to obtain information about the texture and microstructure of the thin films. This section describes the process made in both ASTAR and MTEX, while relevant source code is included in appendix A.

3.4.1 Template Matching

The orientation maps contained one PED pattern per pixel and were acquired by using ASTAR hardware and software [42]. The different template banks used in the study were

made in ASTAR *Diffgen*, using the information given in appendix C, which are based on the information presented in section 2.2.1. It is important to mention that the monoclinic template bank was based on KNN with a 30/70 potassium to sodium ratio, as this was the only monoclinic structure described in literature with atomic positions included. The local crystallographic orientations were identified by template matching as explained in section 2.4.2 by the use of ASTAR *Index*. Three templates for KNN were made to compare the matching quality of each of them. Mainly the pseudo-cubic template was used when producing the results presented in section 4. As the templates for KNN and STO are so similar, it is hard for the ASTAR software to distinguish the two during template matching. In order to avoid incorrect indexing, only the KNN template was used. Consequently, the thin film and substrate could not be separated in the produced orientation maps. The STO template was used for calibration of camera length and distortion in the recorded PED patterns before initialising template matching. This was because the substrate was at zone-axis at for all scans, creating patterns with high symmetry. The produced orientation maps were exported from ASTAR *MapViewer* as ANG files for subsequent processing in the MTEX software.

3.4.2 Mapping of Orientation Data

MTEX was used to inspect and present the texture information in the recorded SPED datasets. The toolbox can be used to gain insight in various phenomena related to texture such as size, shape and location of various grains as well as orientation variations within individual ones. The orientation maps are described in MTEX by a coordinate system with the x-axis along the horizontal view, y-axis along the vertical and the z-axis directed into the plane. This have been used as specimen coordinate systems and will be referred to as such.

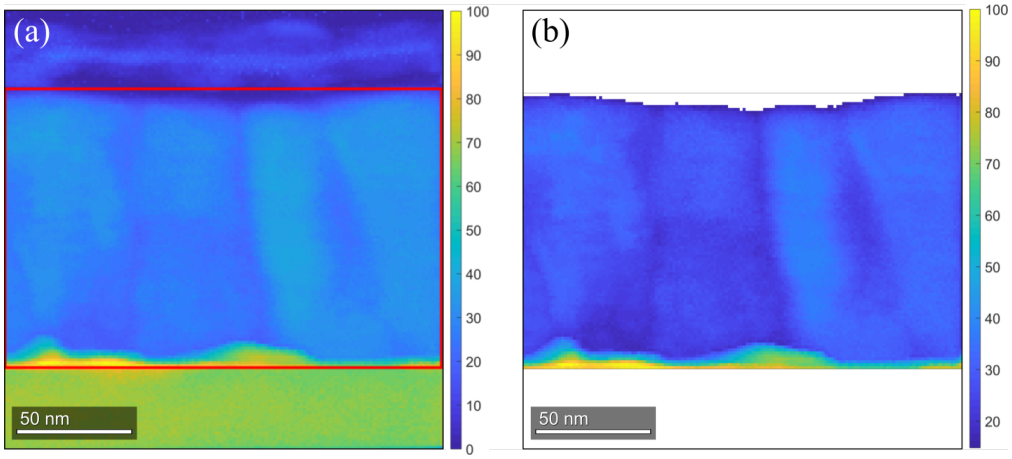

Figure 3.6: Map of correlation index Q with region of interest marked in red (a) and finished cropped and filtered (b).

All datasets contained redundant information such as regions of substrate and vacuum. The maps were therefore cropped to only contain the region of interest before being processed further. All maps were oriented with the film approximately parallel to the x-axis. Consequently, the maps were cropped along the y-axis only, with boundaries set at the interface between the thin film and substrate and at the edge of the film. As only a KNN template bank was used, the STO substrate and KNN thin film was not distinguished during template matching, thus resulting in some complications for an exact definition of the interface between them. Due to the materials producing close to identical DPs and as the substrate was at zone, it was given a relatively high correlation index Q (marked green in Figure 3.6). However, by close inspection of the index maps, it was possible to observe a relative sharp transition line where Q became higher. It was assumed that this thin region (marked yellow in Figure 3.6) was an epitaxial layer of KNN, as the increase in Q could be explained by PED patterns matching better with KNN than STO. The transition line was therefore used as indication of the interface. In order to remove the remaining unwanted regions such as vacuum or protective layers, the datasets were filtered. The average correlation index (Q_{mean}) was calculated for each dataset, and all measurements with an index score below 0.5 Q_{mean} were removed from the map. An example of cropped and filtered dataset is illustrated in Figure 3.6.

As explained in section 2.2.2, the piezoelectric properties of the thin films are dependent on how well the crystals/grains are aligned. Hence, orientation maps with corresponding IPFs of all the filtered datasets were produced. Pole figures were created to complement the information gained from these maps, enabling study of the texture of the thin films. In order to ease the interpretation of the pole figures, orientation distribution functions (ODFs) were calculated for the same crystal coordinates.

To gain information on the distribution of the orientations, the misorientation of each recorded PED pattern relative to the substrate was calculated. The mean orientation of a selected region in the substrate of each of the unfiltered datasets were calculated and used as reference for these calculations. The results have been plotted in histograms, however, as the plots show counts of PED patterns, the peaks observed may originate from single grains which are relatively large in size. In other words, the results are dependent on the area inspected, which can affect the overall distribution presented, thus resulting in a misrepresentation of the relative orientations of all the grains in the film. The misorientation of the PED patterns were therefore also presented in maps, thus enabling a study of the origin of them.

The definition of grains in the datasets proved to be more difficult than first anticipated, and

will be discussed in section 5.2.2. A threshold angle of 4° was first used, before the boundaries were redefined after excluding grains smaller than 20 nm^2. These grains were most likely a result of wrongly indexed pixels and could therefore be neglected. Snippets of code used for processing and analysis of the orientation data in the different specimens are included in appendix A.

3.4.3 Image Processing

All images produced in TEM and Matlab were imported to the open-source vector graphics editor *Inkscape* [47] for editing before being included in the report. The various maps produced from SPED data where oriented so that the substrate was located in the same direction for all maps. DF images were traced to bitmaps in Inkscape in order to colourise and combine them to one image. Fast Fourier transformations (FFTs) of the HRTEM images were created using the FFT function in *Gatan Digital Micrograph* [41]. The thickness of the films was measured using the same software.

4 Results

In this section the results from the characterisation of the five KNN samples are presented. As a total of five specimens were analysed, some of the collected data have been omitted from the section and are presented in the appendix. First, the microstructure of the thin films is presented in BF, DF and HRTEM images. Then the thin film texture and grain size of each specimen are presented from analysis of the crystal orientation information from processed SPED datasets. This includes orientation maps, pole figures and calculation of misorientation relative to the substrate. Finally, X-ray diffraction patterns made by Nikolai Helth Gaukås have been included to complement the results produced in TEM. The results are discussed in section 5.

4.1 Thin Film Microstructure

A plane-view SEM image of specimen *P500S* showing the surface of the thin film, presented in Figure 4.1, was obtained during FIB preparation. The surface is rough and faceted with grains of varying sizes with voids between them. Quick measurements of the image indicate diameter of the grains ranging from 30 to 170 nm.

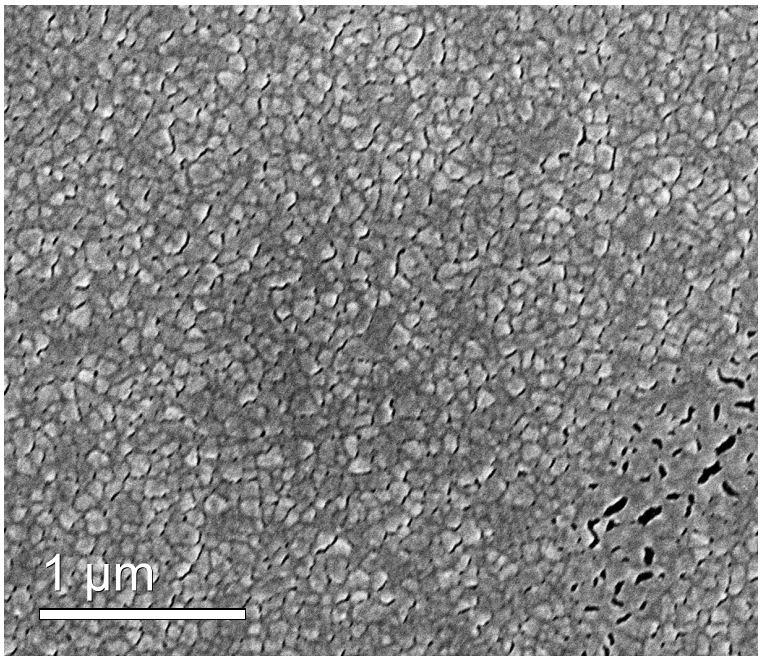

Figure 4.1: SEM image showing top view of specimen *P500S*, obtained during FIB preparation by PhD candidate Adrian Lervik.

The thin film had partly delaminated from the substrate for the two unsintered specimens during TEM sample preparation. Figure 4.2 (a) shows how all the electron transparent film had delaminated in specimen *P450N*. The inset shows how the film moved after being studied for a period in the TEM, making it unusable for further inspection. Figure 4.2 (b) shows that only one of the thin film layers had delaminated in specimen *P500N*. The other thin film layer remained intact during TEM inspection, and was used for further analysis.

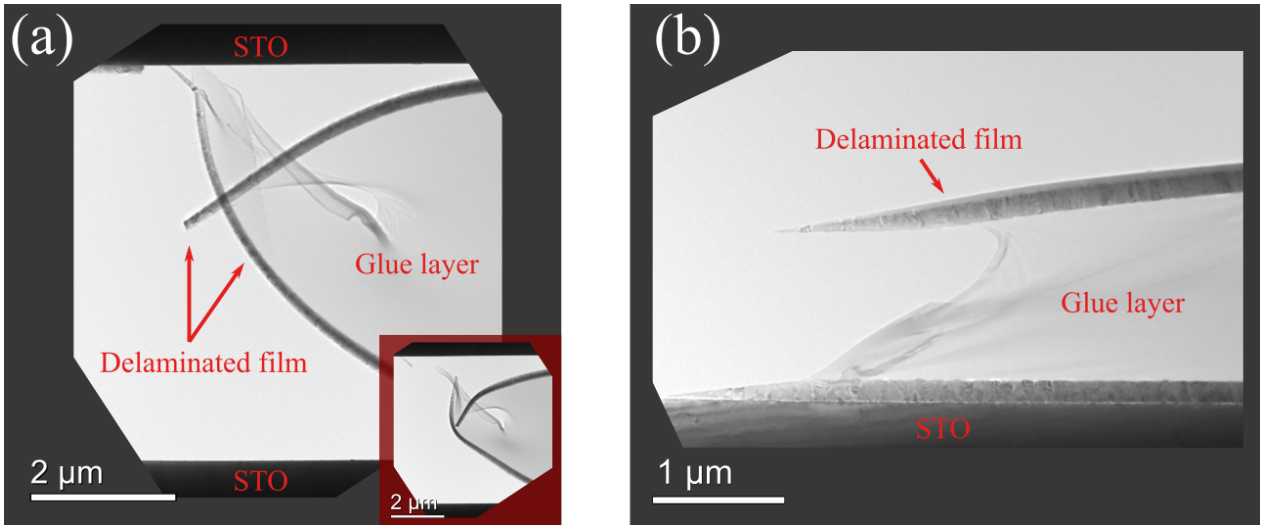

Figure 4.2: BF images of specimen *P450N* (a) and *P500N* (b) obtained in TEM. All electron transparent thin film material has delaminated from the substrate in (a), while only one layer has in (b). The inset in (a) shows the change after being exposed to the electron beam for a period in TEM.

Figure 4.3, 4.4, 4.5 and 4.6 show the microstructure of the thin films in BF images of specimen *P450S*, *P500N*, *P500S* and *P550S*, respectively. A pronounced column growth morphology is observed in all specimens. The majority of the grains extends from the substrate throughout the thickness of the film, except for specimen *P450S*. Figure 4.3 shows how the columnar growth only dominate the lower part of the film in this specimen, stretching only through two thirds of the film thickness. Another important observation is the thin bright line between substrate and film in specimen *P500N*, shown Figure 4.4. This may be a result of the film partly detaching from the substrate.

The average thickness for each film, presented in Table 4, was calculated from multiple measurements in each specimen. As samples produced in PIPS were based on a dimple with the film thickness decreasing close to its centre, the measurements were only made at regions where the film surface was parallel to the substrate.

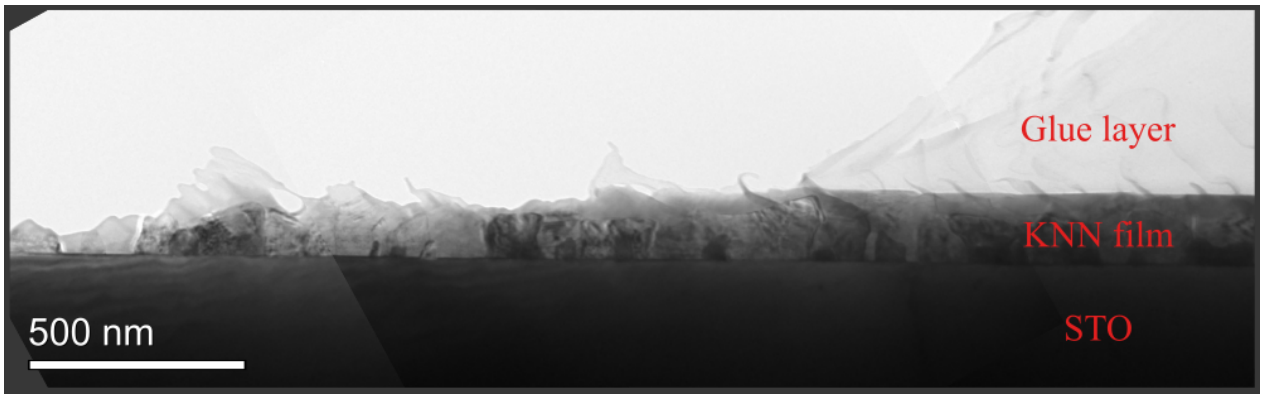

Figure 4.3: BF image of specimen *P450S-II* obtained in TEM. The image is a combination of three separate BF images.

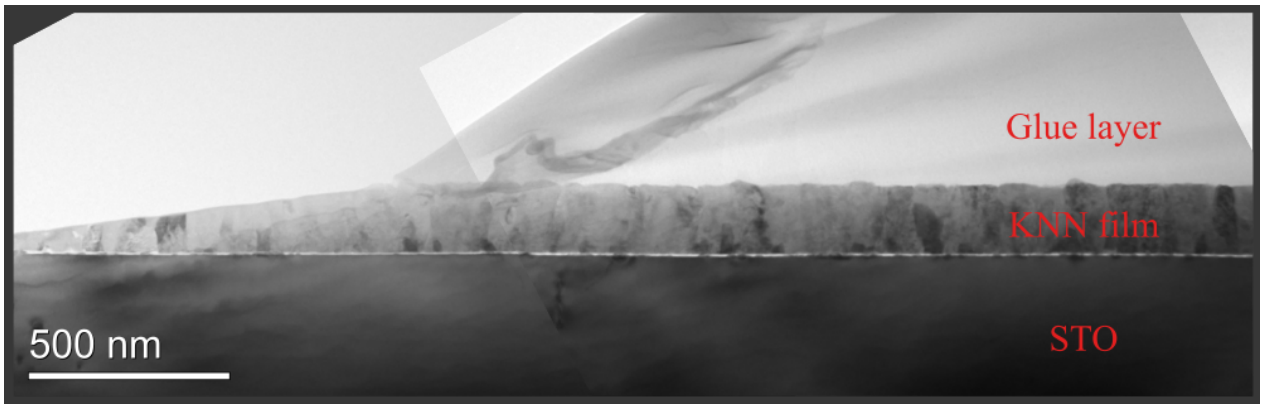

Figure 4.4: BF image of specimen *P500N-III* obtained in TEM. The image is a combination of three separate BF images.

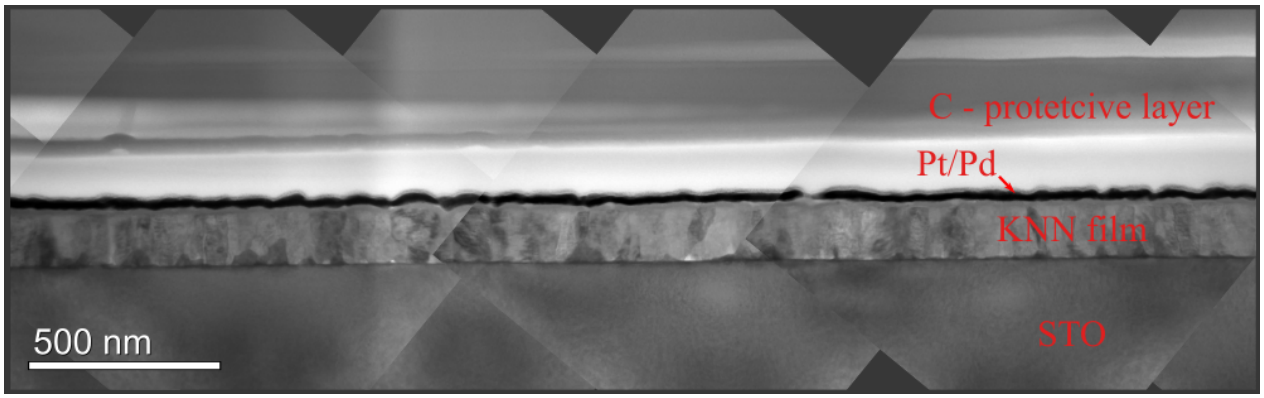

Figure 4.5: BF image of specimen *P500S* obtained in TEM. The image is a combination of six separate BF images.

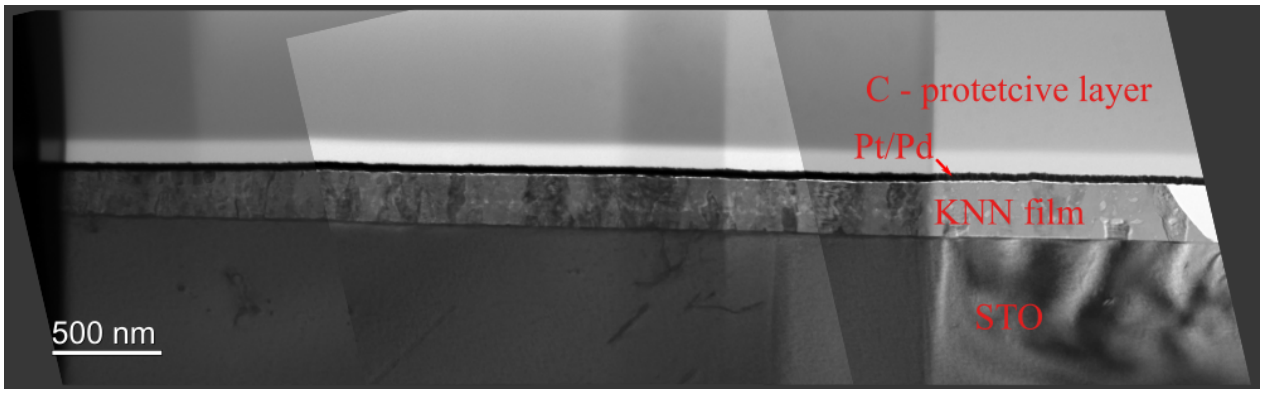

Figure 4.6: BF image of specimen *P550Sa* obtained in TEM. The image is a combination of three separate BF images.

Table 4: Average thin film thickness measured for each specimen. Cross-section specimens consisting of two layers of thin film are separated by the notation *II* and *III* referring to the pieces presented in Figure 3.2.

Specimen	Average Thickness [nm]
P450N-II	251
P450N-III	219
P450S-II	165
P450S-III	158
P500N-II	225
P500N-III	171
P500S	154
P550Sa	240

Figure 4.7 shows one of the HRTEM images obtained from specimen *P450S*, and was acquired from the region presented in Figure 4.3. Fringes are observed in both the substrate and thin film, indicating the directions of the crystal planes. A common orientation of KNN and STO may be observed to the right of the image (marked with a red line), indicating epitaxy. This indication of a thin epitaxial layer was observed along most of the substrate in all specimens with a thickness mainly ranging from 1 to 3 nm, some parts extending further into the film, indicating epitaxial grains. It is important to mention that there were relatively large regions in each specimen where it was not possible to obtain clear HRTEM images of the interface. The area marked by the red square to the left in Figure 4.7 indicates such a region.

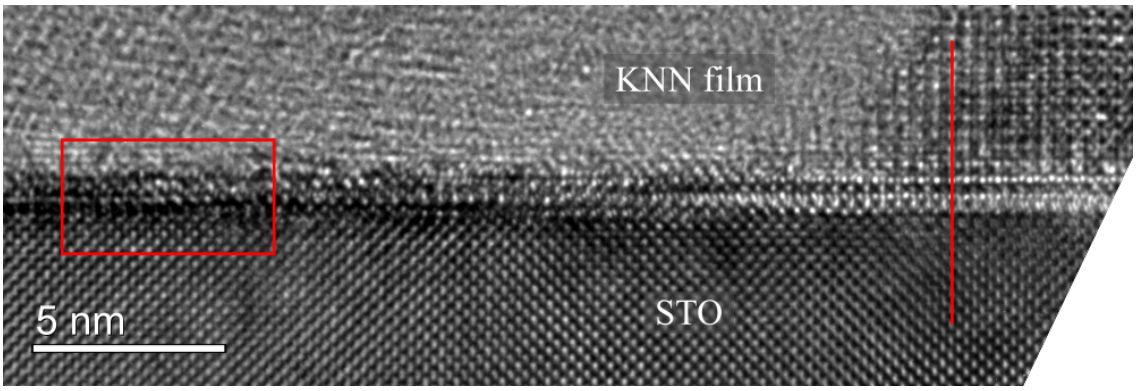

Figure 4.7: HRTEM image of the interface between STO substrate and KNN thin film, obtained from specimen *P450S*. The red line indicates the direction of observed fringes. The region indicated to the left shows patterns that were difficult to interpret.

Specimen *P550Sb* was only used for producing DF images to illustrate texture analysis in conventional TEM. Figure 4.8 shows three DF images constructed by selecting three reflections produced by SAD of the specimen. The information gained is limited to a small area and only describes regions with common orientations. Conventional TEM is in other words not efficient in obtaining information on the orientation of crystals over large areas. Hence, SPED was used to gain detailed information on the texture of the thin films.

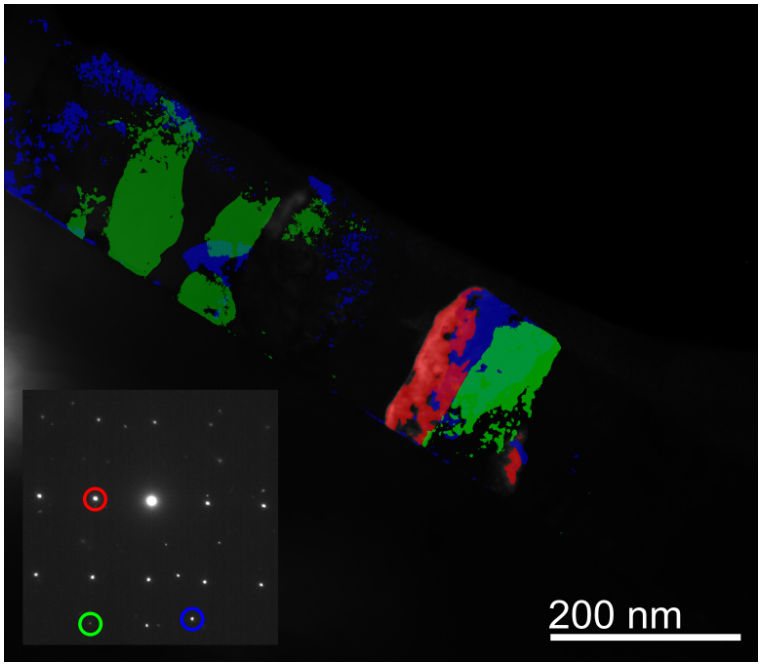

Figure 4.8: DF images produced in TEM from specimen *P550Sb*. The inset shows the DP with selected reflections.

4.2 Thin Film Texture

SPED datasets from specimen *P450S*, *P500N*, *P500S* and *P550Sa* were initially filtered and cropped to a region of interest, as explained in section 3.4.2. All datasets were then combined in order to create large orientation maps for each thin film sample. The complete orientation maps with crystal coordinates viewed along each specimen direction $(\mathbf{x}, \mathbf{y}, \mathbf{z})$ with subsets of orientations plotted into corresponding IPFs are presented in Figure 4.9, 4.10, 4.11 and 4.12.

The information gained from the orientation maps will be discussed in detail in section 5.1, however, some common observations for all specimens should be mentioned. All maps show how regions of similar orientations have been identified with even colouring stretching over larger areas. Some smaller regions containing scattered pixels with different orientations indicate small irregularities. By comparing the maps for each specimen coordinate, it is possible to distinguish some of the grains with the same columnar growth that was observed in the BF images presented in section 4.1. It should also be noted that seemingly systematic patterns observed in all $\mathbf{z}$ oriented IPFs are due to discrete angles used in template matching. The same amount of orientations are plotted, however, due to the geometry of the template they overlap in these IPFs. One of the most significant details in the maps is the lower regions marked in red for all specimen coordinates. These are of particular interest, as the red colour indicates that the $\langle 100 \rangle$ plane normals are stacked parallel to $\mathbf{x}$, $\mathbf{y}$ and $\mathbf{z}$, i.e. the same orientation as the substrate. As the regions are located in the lower region, it is implied that they originate from the substrate, i.e. they are epitaxial.

The texture of the specimens was visualised by plotting the crystal coordinate poles $\{001\}$, $\{011\}$ and $\{111\}$ in pole figures relative to the specimen coordinates. The figures for all specimens with corresponding ODFs are included in appendix B. The plots from all datasets, except for *P550Sa*, showed similar indications of symmetry. Thus, only pole figures of specimen *P500N* and *P550Sa* are included in this section, and are presented in Figure 4.13 and 4.14, respectively. Figure 4.14 shows some clustering around the centre of the $\{001\}$ pole. However, as there are some additional randomly positioned clusters, there is no sign of symmetry. Figure 4.13 shows some faint indications of the symmetry (also present in *P450S* and *P500S*) about a line approximately equal to the specimen direction $\mathbf{y}$ for all figures, indicating some form of preferred orientation being present. This is as expected when considering the epitaxial growth being oriented in the $\langle 001 \rangle$ direction. The small angle between the symmetry line and $\mathbf{y}$ comes from misalignment between the recorded PED patterns and the substrate, which ideally should be parallel as explained in section 3.3.2.

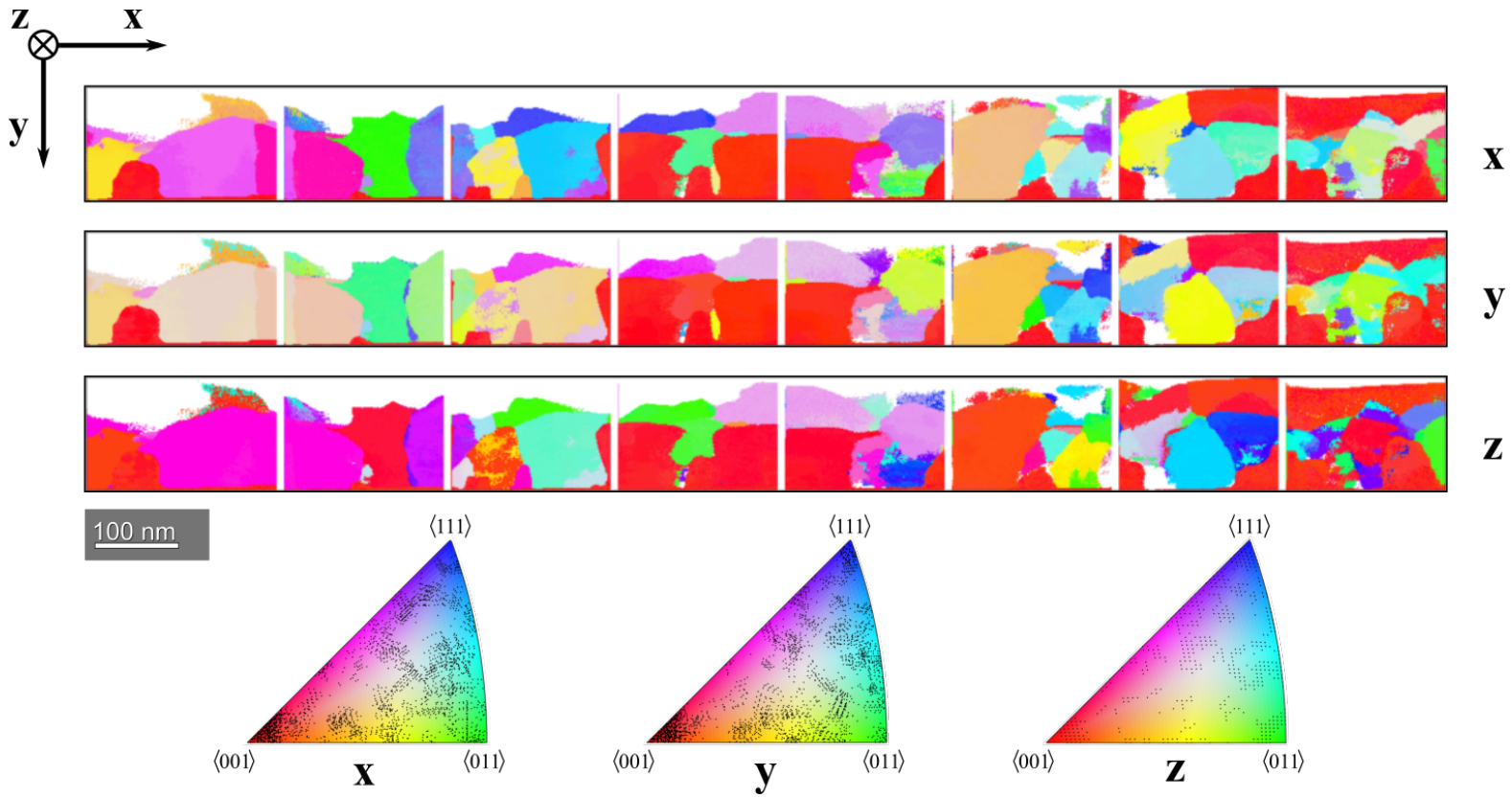

Figure 4.9: Filtered orientation maps with corresponding IPFs in the indicated specimen coordinates **x**, **y** and **z**. The maps are produced by eight datasets obtained from specimen *P450S*, with the substrate oriented down.

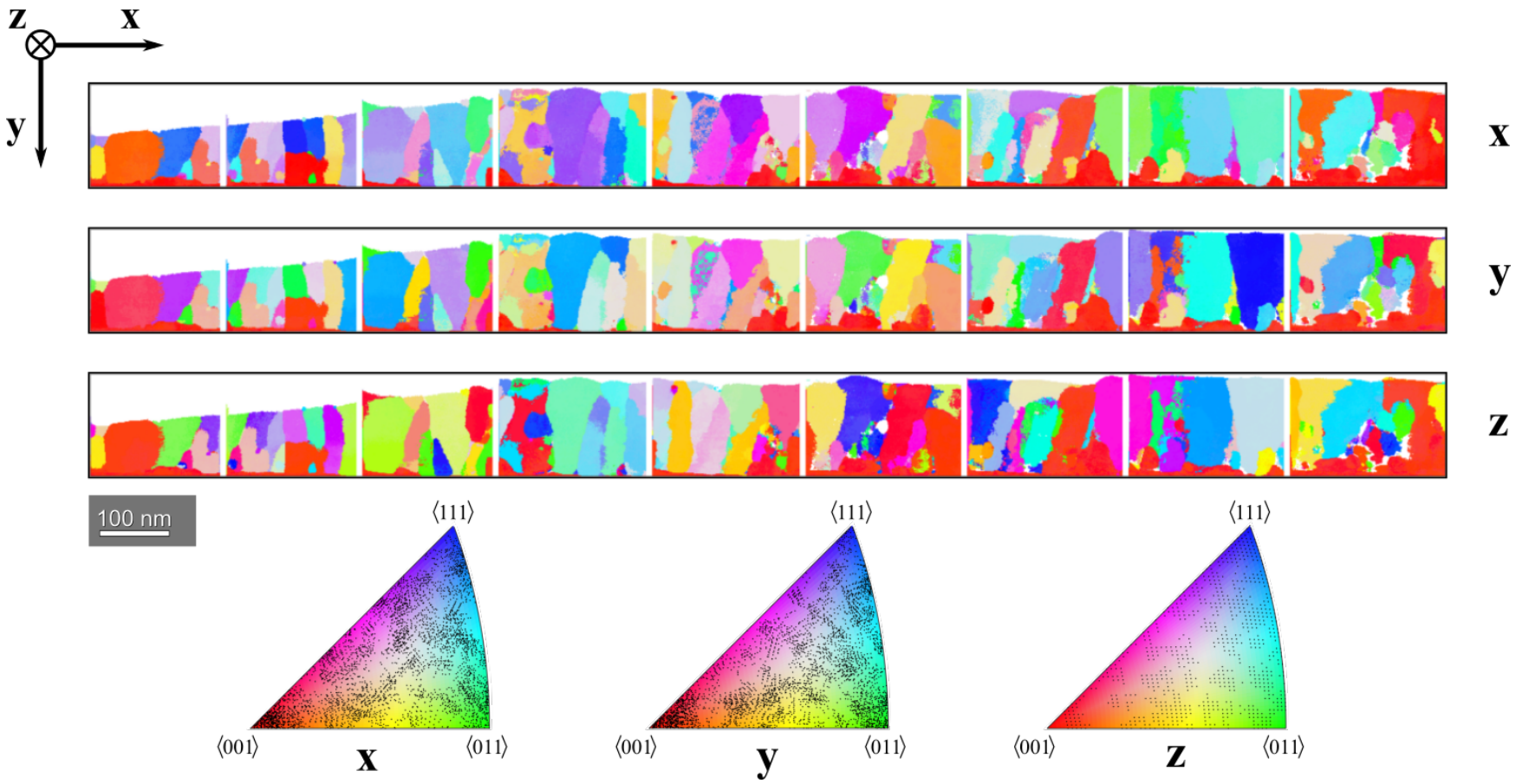

Figure 4.10: Filtered orientation maps with corresponding IPFs in the indicated specimen coordinates **x**, **y** and **z**. The maps are produced by nine datasets obtained from specimen *P500N*, with the substrate oriented down.

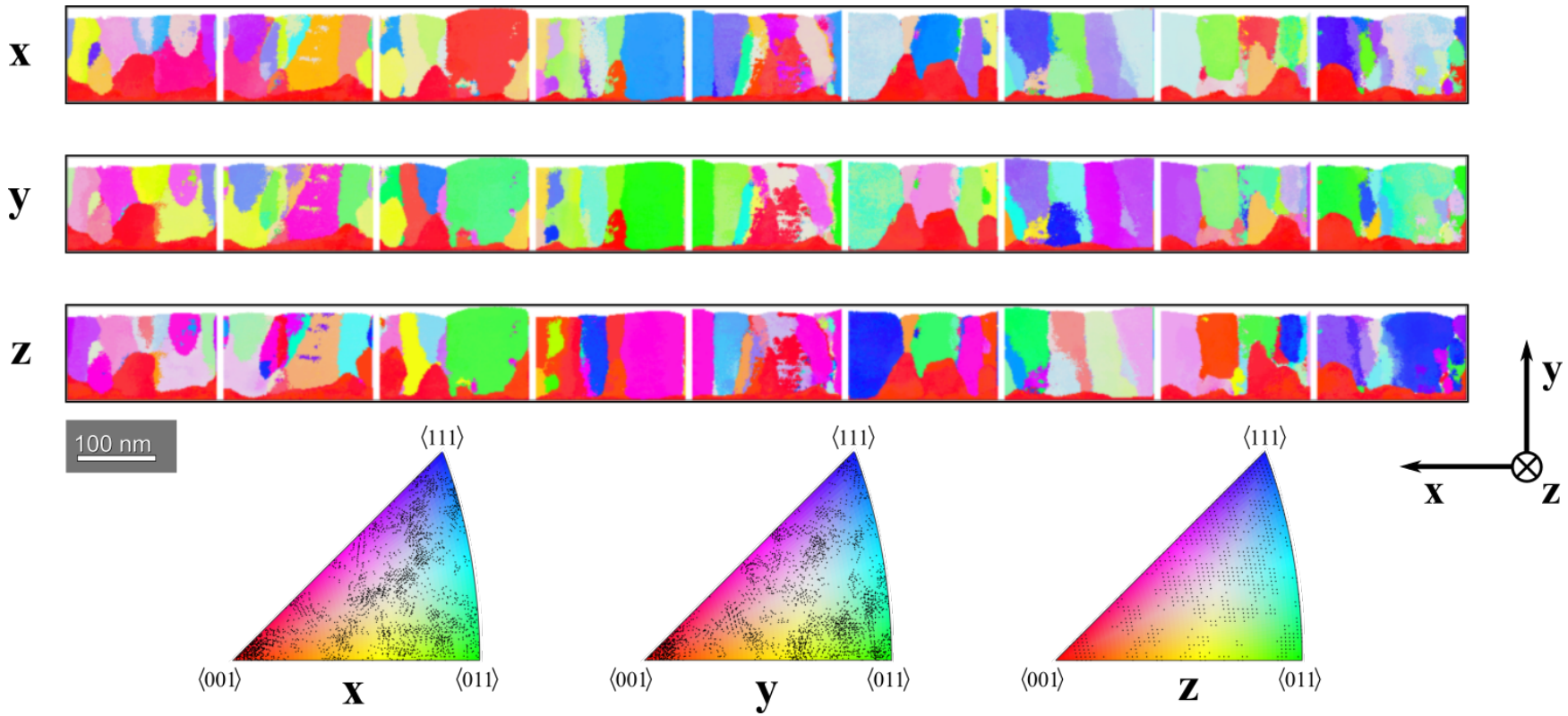

Figure 4.11: Filtered orientation maps with corresponding IPFs in the indicated specimen coordinates **x**, **y** and **z**. The maps are produced by nine datasets obtained from specimen *P500S*, with the substrate oriented down.

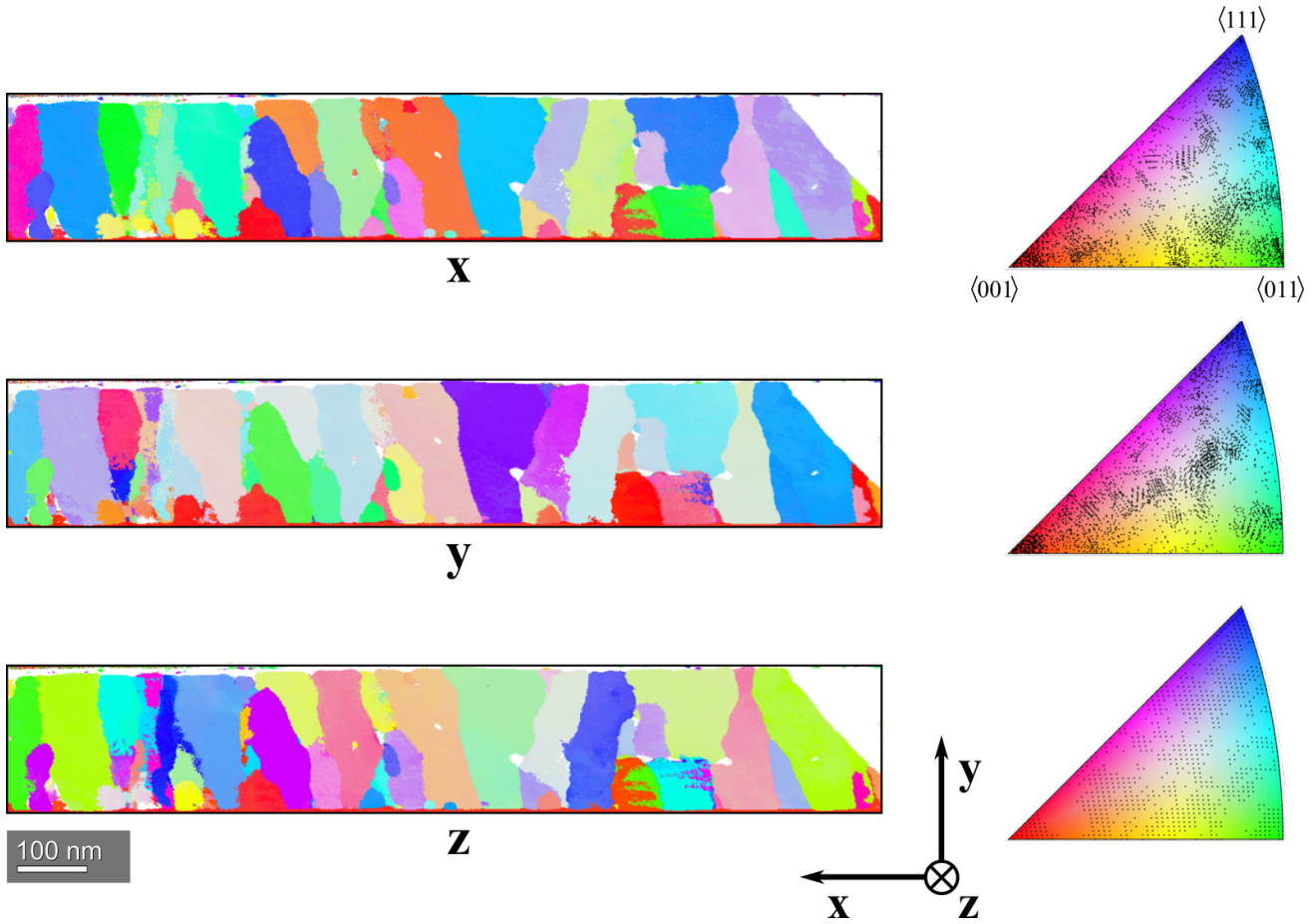

Figure 4.12: Filtered orientation maps with corresponding IPFs in the indicated specimen coordinates **x**, **y** and **z**. The maps are produced by datset obtained from specimen *P550Sa*, with the substrate oriented down.

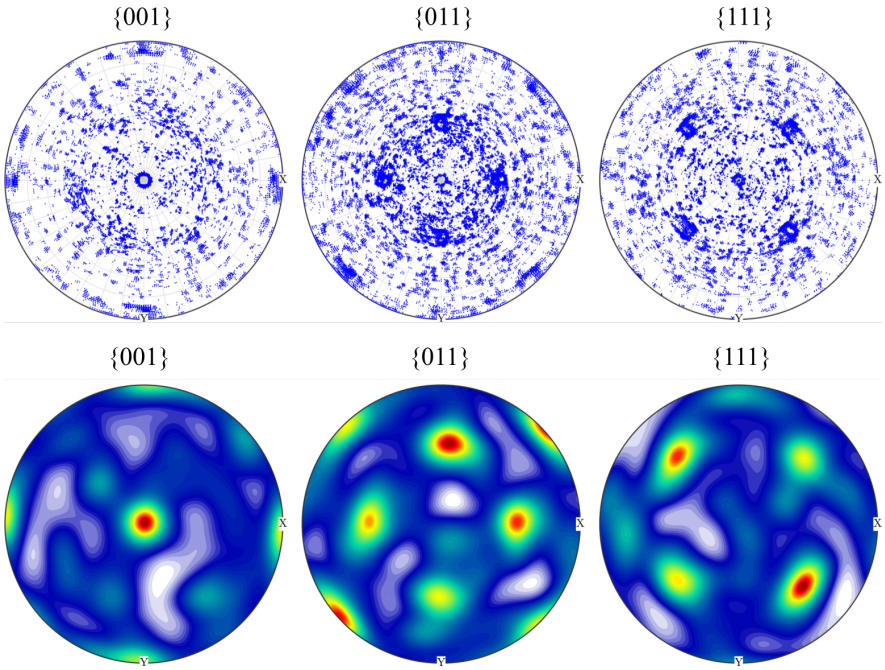

Figure 4.13: {001}, {011} and {111} pole figures of all recorded crystal coordinates relative to the specimen coordinates of specimen *P500N*. Calculated ODFs of these are included, with colours indicating probability density from low (light blue) to high (red).

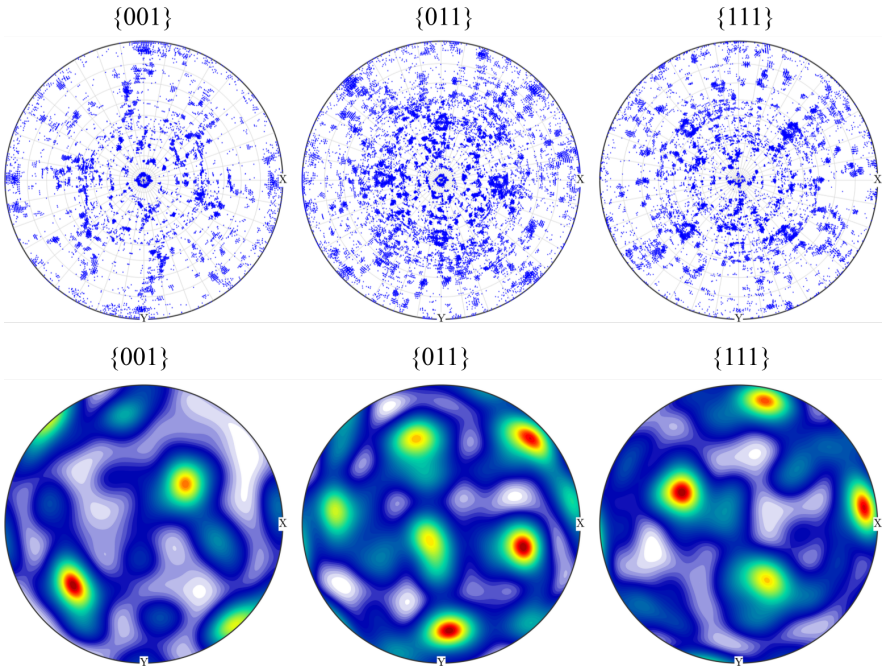

Figure 4.14: {001}, {011} and {111} pole figures of all recorded crystal coordinates relative to the specimen coordinates of specimen *P550Sa*. Calculated ODFs of these are included, with colours indicating probability density from low (light blue) to high (red).

The pole figures presented show a portion of the film being epitaxial, but any systematic trends in the remaining area can not bee seen. By calculating the misorientation of each recorded PED pattern relative to the orientation of the substrate, information from these regions was enabled. The results are presented in histograms plotted for each specimen in Figure 4.15. Due to the cubic symmetry of the template bank used, the greatest possible misorientation is 62.8° [30].

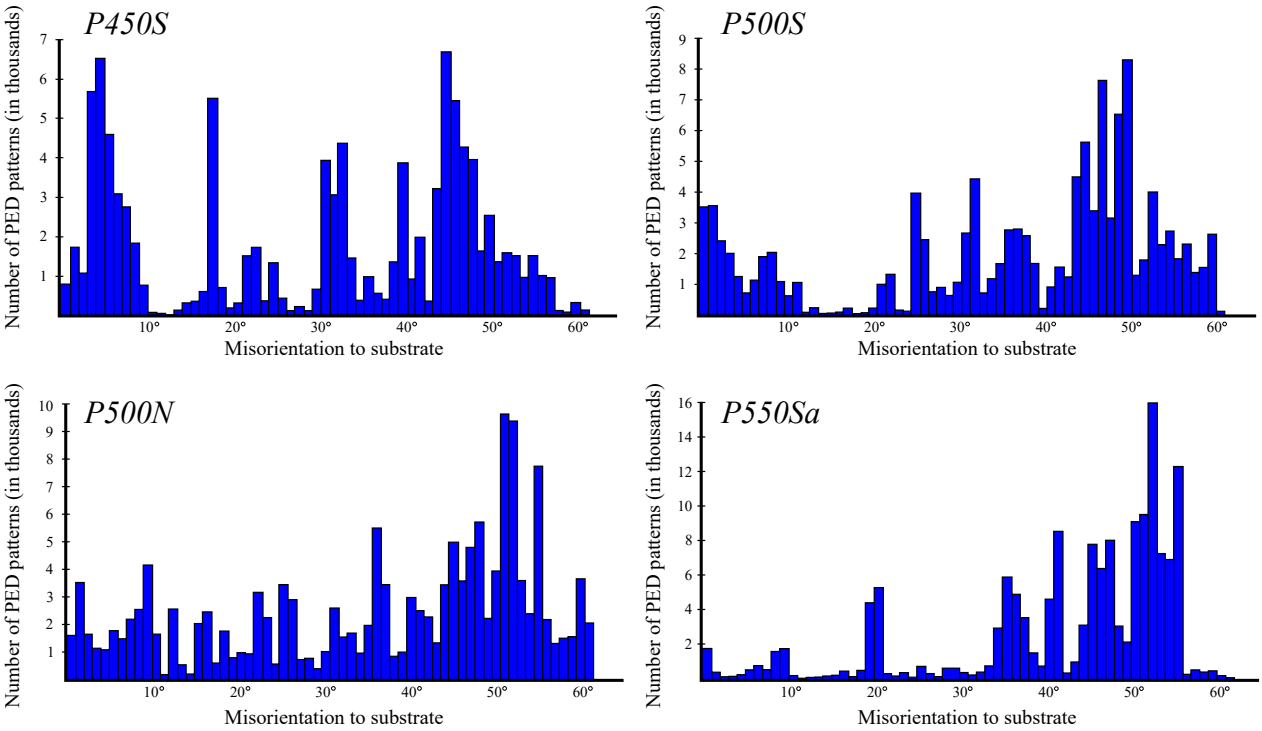

Figure 4.15: Misorientation of recorded PED patterns relative to the substrate in each specimen.

The data presented in Figure 4.15 illustrates the distribution of the misorientations for each specimen. The misorientations have also been plotted in a map, illustrated in Figure 4.16 (blue-yellow, low-high), were some large regions with the same misorientation may be observed. These regions were confirmed to be grains, shown by the defined grain boundaries included in the figure.

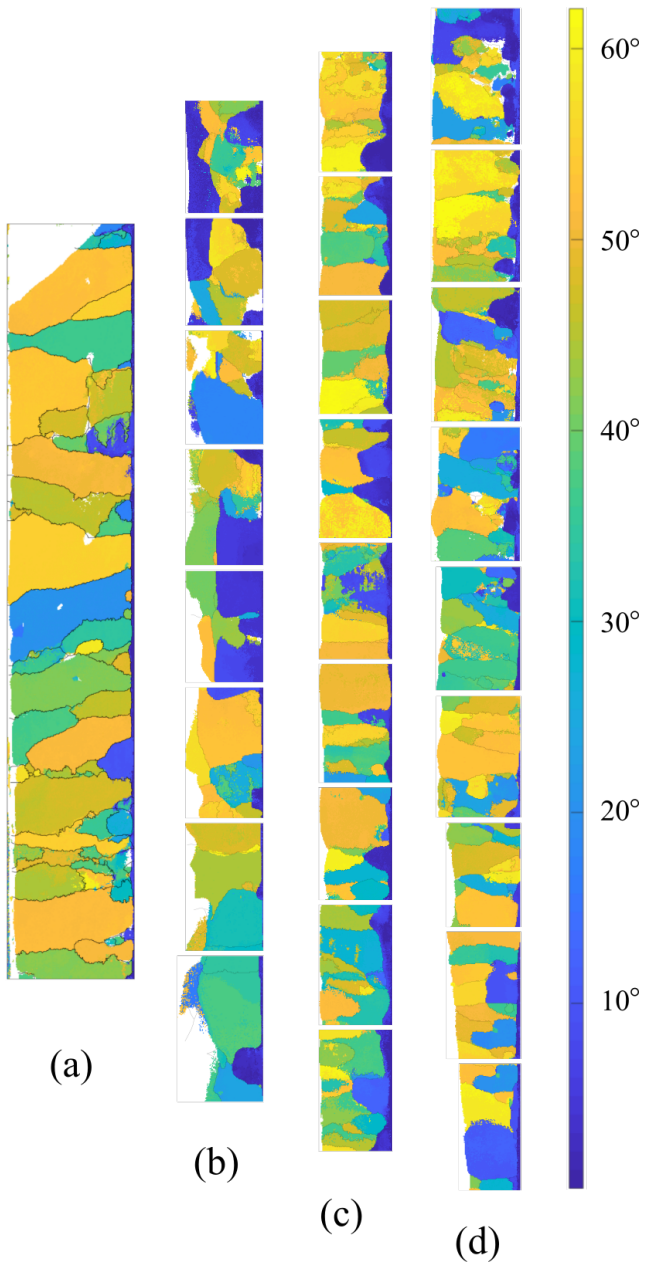

Figure 4.16: Maps of orientation relative to the mean orientation of substrate, produced by datasets from specimen *P550Sa* (a), *P450S* (b), *P500S* (c) and *P500N* (d). The defined grain boundaries are drawn. The substrate is oriented to the right for all maps.

Table 5: Information on reconstructed grains from each specimen. Size refers to the area of the projected grains.

Specimen	Number of grains	Mean size [nm^2]	Maximum size [nm^2]
P450S	93	921.6	7213
P500N	164	791.3	6149
P500S	131	792.9	5747
P550Sa	69	2031.6	12053

The grains were reconstructed as explained in section 2.4.3, with a threshold angle of 4° for all datasets. Table 5 shows the total number of grains as well as mean and maximum projected grain size of each specimen. The majority of the grain sizes are below 1000 nm^2. The size of the column grains ranged from 1300 nm^2 to 6000 nm^2 in all specimens except for *P550Sa*, where column grains as large as 12 000 nm^2 were observed. The definition of grain boundaries enables calculation of mean orientations of each grain. As with the PED patterns, the misorientation of each grain relative to the substrate was calculated for each specimen and the results are presented in Figure 4.17.

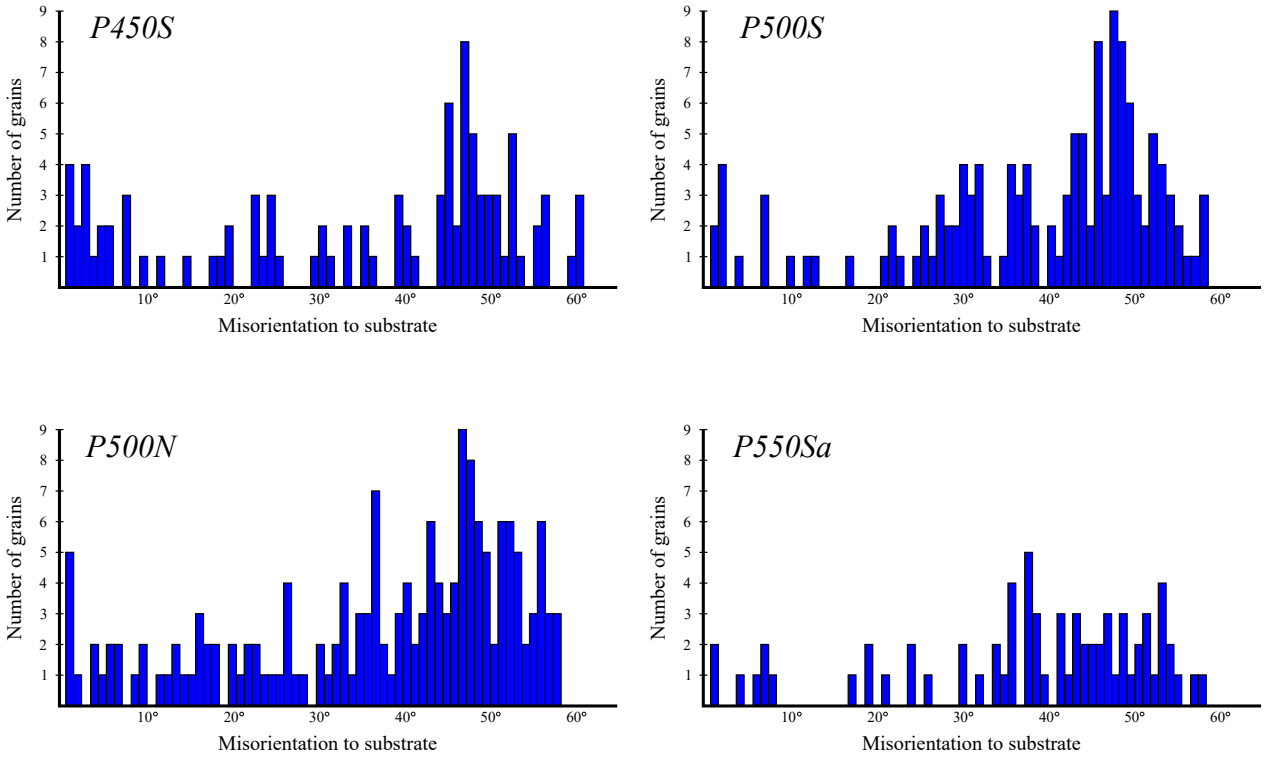

Figure 4.17: Misorientation of defined grains in each specimen relative to the substrate.

4.3 X-ray Diffraction

To complement the findings in TEM, Nikolai Helth Gaukås supplied X-ray diffraction data from specimen *P450N*, *P450S*, *P500N* and *P500S*, presented in Figure 4.18. The workings of XRD are beyond the scope of this study, it will not be discussed or presented in detail. However, some valuable information gained from the results will be explained.

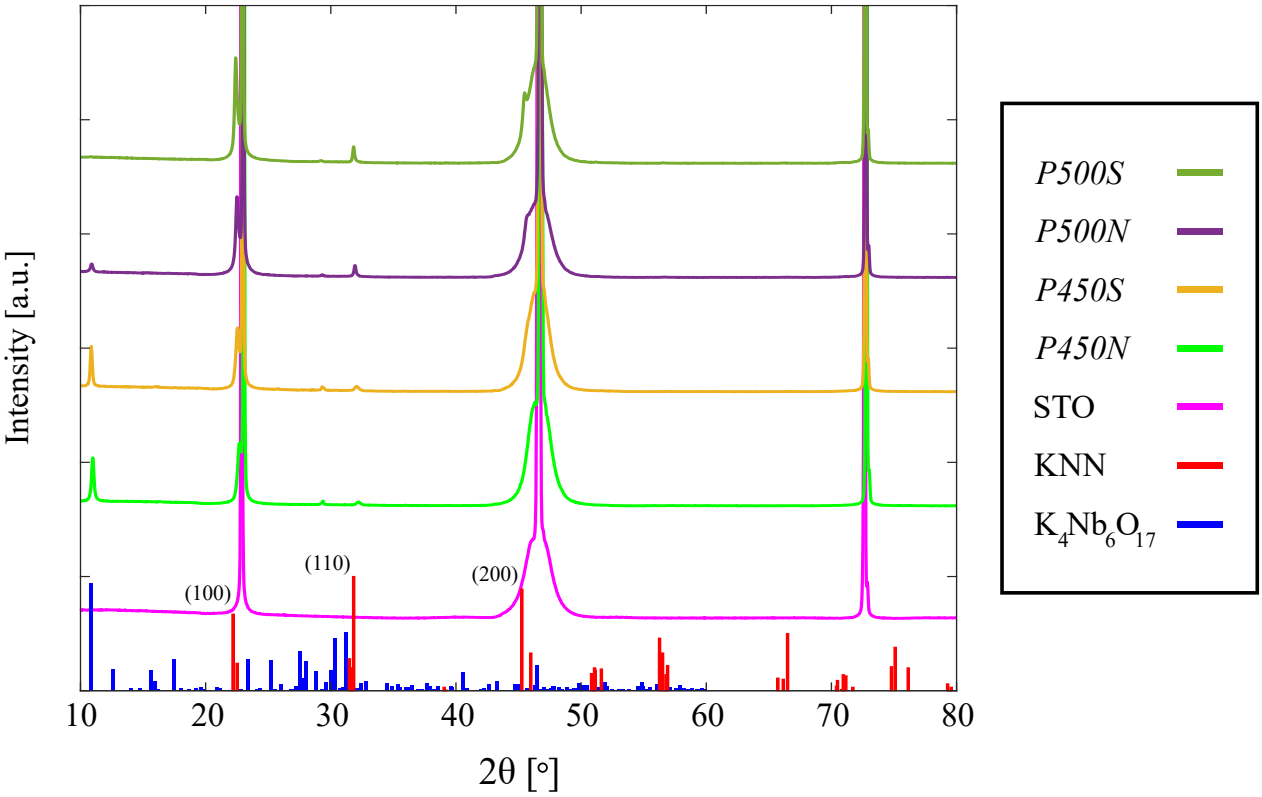

Figure 4.18: Regular X-ray diffraction ($\theta - 2\theta$ XRD) patterns of specimen *P450N*, *P450S*, *P500N* and *P500S* obtained by Nikolai Helth Gaukås [48]. The diffraction pattern from the STO substrate is included. Reference patterns for KNN and the secondary phase $K_4Nb_6O_{17}$ are included. The peaks indicating reflections (100), (110) and (200) for KNN are marked.

The reference patterns, shown as bars in the bottom of Figure 4.18, indicate the expected intensity ratios in the recorded diffraction patterns. As the KNN thin films were grown on (100) oriented STO substrates, all recorded XRD patterns contained intensities originating from STO in addition to the material of the film. Hence, the diffraction pattern from a clean STO substrate was obtained, enabling separation of substrate and material in the recorded results.

Figure 4.18 shows that the pseudo-cubic reflections (100), (110) and (200) are present in all the specimens. The (100) and (200) peaks, located close to the STO reflections, are notable higher than (110) and dominate the diffractogram for all specimens. This suggests that there are some texture present.

Finally, some information on the phase composition should be mentioned, as this may affect the microstructure of the films. Gaukås [48] describes observations of a secondary phase $K_4Nb_6O_{17}$ in some of the specimens. Indications of this phase can be observed in the diffractograms in Figure 4.18. The reference pattern for the phase shows a high peak close to $2\theta = 10°$. This peak is clearly visible in both specimens pyrolysed at 450 °C, indicating a presence of the secondary phase. Specimen *P500N* shows a much smaller peak, while no indications of the secondary phase is present for specimen *P500S*. It should be emphasised that phase purity of the films is not the focus of this study.

5 Discussion

The goal of this work was to study the microstructure and analyse the texture in chemical solution deposited, potassium sodium niobate thin films. The microstructure of the various specimens is first correlated to the synthesis of the thin films. Then, the size and growth of the observed epitaxial layers are described, before the overall texture of each specimen is discussed. Since the majority of the results in the study is based on the relatively new scanning precession electron diffraction technique in combination with automated crystal orientation mapping, aspects of data acquisition and processing are discussed. Lastly, the specimen preparation techniques used for the KNN thin films are compared.

5.1 Microstructure and Texture of the Thin Films

Before discussing the texture observed in the specimens, it is of interest to compare the observed microstructure in the films to previous findings by the research group at the Department of Material Sciences and Engineering of KNN thin films similar to the ones studied.

5.1.1 Effects of Sintering

The BF images in Figure 4.2 show how the specimens that were not sintered had delaminated from the substrate during preparation in the PIPS. The same preparation technique was used for sintered specimens, resulting in the thin film remaining intact. The delamination is therefore assumed to be a direct result of the specimens not being sintered. As mentioned in section 3.1, the sintering process increases the bonding between each deposited layer of KNN as well as the STO substrate. As both KNN and STO are perovskites with moderate difference in unit cell parameters (explained in section 2.2.1), it is expected that the thin film should bond well with the substrate due to epitaxy [49]. However, the results indicate that the temperature used for pyrolysis is not sufficiently high enough for creating chemical bonds between the two materials, thus sintering is necessary to properly attach the thin film to the substrate.

By comparing the results produced from specimen *P500N* and *P500S*, the effect the sintering has on the microstructure of the thin film may be studied. Several works describing this type of heat treatment of KNN have been reported in literature [50, 51]. However, as the effect of sintering is highly dependent on the composition of the precursor solution, as well as

the pyrolysis temperatures used, it is limited how other findings may relate to this study. Previous work concerning similar KNN thin films made by Dale [36] and Lorentzen [15] at The Department of Materials Science and Engineering describe the sintering (also named annealing) as a key factor in the crystallisation of the material. However, by comparing the BF images presented in Figure 4.4 and 4.5, it is obvious that the film already crystallises during pyrolysis at 500 °C, with distinct columnar grains being observed in specimen *P500N*. Further inspections of the specimens show close similarities in the microstructure before and after sintering. The orientation maps presented in Figure 4.10 and 4.11 show no distinct differences and the mean size of the reconstructed grains are 791.3 nm^2 and 792.9 nm^2 for *P500N* and *P500S*, respectively. It has been found by Lorentzen that KNN films pyrolysed at 400°C are amorphous, implying no crystallisation prior to sintering [15], thus making sintering the dominating factor for grain growth as it crystallises the film. In the same study it was proved that at least partial crystallisation occurred at pyrolysis temperature above 500 °C. It should be noted that this was with another precursor solution.

Despite close to no changes in the observable microstructure, the XRD data presented in Figure 4.18 shows that the sintering removes most of the secondary phase in the specimen pyrolysed at 500 °C. It should be noted that the secondary phase is barely present for this specimen, and that the sintering is unsuccessful in removing it for the specimen with a pyrolysis temperature of 450 °C.

5.1.2 Grain Morphology and Thin Film Thickness

The KNN films analysed in this study are all polycrystalline with clear columnar grain structures. The column boundaries are oriented at different angles relative to the substrate surface, with some grains becoming slightly larger further away from the substrate. The grain columns extend from the bottom to the top of the film for all specimens, except for *P450S* where the columns are restricted to the lower two thirds of the film thickness. The reason for this distinct change in microstructure is uncertain. The crystallisation of CSD deposited films depends to a large extent on the growth temperature and whether crystallisation takes place during growth or as a post-growth process [52]. The information gained from the XRD data in Figure 4.18 implies that the unsintered specimen pyrolysed at 450 °C is crystalline. However, as no information was gained from this specimen in the TEM, it is uncertain if complete crystallisation occured during pyrolysis at this temperature. The structure of the grains in *P450S* may thus be a result of either crystallisation during growth, post-growth, or a combination of the two. From the results discussed in 5.1.1, it is assumed that the

crystallisation for the remaining specimens occurred during pyrolysis, i.e. during growth. Consequently, the morphology of these films has taken on a columnar characteristic in which the crystal structure of the initial layer is templated through the entire film thickness, with only some minor changes [53].

One important factor to the microstructure of specimen *P450S*, is the presence of the secondary phase $K_4Nb_6O_{17}$. Previous work on development of KNN thin films using similar synthesis done by Pham [54] shares the same observations of another niobium rich secondary phase ($K_2Nb_4O_{11}$), suggesting it to have an elongated grain structure located at the end surface of the film. The films produced by Pham were treated with a pyrolysis at 400 °C and sintering at 800 °C, both being relatively close to the temperatures used on specimen *P450S*. This implies that the columnar grains may be restricted to the lower part of the film due to formation of grains of the secondary phase occurring in the surface region. This would explain why the remaining specimens with higher pyrolysis temperatures all have columns extending throughout the thickness of the films, as they have no or minimal presence of the secondary phase. It should also be mentioned that the results presented in Figure 4.18 clearly shows that an increase in pyrolysis temperature reduces the presence of the secondary phase, and is consistent with what is given in literature [15, 36]. As the analysis of phase purity exceeded the scope of this study, observations of the secondary phase have not been a priority and has not been detected in TEM.

The reconstruction of grains from the orientation data given in the SPED datasets show multiple smaller grains in addition to the ones with columnar structure. The initial definition of the grain boundaries showed signs of small grains existing within the columns. These were however removed, as they either were too small or had an orientation close to equal to the mean orientation of the column. The filtering of grains will be discussed further in section 5.2.2, but it should be noted that the information gained on grains from the SPED datasets should be interpreted with care. Table 5 shows that the size of the reconstructed grains vary among the specimens, except for *P500N* and *P500S*, as previously mentioned. As the columnar grains extend through the film, their sizes are affected by the thin film thickness. This makes the comparison of grain size between specimens irrelevant. The localisation of the grains within each specimen is still of interest. The boundaries of the reconstructed grains shown in Figure 4.16 indicate a small majority of the smaller grains being located in the lower half of the film. The surface of the specimens pyrolysed at temperatures above 450 °C are mainly dominated by the columnar grains, however, some small grains are also located in this region. This shows that there are some changes to the initial layer, suggesting that there may be some minor competitive growth of grains along the film thickness. As

the column grains become thicker further away from the substrate, it is expected that these will dominate in the surface region. This will also affect the size of the grains measured at the surface, essentially resulting in larger grains measured for thicker thin films. Still, the measured thickness of the grains at the surface (corresponding to diameter measured in plane-view) correlates well with what is given in literature [36, 54] for all specimens, ranging from a few nm up to more than 100 nm. It should also be mentioned that the thickness of the columnar grains at the surface in specimen *P500S* was in accordance with measured diameters in the plane-view SEM image shown in Figure 4.1, ranging from 35 to 110 nm.

The variation in thin film thickness for each specimen, presented in Table 4, is most likely due to the deposition technique used. As described in section 3.1 the spin coating relies on the centrifugal force which not necessarily spreads the solution evenly, resulting in thinner areas at the edge of the substrate. The levelness was also dependent on where the initial solution drops were deposited. The specimens produced in PIPS were made out of the cross-section presented in Figure 3.2, which essentially resulted in one cross-section side being further away from the centre than the other. This can explain the film thickness variation in *II* and *III*.

5.1.3 Epitaxy

Epitaxial growth is most commonly obtained through physical deposition methods, e.g. pulsed laser or RF magnetron sputtering [37, 38]. Still, the aqueous CSD method used for synthesising the films analysed in this study proved to contain some degree of epitaxial growth. Figure 4.7 illustrates the thin epitaxial layer stretching along the substrate surface for all specimens. Some larger epitaxial grains observed in HRTEM are also present in the orientation maps shown in section 4.2. The size and number of such grains vary in the different specimens, implying a dependency with pyrolysis temperature. Similar films as the ones studied, also prepared by sol-gel deposition, have also been showing signs of epitaxial layers [54, 55]. Yu et al. [55] observed a higher probability of epitaxy when the pyrolysis temperature was in the range 400-450 °C, thus proposing that the development of the epitaxial layer was dependent on the pyrolysis temperature. This is in accordance with the results obtained in this work, as the specimens with lower pyrolysis temperature show more signs of epitaxy.

Figure 4.15 gives information on how much of the material that is epitaxial for each specimen. As some variation in the orientation of the substrate itself was recognised, some degree of misorientation can still be considered epitaxial. The plots clearly show a decrease in epitaxy for higher pyrolysis temperatures. This can be explained by the nucleation and growth process which is highly dependent on pyrolysis temperature [39, 52, 56]. Schwartz et al. [39]

describe how a low pyrolysis temperature will induce heterogeneous nucleation to occur at the surface of the substrates, resulting in epitaxial growth. This is explained by a lower activation energy for heterogeneous compared to homogeneous nucleation in general. The same change from epitaxial to polycrystalline microstructure has been documented by Pham [54], though without columnar grain growth.

As the specimens analysed were built layer by layer with columnar growth being observed, it is assumed that each subsequent layer nucleated heterogeneously on the grains crystallised during the previous deposition. This implies that if the initial layer nucleated epitaxially at the substrate, the epitaxy should extend throughout the film thickness. This has, however, not been observed in any of the specimens analysed in this study. The existence of smaller grains originating close to the surface of the thin films suggests that there is some sort for competitive growth. Under certain processing and heat treatment conditions, nucleation may also occur within the bulk of the film [56], i.e. homogeneous nucleation, which results in random oriented grains. Thus, it is natural to assume that there is a competition between heterogeneous and homogeneous nucleation in the specimens, especially in the initial deposited layer. This would explain why the epitaxial layer observed in the first deposited layer is mainly thin (1 - 3 nm), as only a fraction of this layer nucleates heterogeneously, while the majority nucleates homogeneously. Some of the heterogeneous nucleation may extend all the way through the thickness of this layer. The next layers deposited consist mainly of heterogeneous nucleation that forms columnar grains taking on the crystal structure from the surface of the initial layer. This would result in columnar growth with mostly random oriented grains and only a few epitaxial ones, like the ones observed in the study.

It is uncertain why the initial layer has a minority of heterogeneous nucleation opposed to the subsequent ones. One explanation may be that a higher activation energy is needed for nucleation on STO compared to nucleation on the same type of material. The inherent strain from the lattice mismatch between STO and KNN might build up a high lattice energy. This is not favourable to sustain for the system, resulting in an epitaxial layer of only a few nanometres and random nucleation on top of this region. Thus, the energy gain from heterogeneous nucleation is cancelled by the energy required to maintain strain in the material. To force the growth of a completely epitaxial film, it might be necessary to go further down in pyrolysis temperature to promote heterogeneous nucleation and suppress lattice relaxation through random oriented nucleation.

5.1.4 Texture

As explained in section 2.2.2, the piezoelectric properties of the thin films are dependent on how well the crystals/grains are aligned. One of the main goals of this study was to analyse the thin films and determine if the grains had some preferred orientation, i.e. texture. The microstructure has already been described with columnar grains and some small regions of epitaxial growth extending from the substrate. However, none of the results show any clear signs of the thin films being highly textured. This is visualised in the orientation maps and correlating IPFs presented in section 4.2, where the grains have been matched with seemingly random orientations relative to each other. The larger grains produce clusters in the IPFs, none oriented in the same direction. Due to the epitaxy, some denser clustering is observed in the orientation near $\langle 001 \rangle$, especially for specimen *P450S*, suggesting that it may be described as having a weak [001] texture.

The epitaxial growth also affects the calculated ODFs given in appendix B, where a presence of the [001] texture is observed for all specimens except *P550Sa*. The results obtained from these figures are somewhat ambiguous, as the pole figures show the majority of the crystal coordinate poles being randomly scattered. The lack of texture in the ODF of *P550Sa* may be a result of the specimen being relatively thicker than the other, thus limiting the effect of the epitaxial growth in the film. It can also be explained by the much smaller amount of epitaxy compared to the other specimens.

As the amount of epitaxy was limited in most of the specimens, the remaining grains may affect the texture of the films to greater extent. The misorientation distributions presented in Figure 4.17 show the orientations of grains in each specimen relative to the substrate. Except for some small anomalies, all plots seem to follow the Mackenzie distribution [57] which describes the theoretical distribution of perfectly random polycrystals. The small deviations are considered negligible, as the epitaxial grains still dominate. This is in accordance with what is given in literature [9, 39, 55], where highly textured films have been synthesised as a direct result of epitaxial growth.

As mentioned in section 4.3, the XRD results show clearer indications of the same form for texture being present in all films. As the results produced in TEM have been obtained from limited regions ($\sim 0.3\,\mu m^2$), it is possible that the epitaxial layers are more prominent in other parts of the thin films. This would explain the indications of a higher texture observed for XRD and confirm a weak texture in the analysed specimens, but further research is needed to confirm this theory.

5.2 Data Processing

5.2.1 Quality of Template Matching

Before analysing the collected SPED data, template matching was performed. As mentioned in section 3.4.1 three different template banks were made, based on the pseudo-cubic, orthorhombic and monoclinic structures of KNN given in appendix C. The quality of the template matches from these banks were compared by applying them to one of the cropped SPED datasets produced by specimen *P500S*. Mean values were calculated for the correlation index Q and reliability R and are presented in Table 6. Only the pseudo-cubic template bank produced reliable matches with high R. Orientation maps produced form the other banks showed seemingly random scattered orientations, thus only the pseudo-cubic bank was used in this study.

Table 6: Mean value of correlation index Q and reliability R calculated for the various template banks.

Template bank	Pseudo-cubic	Orthorhombic	Monoclinic
Average Q	29.5551	27.5083	29.3837
Average R	18.0453	2.7218	1.3629

As explained in section 2.4.2, each pixel in real space contain information on the correlation index Q and reliability R. Maps of these values for each specimen have been included in appendix D, in order to visualise the localised quality of the scanned regions. The mean values of Q and R of each specimen are presented in Table 7, and are of acceptable quality [35]. The maps correlated relatively well, with values gradually changing without drastic change in most regions. However, a few areas with relative high Q contained seemingly randomly scattered pixels of high and low R values. One example of this anomaly is shown Figure 5.1, where the region to left of the maps contain high and low R values. Two PED patterns from this region are included in Figure 5.1, one with high R (c), and one with low R (d). The IPFs in the figure show density maps of how well the simulated patterns match the experimental ones. As the two PED patterns and IPFs are close to identical, this sudden change in reliability is unexpected. A possible explanation may be that the weaker reflections have not been recognised by the Index software for the PED patterns assigned with high R. This implies that these reflections are at the threshold range. Due to this uncertainty, some regions in the datasets may contain wrongly indexed PED patterns.

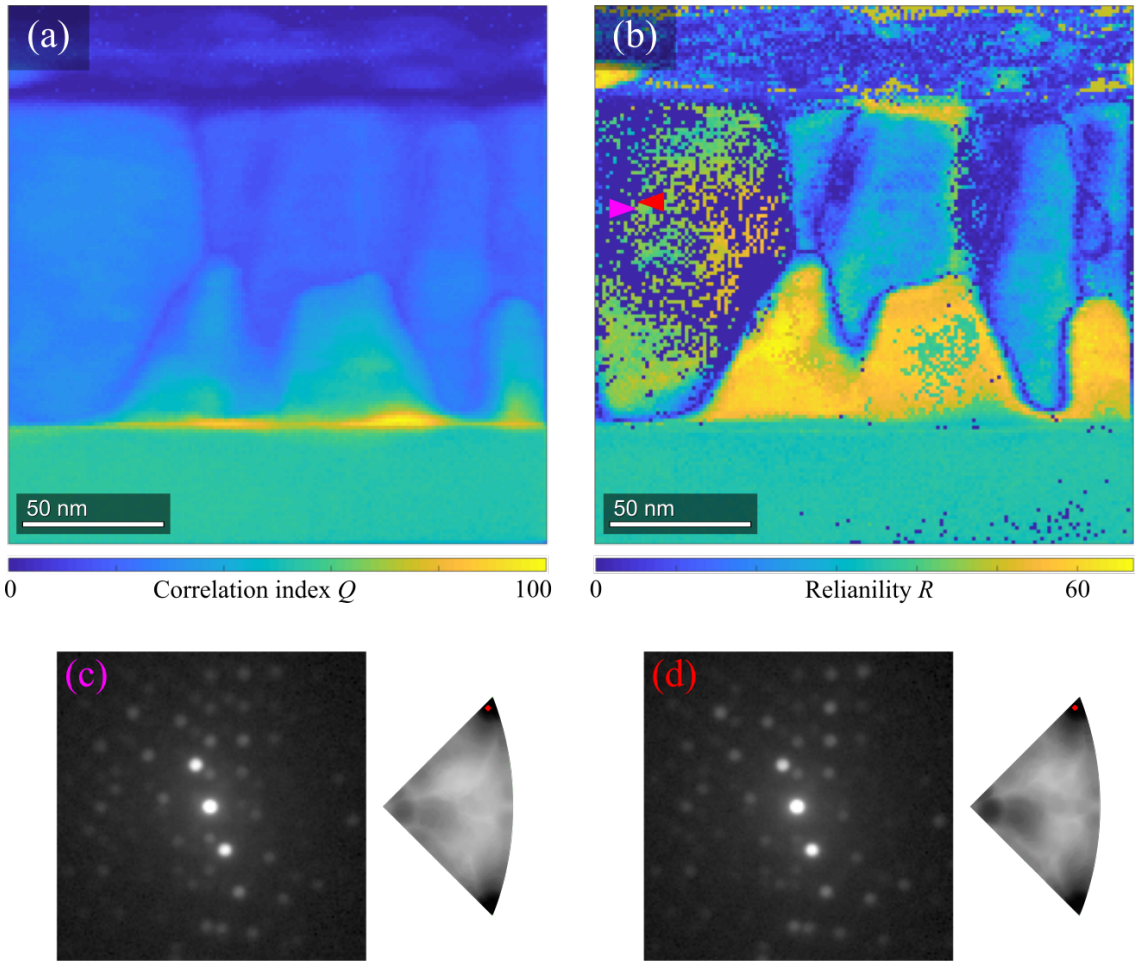

Figure 5.1: Quality of template matching in maps of correlation index Q (a) and reliability R (b) produced by a dataset from specimen *P500S*. PED pattern with high R (c), and with low R (d) are obtained from the pixels marked with respective colours in (b). The match between the simulated and the experimental patterns are plotted as a density maps in the IPFs, with dark regions indicating good match.

Table 7: Mean value of correlation index Q and reliability R calculated from all the cropped and filtered datasets produced by each specimen using the pseudo-cubic template.

Specimen	*P450S*	*P500N*	*P500S*	*P550S*
Average Q	34.4566	31.4224	28.8822	29.0567
Average R	25.6580	24.5162	22.3596	30.4806

5.2.2 Definition of Grain Boundaries

The grain boundaries were defined as explained in section 2.4.3 with a threshold angle of 4°. The initial boundaries produced multiple small grains which were scattered randomly in the datasets. The majority of these grains consisted of only a few PED patterns, indicating that they were a result of wrong template matching. The datasets were therefore filtered, removing all grains smaller than 20 nm^2, before defining new boundaries with the same threshold angle. As mentioned, former research recommends a further removal of unreliable grains, based on the reliability of the PED patterns within each grain [35]. Attempts were made, however, it was concluded that this lead to the removal of too large regions. As explained in section 5.2.1, there were some errors in R, supporting the decision not to filter based on these values.

The reconstructed grains still needed processing, as observations of neighbouring grains with similar orientations were made. A closer inspection showed that the PED patterns at the boundary had a relative high misorientation with respect to the mean orientation of each grain. The mean orientation was, however, close to equal for the two, making the boundary ambiguous. Proper reconstruction of grains and grain boundaries is a common issue, and various approaches for better results are described in literature [58, 59]. Humphreys et al. [58] proposes a solution to the problem, by applying a filter before the initial definition of boundaries. Multiple filters were therefore tested on the recorded data, none of which produced satisfactory results. Hence, selected grains were merged manually by comparing mean orientations. It should be noted that some of the filters in MTEX are complex, and further research on the applications of these might have yielded more reliable results.

There is a source of error present in the measured size of the reconstructed grains. This is due to some of the grains being located at the image boundary, suggesting that the areas may be underestimated. It is therefore recommended to use rectangular scans, as this limits the number of grains being affected by this. It is also possible to remove these grains, however this would have led to insufficient amount of data for this study.

5.2.3 Quality of SPED Data

The quality of the orientation maps is highly dependent on the data acquired in TEM. One of the major challenges for TEM in general is the possibility of the electron beam penetrating different grains or materials through the thickness of the TEM sample. This leads to complications for the SPED technique in particular, as only one orientation is assigned to a PED pattern that can show reflections from multiple grains. This problem most certainly

affects the results obtained in this study, as there is a probability of overlapping grains. This probability is considered relatively high, as a specimen of 100 nm thickness can contain at least three grains of 30 nm diameter, and smaller grains have been observed in the films. The PED patterns presented in Figure 5.1 (c,d) are clear examples of the overlap problem. The irregularities observed in the orientations maps can also be explained as a direct result of overlapping grains. The scattered pixels of different orientations are located in regions where multiple reflections in PED patterns produce different results in template matching.

Another factor that affects the PED patterns is the presence of afterglow. This phenomenon is a result of the reflections recorded from one probe position being carried over to the next, due to reflections not disappearing fast enough in the fluorescent screen. The problem of afterglow may be averted if the acquisition exposure time was increased, giving reflections for the present probe position time to dominate the fluorescent screen. However, this would also result in fainter reflections not being recognised.

To control how well the orientation maps described reality, a high-resolution image was obtained from a selected pair of grains observed in specimen *P550Sa*. FFTs of the substrate, the two grains and the interface between the substrate and each grain were created from this HRTEM image. Figure 5.2 shows a BF image of the grains with orientation maps plotted along specimen coordinates $\mathbf{x}$ and $\mathbf{y}$, as well the HRTEM image with corresponding FFTs. The orientation maps indicate that the grain the to left approximately shares orientation with the substrate in both the $\mathbf{x}$ and $\mathbf{y}$. However, the grain is a slight shade brighter in the $\mathbf{x}$ direction, indicating a small rotation about the $\mathbf{y}$ axis. This small rotation can be observed in the produced FFTs as well. The blue FFT shows how the pattern of the grain perfectly overlaps the substrate which is at zone. The pink FFT shows the pattern produced by the grain alone, which is close to being at zone, but with a slight rotation along the $\mathbf{y}$ axis. The grain to the right has a seemingly random orientation relative to the substrate, which is confirmed by the FFTs as well.

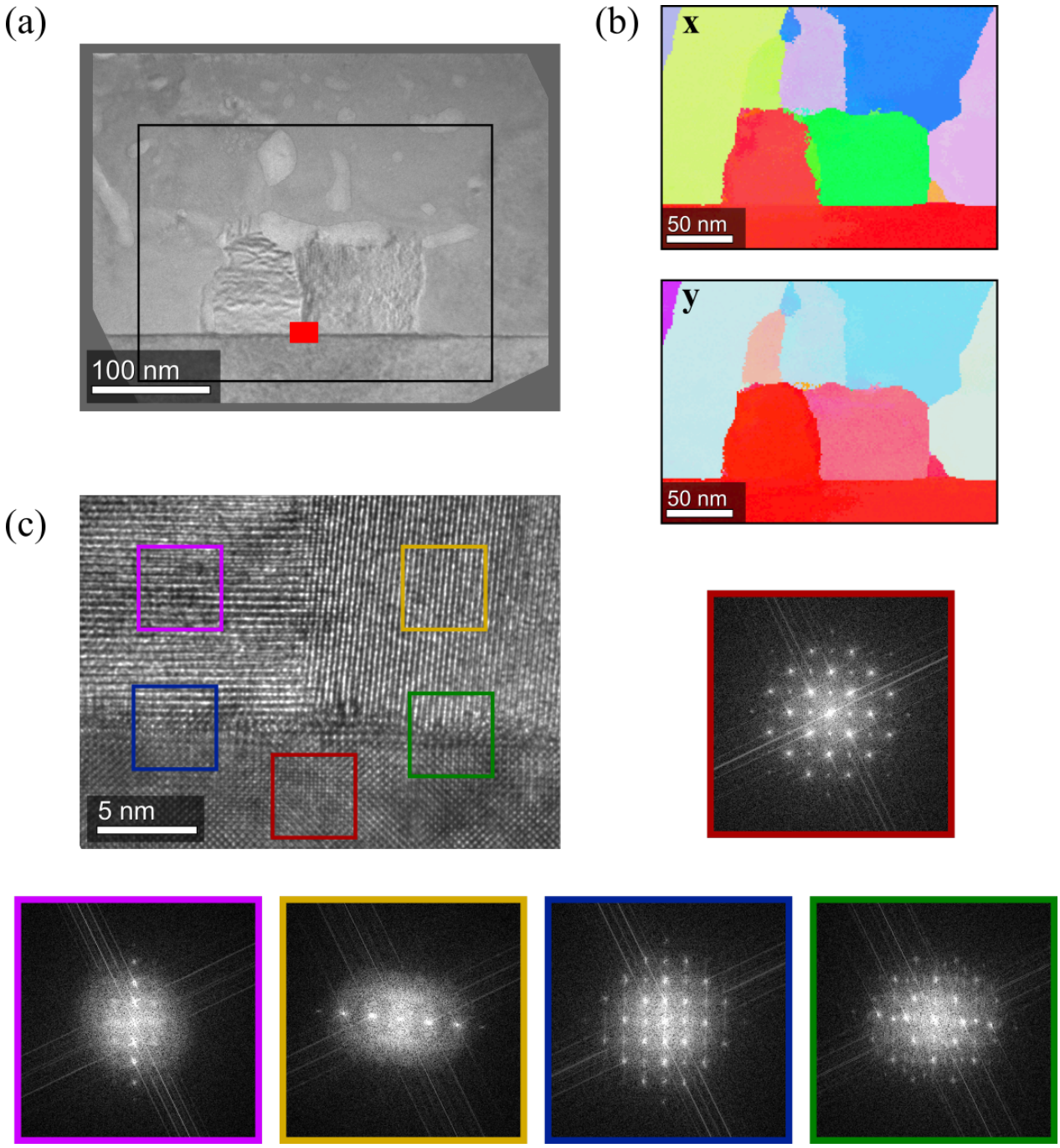

Figure 5.2: The black rectangle in the BF image (a), indicate the region presented in the orientation maps (b). The red rectangle in (a) marks the region where the HRTEM image (c) was obtained. FFTs presented in coloured frames originate from the undersized squares in the HRTEM image. The images were obtained from specimen *P550Sa*.

5.3 Sample Preparation

Two different preparation techniques were used in this study, both producing specimens of high quality. The samples made using FIB were easy to work with in the TEM, due to high degree of control over the zone axis. Both specimens contained large areas of electron transparent material with minimal height difference. However, it is important to mention that FIB preparation is an expensive technique that requires much skill and expertise to perform. The samples produced by PIPS proved to be of comparable quality to the ones made by FIB, containing even larger areas of electron transparent material. However, as the technique is based on a dimple, the specimen becomes increasingly thicker further away from the hole. This leads to a decrease in quality, as it becomes less electron transparent and the possibility of multiple grains overlapping increase in these regions. Another disadvantage of the PIPS specimens is the glue layer. As mentioned in section 4.1, the thin film delaminated from the substrate in some samples due to weaker bonding. The delamination most likely occurred during ion polishing in the PIPS, as the specimens were being exposed to drastic temperature changes. This would result in different thermal expansion and contraction of the materials in the specimens. A thinner glue layer could have restricted this movement and delamination might been avoided.

Both techniques expose the specimens to an ion beam, which is a potential danger as it can turn the crystalline material amorphous. For the FIB specimens, the protective layers of Pt/Pd (80/20) and deposited carbon proved to be sufficient to stop the gallium ions from reaching the film. Ion beam damage of the PIPS specimens was avoided by gradually reducing the acceleration voltage.

It is worth to mention that preparation by wedge polishing has been tried by the author [11]. This technique proved to not be as efficient, as no usable specimens were obtained due to the material cracking.

6 Conclusion

The column growth morphology, epitaxy, thin film texture and grain size of chemical solution deposited KNN thin films were studied in TEM. The effects of pyrolysis have been investigated, based on the results from studies of specimens pyrolysed at 450 °C, 500 °C and 550 °C. The effects of sintering at 700 °C are also investigated, based on comparisons between an unsintered and a sintered specimen pyrolysed at 500 °C. The thickness of the thin films ranged from 150 nm to 240 nm. Conclusions from the thin film studies in TEM are:

- Sintering at 700 °C proved necessary for good bonding between substrate and thin film.
- Crystallisation during pyrolysis at 500 °C was found to be in direct correlation with the final crystallographic structure of the films after sintering.
- The microstructure of the films is dominated by a columnar growth in which the crystal structure of the initial layer has been approximately templated through the entire film thickness.
- Thin films pyrolysed at 450 °C show column grains only extending through two thirds of the film thickness. The majority of the column grains in films pyrolysed at higher temperatures extend all the way to the film surface.
- The columnar grains become larger further away from the substrate.
- The size of the projected column grains ranged mainly from 1300 nm^2 to 6000 nm^2, with grain thickness at the surface ranging from a few nanometres to over 100 nm.
- All films contained thin epitaxial layers (1 - 3 nm) covering most of the substrate surface, with some epitaxial grains stretching into the film.
- Films pyrolysed at lower temperatures contained a higher amount of epitaxial growth.
- No films had a high degree of orientation.
- The crystal texture in the growth direction shows indications of a weak [001] texture attributed to the small amounts of epitaxy in the films.
- FIB and PIPS preparation of TEM specimens yielded high quality samples with vast, electron transparent regions.
- The unsintered thin films delaminated during PIPS sample preparation.

7 Further Work

Both the PIPS and FIB preparation techniques used for KNN thin films in this work yielded high quality TEM specimens with no clear preparation artefacts. The SPED technique used in this study gave detailed information on growth morphology, crystallographic structure and the texture of the films. By performing this technique on multiple thin films exposed to different heat treatments, a study of these thin film features as a function of process parameters like pyrolysis and sintering was enabled.

As a presence of a secondary phase has been confirmed for some of the specimens, it may be of interest to analyse variations in atomic composition of the films. This may be accomplished by doing energy-dispersive X-ray spectroscopy (EDS) in TEM, a technique which utilises characteristic X-rays to determine which elements are present. Another approach may be electron energy-loss spectroscopy (EELS) in TEM, which discriminate the transmitted electrons according to their loss of kinetic energy when interacting with the specimen. Both techniques can be used in scanning TEM (STEM) for chemical and elemental mapping. By comparing these maps to SPED maps, a study of how the variations in elemental composition are connected to variations within the microstructure is enabled. The techniques could also give valuable information on the epitaxial layer observed at the interface between the substrate and film.

In order to improve the determination of grain boundaries and texture, it is obvious that separation of different reflections in PED patterns from overlapping grains is of importance. A recent open-source Python library for crystallographic electron microscopy named *pyXem* (Python Crystallographic Electron Microscopy) [60], shows potential of being as suitable alternative to both NanoMegas and the MTEX software. One of the goals of this project is to improve the template matching routines through open collaboration and utilisation of existing, well established Python libraries. The pyXem project is still in its early stages of development with potential errors. However, as the use of the SPED technique is continuously increasing, more contributions to the code are being made, which can be beneficial for many working in the field of crystallographic electron microscopy.

References

[1] J. Rödel, W. Jo, K. T. P. Seifert, E.-M. Anton, T. Granzow, and D. Damjanovic, "Perspective on the development of lead-free piezoceramics," *Journal of American Ceramic Society*, vol. 92, no. 6, pp. 1153–1177, 2009.

[2] G. H. Haertling, "Ferroelectric ceramics: History and technology," *Journal of American Ceramic Society*, vol. 82, no. 4, pp. 797–818, 1999.

[3] S. Katzir, "Who knew piezoelectricity? Rutherford and Langevin on submarine detection and the invention of sonar," *The Royal Society Journal of The History of Science*, vol. 66, pp. 141–157, 2012.

[4] M. T. Ghoneim, M. A. Zidan, M. Y. Alnassar, A. N. Hanna, J. Kosel, K. N. Salama, and M. M. Hussain, "Thin PZT-based ferroelectric capacitors on flexible silicon for nonvolatile memory applications," *Advanced Electronic Materials*, vol. 1, no. 6, pp. 411–418, 2015.

[5] T. Kanda, T. Morita, M. K. Kurosawa, and T. Higuchi, "A rod-shaped vibro touch sensor using PZT thin film," *IEEE Transactions on Ultrasonics, Ferroelectrics, and Frequency Control*, vol. 46, no. 4, pp. 875–882, 2002.

[6] B. Jaffe, W. R. Cook, and H. Jaffe, *Piezoelectric ceramics*. Academic Press, 1971.

[7] "Council of European Union. rohs directive 2002/95/ec." URL: `http://eur-lex.europa.eu/legal-content/EN/TXT/HTML/?uri=CELEX:32002L0095&from=EN`, 2003. Accessed: 14.11.2017.

[8] Y. Saito, H. Takao, T. Tani, T. Nonoyama, K. Takatori, T. Homma, T. Nagaya, and M. Nakamura, "Lead-free piezoceramics," *Nature*, vol. 432, pp. 84–87, 2004.

[9] X. Wang, J. Wu, D. Xiao, J. Zhu, X. Cheng, T. Zheng, B. Zhang, X. Lou, and X. Wang, "Giant piezoelectricity in potassium–sodium niobate lead-free ceramics," *Journal of American Chemical Society*, vol. 136, no. 7, pp. 2906–2910, 2014.

[10] J. Kwak, A. Kingon, and S.-H. Kim, "Lead-free $(Na_{0.5}K_{0.5})NbO_3$ thin films for the implantable piezoelectric medical sensor applications," *Materials Letters*, vol. 82, pp. 130–132, 2012.

[11] A. Toresen, "The search for lead-free piezoelectric materials: A TEM characterisation of KNN thin films." Project's thesis, Norwegian University of Science and Technology, 2017.

[12] C. Kittel, *Introduction to Solid State Physics*. John Wiley & Sons, Inc, 8th ed., 2005.

[13] T. Hahn, *International Tables for Crystallography*, vol. A. Springer, 5th ed., 2005.

[14] M. Lallart, ed., *Ferroelectrics - Characterization and Modeling*. InTech, 1 ed., 2011.

[15] K. K. T. Lorentzen, "Deposition of phase pure KNN thin films," Master's thesis, Norwegian University of Science and Technology, 2016.

[16] K. Momma and F. Izumi, "VESTA 3 for three-dimensional visualization of crystal, volumetric and morphology data," *Journal of Applied Crystallography*, vol. 44, pp. 1272–1276, 2011.

[17] R. M. Hazen, "Perovskites," *Scientific American*, vol. 258, no. 6, pp. 52–61, 1988.

[18] J.-F. Li, K. Wang, F.-Y. Zhu, L.-Q. Cheng, and F.-Z. Yao, "$(K, Na)NbO_3$-based lead-free piezoceramics: Fundamental aspects, processing technologies, and remaining challenges," *Journal of American Ceramic Society*, vol. 96, no. 12, pp. 2677–3696, 2013.

[19] H. E. Mgbemere, M. Hinterstein, and G. A. Schneider, "Structural phase transitions and electrical properties of $(K_xNa_{1-x})NbO_3$-based ceramics modified with Mn," *Journal of the Euoprean Ceramic Society*, vol. 32, pp. 4341–4352, 2012.

[20] P. Kumar, M. Pattanaik, and Sonia, "Synthesis and characterizations of KNN ferroelectric ceramics near 50/50 MPB," *Ceramic International*, vol. 39, no. 1, pp. 65–69, 2012.

[21] G. Khorramia, A.Kompanya, and A. Zakb, "Structural and optical properties of $(K, Na)NbO_3$ nanoparticles synthesized by a modified sol–gel method using starch media," *Advanced Powder Technology*, vol. 26, no. 1, pp. 113–118, 2015.

[22] O. Madelung, U. Rössler, and M. Schulz, eds., *Ternary Compounds, Organic Semiconductors*. Springer, 2000.

[23] P. R. Potnis, N.-T. Tsou, and J. E. Huber, "A review of domain modelling and domain imaging techniques in ferroelectric crystals," *Materials*, vol. 4, pp. 417–447, 2011.

[24] L. Zheng, X. Huo, R. Wang, J. Wang, W. Jiang, and W. Cao, "Large size lead-free $(Na, K)(Nb, Ta)O_3$ piezoelectric single crystal: Growth and full tensor properties," *CrystEngComm*, vol. 15, pp. 7718–7722, 2013.

[25] E. Ruska, "The development of the electron microscope and of electron microscopy," *Bioscience Reports*, vol. 7, no. 9, pp. 607–629, 1987.

[26] D. B. Williams and C. B. Carter, *Transmission Electron MIcroscopy*. Springer, 2nd ed., 2009.

[27] "Schematic drawing of a transmission electron microscope (TEM)." URL: `https://commons.wikimedia.org/wiki/File:Scheme_TEM_en.svg`. Accessed: 03.12.2017.

[28] R. Vincent and P. A. Midgley, "Double conical beam-rocking system for measurement of integrated electron diffraction intensities," *Ultramicroscopy*, vol. 53, no. 3, pp. 271–282, 1994.

[29] P. A. Midgley and A. S. Eggeman, "Precession electron diffraction – a topical review," *IUCrJ*, vol. 2, no. 1, pp. 126–136, 2015.

[30] V. Randle and O. Engler, *Introduction to Texture Analysis: Macrotexture, Microtexture and Orientation Mapping*. CRC Press, 2009.

[31] H. Bunge, *Texture analysis in Materials Science*. Butterworth & Co, 1982.

[32] S. Suwas and R. K. Ray, *Crystallographic Texture of Materials*. Springer, 2014.

[33] B. C. Nzogang, J. Bouquerel, P. Cordier, A. Mussi, J. Girard, and S. Karato, "Characterization by scanning precession electron diffraction of an aggregate of bridgmanite and ferropericlase deformed at HP-HT," *Geochemistry, Geophysics, Geosystems*, 2018.

[34] E. F. Rauch and L. Dupuy, "Rapid diffraction patterns identification through template matching," *Archives of Metallurgy and Materials*, vol. 50, no. 1, pp. 87–99, 2005.

[35] E. Rauch and M. Véron, "Automated crystal orientation and phase mapping in TEM," *Materials Characterization*, vol. 98, pp. 1–9, 2014.

[36] S. M. Dale, "Lead-free piezoelectric materials for medical technology," Master's thesis, Norwegian University of Science and Technology, 2018.

[37] A. Tian, W. Ren, L. Wang, P. Shi, X. Chen, X. Wu, and X. Yao, "Effect of deposition temperature on orientation and electrical properties of $(Na_{0.5}K_{0.5})NbO_3$thin films by pulsed laser deposition," *Applied Surface Science*, vol. 258, no. 7, pp. 2674–2678, 2012.

[38] X. Wang, U. Helmersson, and S. Olafsson, "Growth and field dependent dielectric properties of epitaxial $Na_{0.5}K_{0.5}NbO_3$ thin films," *Applied Physics Letters*, vol. 73, no. 7, pp. 927–930, 1998.

[39] R. W. Schwartz, T. Schneller, and R. Waser, "Chemical solution deposition of electronic oxide films," *Comptes Rendus Chimie*, vol. 7, no. 5, pp. 433–461, 2004.

[40] M. K. V. Bael, D. Nelis, A. Hardy, D. Mondelaers, K. V. Werde, J. D'Haen, G. Vanhoyland, H. V. D. Rul, J. Mullens, L. C. V. Poucke, F. Frederix, and D. J. Wouters, "Aqueous chemical solution deposition of ferroelectric thin films," *Integrated Ferroelectrics*, vol. 45, no. 1, pp. 113–122, 2002.

[41] "Gatan microscopy suite software." URL: `http://www.gatan.com/products/tem-analysis/gatan-microscopy-suite-software`. Accessed: 03.12.2017.

[42] "NanoMegas." URL: `http://www.nanomegas.com/`. Accessed: 06.05.2018.

[43] J. Cowley, "Applications of electron nanodiffraction," *Micron*, vol. 35, pp. 345–360, 2004.

[44] J. S. Barnard, D. N. Johnstone, and P. A. Midgley, "High-resolution scanning precession electron diffraction: Alignment and spatial resolution," *Ultramicroscopy*, vol. 174, pp. 79–88, 2017.

[45] F. Bachmann, R. Hielscher, and H. Schaeben, "Texture analysis with MTEX - free and open source software toolbox," *Solid State Phenomena*, vol. 160, pp. 63–68, 2010.

[46] "MTEX." URL: `http://mtex-toolbox.github.io.` Accessed: 06.05.2018.

[47] "Inkscape." URL: `https://inkscape.org/en/`. Accessed: 06.05.2018.

[48] N. H. Gaukås, S. M. Dale, T. M. Ræder, A. Toresen, R. Holmestad, J. Glaum, M.-A. Einarsrud, and T. Grande, "Controlling phase purity in KNN thin films by aqueous chemical solution deposition." (to be published), 2018.

[49] C. Li, L. Wang, Z. Wang, Y. Yang, W. Ren, and G. Yang, "Atomic resolution interfacial structure of lead-free ferroelectric $K_{0.5}Na_{0.5}NbO_3$ thin films deposited on $SrTiO_3$," *Scientific Reports*, vol. 6, 2016.

[50] Y. Zhen and J.-F. Li, "Normal sintering of $(K, Na)NbO_3$-based ceramics: Influence of sintering temperature on deification, microstructure and electrical properties," *Journal of American Ceramic Society*, vol. 89, no. 12, pp. 3669–3675, 2006.

[51] J. Fang, X. Wang, Z. Tian, C. Zhong, and L. Li, "Two-step sintering: An approach to broaden the sintering temperature range of alkaline niobate-based lead-free piezoceramics," *Journal of American Ceramic Society*, vol. 93, no. 11, pp. 3552–3555, 2010.

[52] T. Schneller, R. Waser, M. Kosec, and D. Payne, eds., *Chemical Solution Deposition of Functional Oxide Thin Films*. Springer, 2013.

[53] T. Schuler, T. Krajewski, I. Grobelsek, and M. Aegerter, "A microstructural zone model for the morphology of sol-gel coatings," *Journal of Sol-Gel Science and Technology*, vol. 31, pp. 235–239, 2004.

[54] K.-N. Pham, N. H. Gaukås, M. Morozov, T. Tybell, P. E. Vullum, T. Grande, and M.-A. Einarsrud, "Epitaxial $K_{0.5}Na_{0.5}NbO_3$ thin films by aqueous chemical solution deposition." (to be published), 2018.

[55] Q. Yu, J.-F. Li, Y. Chen, L.-Q. Cheng, W. Sun, Z. Zhou, and Z. Wang, "Effect of pyrolysis temperature on sol–gel synthesis of lead-free piezoelectric $(K, Na)NbO_3$ films on NbNb substrates," *Journal of American Ceramic Society*, vol. 97, no. 1, pp. 107–113, 2014.

[56] R. W. Schwartz, "Chemical solution deposition of perovskite thin films," *Chemistry of Materials*, vol. 9, no. 11, p. 2325–2340, 1997.

[57] J. Mason and C. Schuh, "The generalized mackenzie distribution: Disorientation angle distributions for arbitrary textures," *Acta Materialia*, vol. 57, no. 14, pp. 4186–4197, 2009.

[58] F. Humphreys, P. Bate, and P. Hurley, "Orientation averaging of electron backscattered diffraction data," *Journal of Microscopy*, vol. 201, pp. 50–58, 2000.

[59] J. Wheeler, D. Prior, Z. Jiang, R. Spiess, and P. Trimby, "The petrological significance of misorientation between grains," *Contributions to Mineralogy and Petrology*, vol. 141, no. 1, pp. 109–124, 2001.

[60] "pyXem." URL: `www.github.com/pyxem/pyxem`. Accessed: 17.06.2018.

[61] N. Zhang, A. M. Glazer, D. Baker, and P. A. Thomas, "Structures of $K_{0.05}Na_{0.95}NbO_3$ (50-300 k) and $K_{0.30}Na_{0.70}NbO_3$ (100-200 k)," *Acta Crystallographica Section B*, vol. 65, no. 3, pp. 291–299, 2009.

A Data Analysis Code from Matlab

```
% Define crystal system
CS = {...
    'notIndexed',...
    crystalSymmetry('m-3m', [3.983 3.983 3.983], 'mineral', 'KNN', 'color', '
    light blue')};

% Set Plotting convention
setMTEXpref('xAxisDirection', 'east');
setMTEXpref('zAxisDirection', 'intoPlane');

% Load data
data = struct();
data.rawData = loadEBSD(fullfile('file.ang'), CS, 'interface', 'ACOM');
data.rawData.scanUnit = 'nm';

% Manually obtained ROI and STO region
roi = [20 54 1279-20 265-54];
sto = [25 10 1275-25 40-10];

% Create reference for STO-orientation
limit = inpolygon(data.rawData, sto);
STOregion = data.rawData(limit);
STOref = mean(STOregion.orientations);

% Crop the map to ROI
limit = inpolygon(data.rawData, roi);
data.roi = data.rawData(limit);

% Filter the remaining data based on mean Q
avIndex = mean(data.roi.index);
data.FD = data.roi(data.roi.index > avIndex/2);

% Normalise R to 100 and save mean values for R and Q
data.FD.rel = data.FD.rel*100;
avRelALL = mean(data.FD.rel);
avIndexALL = mean(data.FD.index);
```

Listing 1: Orientation data filtering in the Matlab toolbox MTEX.

```
% Define initial grains (grainsB) before filtering out small grains
[grains, dataC.grainId, dataC.mis2mean] = calcGrains(dataC, 'boundary', 'tight', 'angle', 4*degree);
toRemove = grains(grains.grainSize <= 20);
dataC(toRemove) = [];

% Create the final grains (grainsC)
[grainsC, dataC.grainId, dataC.mis2mean] = calcGrains(dataC, 'angle', 4*degree);


% Compare orientation of grains before merging
g1 = 20;
g2 = 31;
cake = angle(grainsC.meanOrientation(g1), grainsC.meanOrientation(g2))/degree;

% Obtain the grain boundary between mergin grains
mergeBoundary = grainsC.boundary(grainsC(g1));
mergeBoundary = mergeBoundary(grainsC(g2));

% Create new set of merged grains
[mergedGrains ,parentId] = merge(grainsC,mergeBoundary,'calcMeanOrientation');

% Update a dataset containing merged grains
dataM = dataC;
dataM('indexed').grainId = parentId(Dselect('indexed').grainId);
```

Listing 2: Reconstruction and merging of grains in the Matlab toolbox MTEX.

B Pole Figures and ODFs

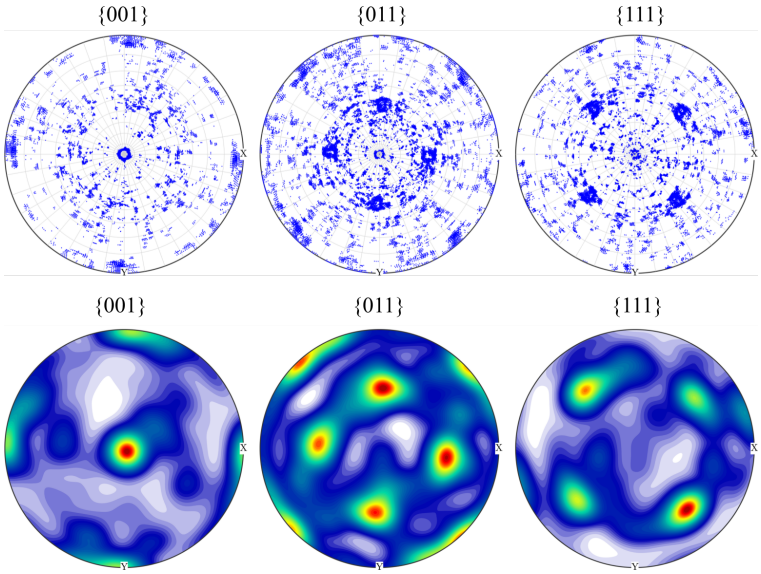

Figure B.1: {001}, {011} and {111} pole figures of all recorded crystal coordinates relative to the specimen coordinates of specimen *P450S*. Calculated ODFs of these are included, with colours indicating probability density from low (light blue) to high (red).

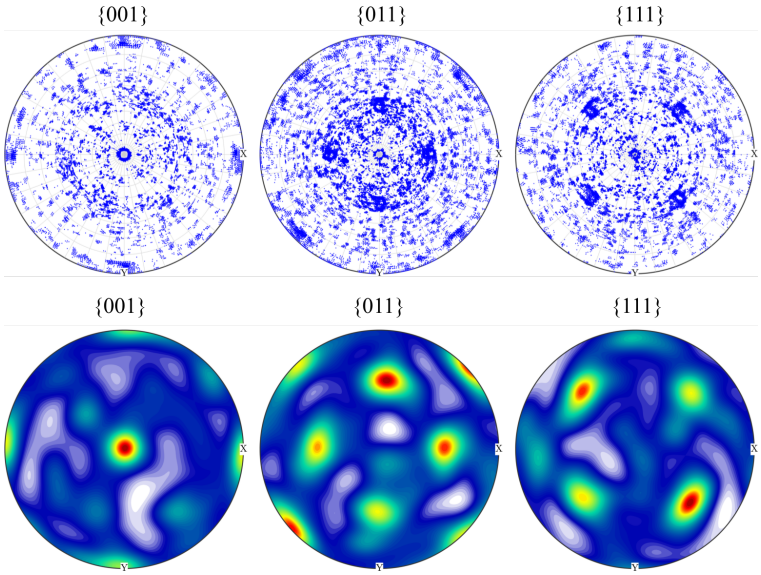

Figure B.2: {001}, {011} and {111} pole figures of all recorded crystal coordinates relative to the specimen coordinates of specimen *P500N*. Calculated ODFs of these are included, with colours indicating probability density from low (light blue) to high (red).

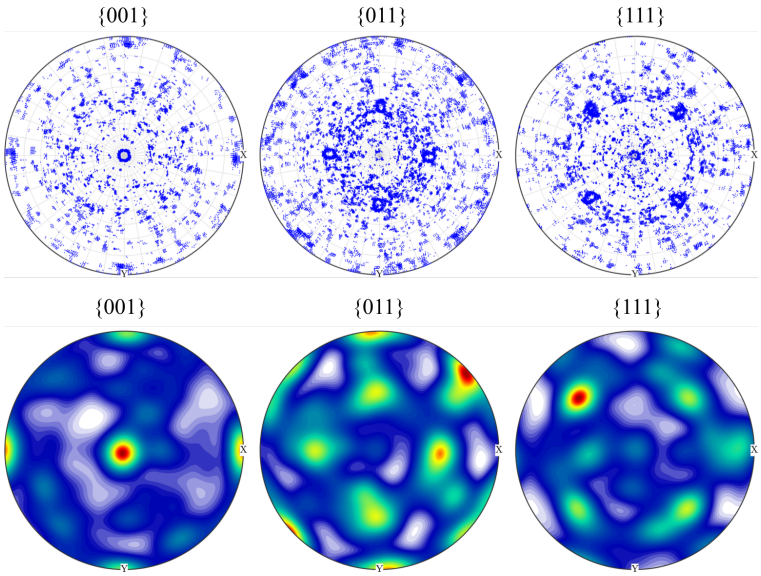

Figure B.3: {001}, {011} and {111} pole figures of all recorded crystal coordinates relative to the specimen coordinates of specimen *P500S*. Calculated ODFs of these are included, with colours indicating probability density from low (light blue) to high (red).

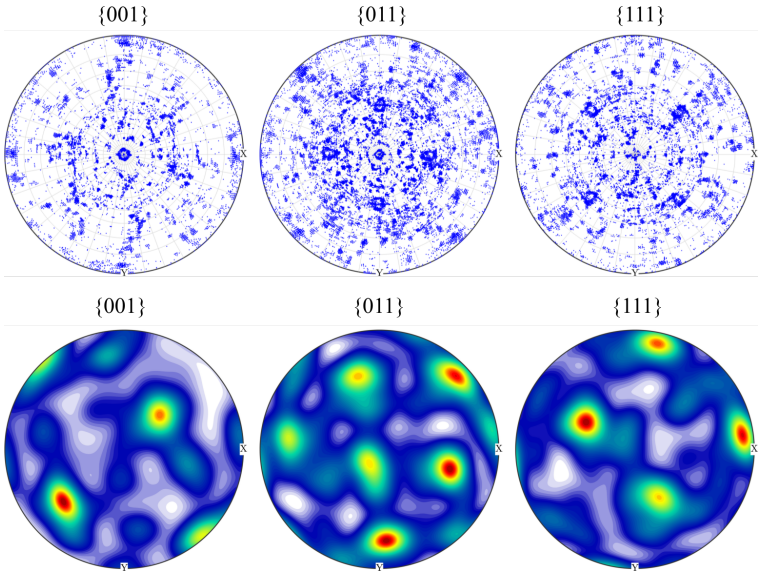

Figure B.4: {001}, {011} and {111} pole figures of all recorded crystal coordinates relative to the specimen coordinates of specimen *P550Sa*. Calculated ODFs of these are included, with colours indicating probability density from low (light blue) to high (red).

C Crystal Structures

Table 8: Atomic coordinates for STO with space group $Pm\bar{3}m$. Lattice parameters are $\mathbf{a} = \mathbf{b} = \mathbf{c} = 3.905$ Å and angles $\alpha = \beta = \gamma = 90°$ [22].

Element	X	Y	Z	Occupation
Sr	0.0	0.0	0.0	1.0
Ti	0.5	0.5	0.5	1.0
O	0.0	0.5	0.5	1.0

Table 9: Atomic coordinates for the pseudo-cubic structure of KNN. The space group is $Pm\bar{3}m$ with lattice parameters $\mathbf{a} = \mathbf{b} = \mathbf{c} = 3.983$ Å and angles $\alpha = \beta = \gamma = 90°$.

Element	X	Y	Z	Occupation
K	0.0	0.0	0.0	0.5
Na	0.0	0.0	0.0	0.5
Nb	0.5	0.5	0.5	1.0
O	0.0	0.5	0.5	1.0

Table 10: Atomic coordinates for the monoclinic structure of (30/70) KNN. The space group is Pm with lattice parameters $\mathbf{a} = 5.659$, $\mathbf{b} = 3.939$ and $\mathbf{c} = 5.625$ Å and angles $\alpha = \gamma = 90°$ and $\beta = 90.073°$ [61].

Element	X	Y	Z	Occupation
Na	0.5389	0.5000	0.0180	0.7
K	0.5389	0.5000	0.0180	0.3
Na	0.0389	0.5000	0.5180	0.7
K	0.0389	0.5000	0.5180	0.3
Nb	0.0362	0.0000	-0.0030	1.0
Nb	0.5362	0.0000	0.4970	1.0
O	0.0000	0.5000	0.0000	1.0
O	0.5000	0.5000	0.5000	1.0
O	0.2737	0.0000	0.2286	1.0
O	0.2286	0.0000	0.7263	1.0
O	0.7714	0.0000	0.2737	1.0
O	0.7263	0.0000	0.7714	1.0

Table 11: Atomic coordinates for the orthorhombic structure of KNN. The space group is Amm2 with lattice parameters $\mathbf{a} = 3.944$, $\mathbf{b} = 5.643$ and $\mathbf{c} = 5.676$ Å and angles $\alpha = \beta = \gamma = 90°$ [19].

Element	**X**	**Y**	**Z**	**Occupation**
K	0.0000	0.0000	0.0453	0.5
Na	0.0000	0.0000	0.0453	0.5
Nb	0.5000	0.0000	0.5251	1.0
O	0.0000	0.0000	0.4727	1.0
O	0.5000	0.7535	0.2285	1.0

D Maps of Correlation Index and Reliability

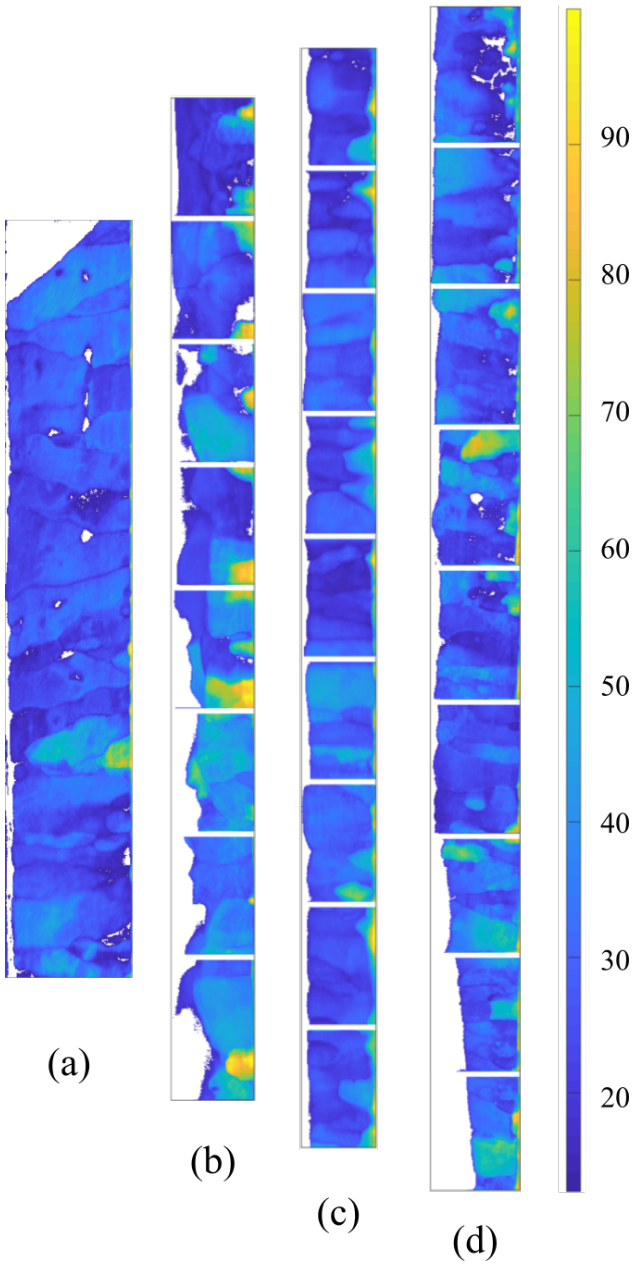

Figure D.1: Quality of template matching in maps of correlation index Q, produced by datasets from specimen *P550Sa* (a), *P450S* (b), *P500S* (c) and *P500N* (d). The substrate is oriented to right for all maps.

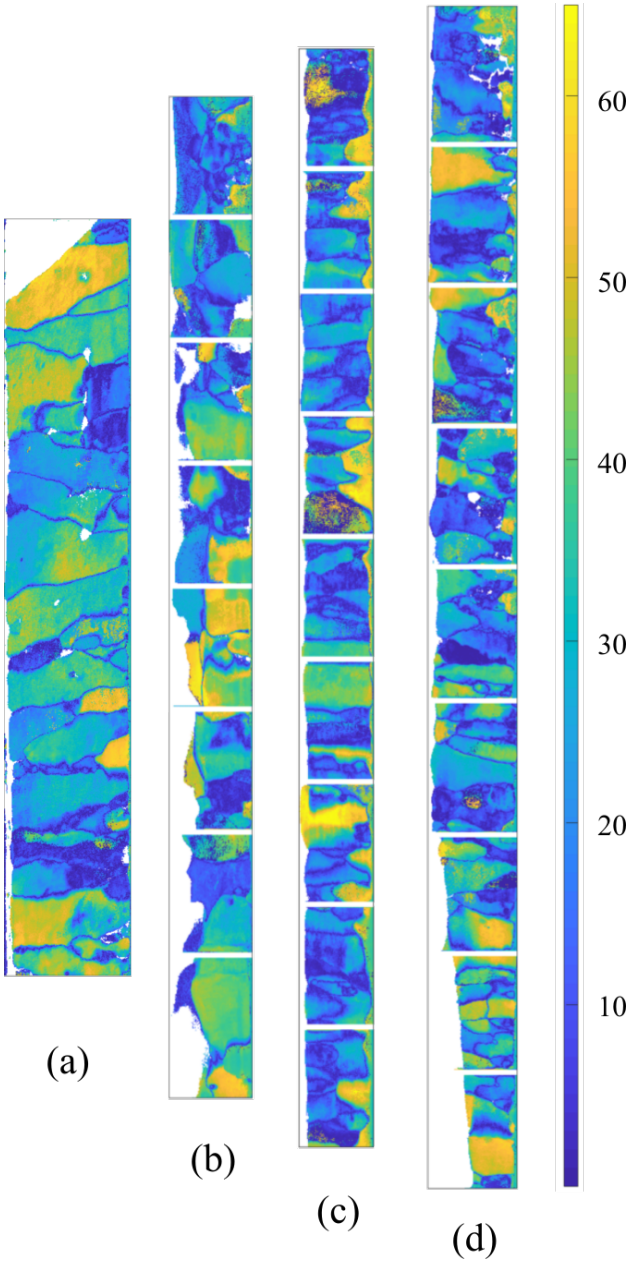

Figure D.2: Quality of template matching in maps of reliability R, produced by datasets from specimen specimen *P550Sa* (a), *P450S* (b), *P500S* (c) and *P500N* (d). The substrate is oriented to right for all maps.